INFRARED PHOTOFRAGMENT SPECTROSCOPY OF CHARGED AMINO ACID WATER CLUSTERS IN THE GAS PHASE

THÈSE N^{O} 3441 (2006)

PRÉSENTÉE À LA FACULTÉ SCIENCES DE BASE

Institut des sciences et ingénierie chimiques

SECTION DE CHIMIE ET GÉNIE CHIMIQUE

ÉCOLE POLYTECHNIQUE FÉDÉRALE DE LAUSANNE

POUR L'OBTENTION DU GRADE DE DOCTEUR ÈS SCIENCES

PAR

Anthi KAMARIOTOU

DEA de chimie physique, Université Louis Pasteur, Strasbourg, France
et de nationalité hellénique

acceptée sur proposition du jury:

Prof. Th. Rizzo, directeur de thèse
Prof. P. Dyson, rapporteur
Prof. S. Leutwyler, rapporteur
Prof. R. Weinkauf, rapporteur

Lausanne, EPFL
2006

Abstract

We present in this work a new technique, which combines laser photofragmentation spectroscopy with tandem mass spectrometry, for structural investigations of biomolecular ions in the gas phase. A novel apparatus was designed and built for the implementation of these studies. In this instrument closed shell ions are produced in the gas phase by electrospray ionization and stored in a hexapole ion trap prior to mass selection of a parent beam in a first quadrupole and then irradiation in an octupole ion guide using laser light. Mass analysis of the photofragmentaion products in a final stage quadrupole as a function of the wavelength generates an action spectrum.

We applied this new technique to follow the microsolvation of charged amino acids in the gas phase. In these studies, the nanoelectrospray ionization source generates a distribution of water clusters of charged amino acids at various hydration levels. A particular size of cluster is selected and irradiated by infrared laser pulses resulting in the dissociation of one water molecule. Detection of the photofragmentation of this weak non-covalent bond allows us to generate the vibrational action spectrum of this particular cluster. We use a two-stage difference frequency mixing setup to produce laser light in the 2900-3800 cm^{-1}, allowing us to probe the light-atom stretching region.

IR photofragmentation spectra have been obtained for the hydrates of protonated and lithiated valine and those of protonated tryptophan. By probing the region of free and hydrogen-bonded N-H and O-H stretch vibrations and with the help of density functional theory calculations at the B3LYP/6-31++G** level, we relate spectral changes to the structure of clusters. In the study of lithiated valine water clusters, we addressed the question of zwitterion formation upon the combined effect of water and an external ion. Our data indicate the presence of the non-zwitterionic form of valine upon addition of up to four water molecules. In all of the species studied here, the hydration process is driven by solvation of the charge, and upon completion of a first shell around it, water preferentially forms a second solvation shell with no strong competition from other hydration sites on the amino acid backbone. Strikingly, similar water network structures have been observed at the highest hydration level of completely different species, probably indicating the existence of stable ordered water structures. We obtained evidence for a structrual change of the valine backbone in lithiated valine upon addition of the third water molecule, while no conformational change has been identified in the clusters of the protonated species. We have thus been able to answer questions related to the conformational preferences of the amino acid and the structuring of the water network.

Version abrégée

Au cours de ce travail, une nouvelle technique a été élaborée combinant spectroscopie laser de photofragmentation et spectrométrie de masse en tandem, afin d'étudier la structure en phase gazeuse de molécules d'intérêt biologique. Nous avons construit pour cela un nouvel appareil, où les ions produits par ionisation électrospray sont piégés dans un hexapole et sélectionnés en masse par un quadrupole, de sorte à permettre l'irradiation laser d'une seule masse parent. Un second analyseur quadripolaire effectue la mesure de masse d'un des fragments issus de la photodissociation en fonction de la longueur d'onde, générant ainsi le spectre d'action de la molécule.

Cette technique a été appliquée à l'étude de microsolvatation d'acides aminés chargés en phase gazeuse. Une source nanospray permet de produire une distribution de clusters d'acides aminés avec un nombre variable d'adduits d'eau. Après sélection en masse d'un seul état d'hydratation, le complexe non-covalent est dissocié grâce à l'énergie d'un faisceau laser infrarouge de longueur d'onde variable permettant ainsi d'obtenir le spectre vibrationnel de la molécule. Nous avons utilisé un dispositif de mélange optique par différence de fréquence en deux étapes (DFM- Difference Frequency mixing) pour générer une radiation dans le domaine de fréquences d'absorption des vibrations C-H, N-H et O-H (2900 - 3800 cm^{-1}).

Les spectres de photofragmentation infrarouge ont été mesurés pour les complexes d'hydratation du tryptophane protoné ($Trp•H^+(H_2O)_n$), de la valine protonée ($Val•H^+(H_2O)_n$), et de la valine neutre coordinée à un atome de lithium ($Val•Li^+(H_2O)_n$). Sur la base de ces données et grâce à des calculs de densité fonctionnelle B3LYP/6-31++G**, il a été possible de mettre en relation les déplacements des bandes d'absorption et les caractéristiques structurales de chaque complexe. Ainsi, l'étude de $Val•Li^+(H_2O)_n$ soulève le problème de formation du zwitterion de la valine dû à l'effet combiné du solvant et des interactions électrostatiques avec un ion externe. Nos données expérimentales indiquent la présence de la forme non zwitterionique de la valine malgré l'ajout de quatre molécules d'eau. Il semblerait, d'après les différents complexes d'hydratation étudiés, que la présence d'une charge dans le cluster contrôle le processus de solvatation. Après saturation de la première couche de solvatation, les molécules d'eau forment préférentiellement une seconde couche, alors que la présence d'autres sites propices à l'hydratation ne semble pas donner lieu à une compétition avec les interactions solvant-solvant. Par ailleurs, les similitudes observées dans les structures du réseau de solvant dans les complexes étudiés, indépendamment de la nature de l'acide aminé, indiquent probablement l'existence de structures ordonnées stables du solvant. De plus, un changement structural du squelette de la valine a été mis en évidence dans le complexe de $Val•Li^+(H_2O)_3$, alors qu'aucun changement conformationnel n'a été identifié dans les clusters des espèces protonées. Ainsi, ces études de micro-solvatation ont fourni des informations utiles concernant l'influence du solvant sur les préférences conformationnelles des acides aminés étudiés et la structuration du solvant atour de ceux-ci.

Contents

Acknowledgments

Curriculum Vitae

Introduction

Understanding the mechanisms that govern life represents one of the biggest motivations and challenges for science, as revealed by the active interdisciplinary efforts developed over the last few decades. The beauty of investigations on 'living matter' resides in the principle that complexity grows out of simplicity. Only four nucleic bases contain all of the information necessary to create life: adenine, thymine, cytosine and guanine. They form the sub-units of the DNA double strand, which after replication and transcription generates proteins.

Proteins are composed of sequences of the 22 natural amino acids, which all have in common a carboxylic acid function and an amine group but only differ by the nature of their residue. They are linked together by the covalent peptitde bond and also interact non-covalently to form large, highly ordered three-dimensional molecular edifices. The resulting secondary and tertiary structures are endowed with a specific function within their biological environment. Non-covalent interactions play a dominant role in protein structure and function. The comprehension of the forces that drive protein folding into well-ordered molecular architectures and how these are related to a specific function, is necessary for developing a fundamental understanding of 'living matter'. The present work addresses this general problem, starting at the origin of complexity and seeking to provide information on the amino acid building blocks constituting proteins. We review here some of the important approaches for us, that have contributed to understand the structure of both large (proteins and their complexes) and small (amino acids and peptides) edifices, as isolated species and in a microsolvation environment.

I. Biological molecules in the gas phase

The predominant form of many biological molecules in aqueous solution is that of a closed shell molecular ion. The transfer of these species in the gas phase has been enabled by the introduction of two 'soft' ionization techniques, electrospray (ESI) [1, 2] and matrix laser assisted desorption/ionization (MALDI) [3, 4] in mass spectrometry. This important achievement has led to a flood of activity in the study of biomolecular ions in the gas phase. Removing them from their solvent environment allows for a more detailed investigation and comprehension of their intrinsic properties.

Mass spectrometry has largely contributed to determinations of protein sequences and their structural characterization. Dissociation studies such as collision induced dissociation (CID) [5, 6], infrared multiphoton dissociation (IRMPD) [7, 8], blackbody induced radiative dissociation (BIRD) [9, 10] and electron capture dissociation (ECD) [11] have played an important role in providing structural information on biological molecules and their energetics. When combined with hydrogen/deuterium exchange experiments [12-15] gross information has also been obtained on the overall shape of these flexible molecules, and their folding aspects have been revealed by subsequent denaturation studies [16]. Moreover, molecular weight determinations of non-covalently complexes of proteins demonstrate the relationship between structure and function, illustrating the principles of molecular recognition [17, 18].

On the other hand, other methods such as ion drift chromatography [19-23] electric deflection experiments [24-26] [27] and high-field asymmetric waveform ion mobility spectrometry (FAIMS) [28, 29] yield information on the gross structure of molecules ranging from small peptides to large proteins, based on the drift time of mass selected ions through a buffer gas, their dipole moment or their ion mobility at high electric fields. The combination of ion chromatography with H/D exchange [30] and denaturing experiments [31, 32] provides insights on protein folding and the intrinsic driving forces that determine the secondary structure of biomolecules. More recent coupling of ion mobility with dissociation techniques such as CID [33] opens up the doors of conformation-selective structural characterizations in mass spectrometry.

Although extremely valuable information can be inferred from the aforementioned methods by indirect means, they clearly lack the detailed structural characterization obtained in solution by crystallography and multidmensional NMR, which is also achieved in gas phase spectroscopic studies of small molecules. Moreover, when structural isomers or conformations do not differ by their mass, fragmentation patterns or ion mobilities, the limitation of these techniques can be overcome by optical methods of investigation, since spectroscopic properties are always sensitive to structural alterations.

II. Spectroscopy of neutrals

As described above, a great deal of effort has been devoted to the structural characterizations of biological molecules, e.g. on entire proteins. However, investigation of the structural properties of their building blocks, i.e., amino acids is also crucial for understanding and predicting their interactions in biological systems. Spectroscopic studies have adopted such a reductionist point of view in an effort of understanding complexity out of simplicity.

The application of gas phase spectroscopy to biologically related molecules was pioneered a couple of decades ago by Levy and coworkers [34-38]. Levy's group measured the first electronic spectrum of neutral tryptophan in a supersonic molecular beam, revealing the presence of different stable conformations of the amino acid. These landmark results were followed by numerous studies [39-50] related to conformational preferences of small molecules of biological interest. An entire arsenal of creative techniques has been developed based on double resonance spectroscopies, such as ultraviolet hole burning techniques [42, 51] and resonant ion depletion IR spectroscopy[52] for conformation-selective studies of individual amino acids and small peptides and their hydrates containing a few water molecules [46, 53, 54]. Recent advances extend the spectral range of investigation to the mid-IR region using difference frequency mixing in $AgGaSe_2$ [55-58] or infrared multiphoton dissociation with a free electron laser [50, 59]. This results in an increase of the level of information extracted by spectroscopic studies, since complementary pieces of information is obtained by probing simultaneously the low-frequency stretching and bending modes. Moreover, a new mass-isomer selective technique has been introduced by Gerhards and coworkers based on infrared/resonant two-photon ionization [57] and was successfully applied to the study of beta-sheet model structures. On the other hand, Zwier and coworkers[60-62] have shown the challenging perspectives of spectroscopic studies with experiments on population transfer between different conformers and measurement of the energy barriers separating the minima on the potential energy surface.

III. Spectroscopy of ions

Despite the predominance and the importance of closed shell ions in solution, early spectroscopic studies have been performed on neutral molecules because of the difficulty of producing sufficient gas phase concentrations of ions. However, the parallel progress made in mass spectrometry has set the scene for spectroscopic investigations of closed shell biomolecular ions and their clusters in the gas phase. Indeed, mass spectrometry has not only solved the problem of bringing biomolecular ions into the gas phase but it also provides an ideal environment for photofragmentation studies, which has been widely applied to spectroscopic studies of non-biologically related molecules [63-74]

Thus, the first spectroscopic studies of biologically related ions were published only recently. Ideue *et al* [75] and Rodriguez-Cruz *et al.* [76] reported the first laser induced fluorescence measurements of the tryptophan residue of cytochrome C in the electrospray plume. In both experiments, the fluorescence signal served to monitor conformational changes upon denaturation of the protein. Since then, a wide variety of photofragmentation methods have been used to extract spectroscopic information on biomolecular ions based on different detection schemes. Parks and coworkers monitored by fluorescence resonance energy transfer (FRET) spectroscopy the dissociation of weakly bound oligonucleotides duplexes stored in a quadrupole ion trap in order to follow conformational changes of the unzipping molecule [77]. Other studies are based on the photodissociation of a chemical bond upon electronic excitation of ions in an electrostatic storage ring, for instance by Andersen and coworkers [78], who measured the first absorption spectrum of the green fluorescent protein chromophore anion. The gas phase electronic spectra and lifetime measurements obtained for a number of biological ions have shown the importance of this innovative technique for probing the photophysics and structural properties of these ions [78-82]. Recently, a number of groups have performed UV spectroscopy of protonated aromatic amino acids [83-87] with the first electronic spectrum of protonated tryptophan measured at low temperature in a quadrupole ion trap by Nolting *et al.*[88].

Infrared spectroscopy of biomolecular ions started to emerge over the last couple of years based on the photodissociation of a chemical bond in an FT-ICR cell. Mainly structural information is extracted from the vibrational spectra obtained either in the light-atom stretching region [89] or in the mid-IR region by infrared multiphoton dissociation with a free electron laser [90-93]. Other infrared studies from Simons and coworkers [94] use photofragmentation of a weak bond to a ‘messenger’ molecule, while those of Desfrancois and coworkers involve photodetachment of a weakly bound electron in water complexes of formamide [95]. This group has developed a creative technique to study conformations of molecules of biological interest by forming dipole bound anions via Rydberg electron transfer [96].

IV. Hydration studies

The abundance of information obtained in the gas phase on bare molecular ions has contributed to an increased level of comprehension of the forces acting either through covalent bonds or non-covalent intramolecular interactions between neighboring groups, which control molecular shape and activity of biomolecules. However, the environment plays a predominant role in the properties of biological molecules and has been addressed by solvation studies in the gas phase. The presence of water is critical in protein structure and its maintenance. It is known to trigger protein folding but it also plays a key role in protein function dynamics and reactivity.

Hydration and dehydration studies of peptides and proteins are easily implemented in mass spectrometry due to the ability of ESI and MALDI in preserving weakly bound clusters of the biomolecular ions with water. The high degree of activity in this field indicates the necessity to test the relevance of gas phase studies and bridge the gap to solution phase experiments. The influence of protein structure and composition on the organization of the solvation shell was shown by the studies of Zhan et al. [97] together with the observation of clathrates in peptide water clusters by Beauchamp et and coworkers [98]. The observation of 'magic' numbers of water adducts by William's group suggest the existence of favorable arrangements of water (around gramicidin S $(M+2H)^{2+}$) [99] and can be related to a competition between solvation of the core molecule by water molecules versus self-solvation. Ion mobility experiments carried out by Jarrold and coworkers [22, 100, 101] have mainly addressed the effect of charge and conformation on the propensity of proteins to bind water, while more recent experiments by Wyttenbach *et al* [102, 103] have brought new insights into this field. All of these studies demonstrate that the solute plays a clear role in the build up of the solvation shell around it.

In the opposite sense, spectroscopic studies have shown that conformational preferences, and hence properties, of flexible biological molecules can change in the presence of solvent [51, 53-55, 59, 104] due to the subtle balance of inter- and intramolecular interactions between the molecule and its microsolvation shell. A clear example where solvent plays a crucial role is zwitterion formation. In aqueous solution at physiological pH, most amino acids are in their zwitterionic form, where the carboxylic acid group is deprotonated and a amino group is protonated. However, in the absence of water, both experimental and theoretical work suggest that isolated neutral amino acids such as glycine [105-107], alanine [108, 109], valine [49, 110] and arginine [111, 112] exist in the non-zwitterionic form, although for arginine these two forms of the molecule are within a few kcal/mol in energy[112, 113]. Hydration studies seek to determine the number of water molecules necessary to stabilize the zwitterionic form in the hydrated clusters of amino acids. This has been pursued by spectroscopic studies in the gas phase [42, 53, 59, 114], in a matrix [115] and also addressed at a theoretical level [116-118].

A closely related subject is the role of salt-bridges, in which the presence of another charge, either from the same molecule or an external ion, stabilizes zwitterion formation. Electrostatic interactions between amino acids (and related molecules) and a metal ion have been investigated theoretically[119-123] and experimentally by blackbody infrared radiative dissociation (BIRD) [124-129], ion-mobility [130], kinetic methods [130] and vibrational photofragment spectroscopy using free electron laser [90]. The combined effect of metal ion binding and hydration has also been investigated by collision induced dissociation (CID) [131, 132] and BIRD experiments [125-127] as well as theoretical calculations[129].

A variety of approaches have been used both at experimental and theoretical level on a variety of amino acids, either with the stabilization through solvent interactions solely or through electrostatic interactions with a metal ion in order to understand how the zwitterionic form of amino acids can be stabilized in the gas phase. However, the lack of agreement between independent experimental results or predictions of theory show the difficulty of understanding the structural properties and the relationship with solvent environment of the most basic biological entities, amino acids. This example of amino acid solvation demonstrates the real need of spectroscopic studies on ions, since these can provide complementary information not only to that obtained on neutral molecules but also to that extracted by non-spectroscopic methods. The results of this thesis will show one example where non-spectroscopic measurements drew erroneous conclusions regarding zwitterion formation.

V. Role of theory

The experimental work reviewed above relies upon a strong support of theoretical calculations for structural determinations. The goal of theory is to predict energetically favored structures and calculate the molecular properties associated with a particular geometry, which can be compared with experimental results. However, the size and flexibility of biomolecules represent major challenges for theory, which needs to provide reliable information with low computational cost.

Experimental work is necessary to improve the ability of theory to predict structural properties of biologically related molecules by providing test cases for calculations. On the other hand, as experiments address more and more complex systems theory plays an indispensable role in interpreting the data.

VI. Goals

The general purpose of the present thesis was to develop a versatile tool devoted to spectroscopic studies of closed shell molecular ions of biological importance in the gas phase so as to deduce structural information. Having realized the advantages of mass spectrometric technological advances for the study of biological molecules, we built an electrospray ion trap mass spectrometer to perform photofragmentation laser spectroscopic studies in an effort of bringing together the two fields of ‘mass spectrometry’ and ‘spectroscopy’.

We chose, as a first application of our new technique, to study the microsolvation process of charged amino acids in the gas phase due to the fundamental importance of these studies for the comprehension of the interplay between structure of biological entities and environment.

Structural characteristics have spectroscopic signatures throughout the whole spectral range. Since, non-covalent interactions and in particular hydrogen-bonding largely determine the structure of biological molecules, vibrational spectroscopy in the infrared region is a good way to probe structural changes related to the formation and breaking of these labile bonds.

The challenge of these studies originates from the nature of the species under investigation. Their flexibility gives rise to a number of possible conformations relying upon intramolecular interactions. However, in the presence of solvent, the latter are in competition with intermolecular interactions, which may unfavor some of the conformations of the bare ion or even lock the molecule into a single conformation. Despite the simplicity of amino acids in comparison to proteins, they provide very rich information in terms of structural properties. In the present studies we have addressed a number of important questions:

(1) How does the conformation change in the presence of water? Does the charged amino acid retain conformational preferences of the bare molecule or does hydration lead to new conformational preferences?

(2) How does the solvent shell organize around the molecule. What are the driving forces of solvation: how are they related (or even influenced) by the amino acid structure and to the preferred binding sites of the solvent?

(3) How many water molecules are necessary to recover the structure of the molecule in bulk solution?

VII. Outline

As described in *Chapter 1* of this thesis, a substantial fraction of this work was devoted to the design, construction and implementation of an electrospray ionization (ESI) tandem ion trap photofragment mass spectrometer intended to produce closed shell molecular ions of biological interest for gas phase spectroscopic studies. *Chapter 2* discusses the details of infrared photofragmentation spectroscopy applied to the study of non-covalent species in our new instrument. The results concerning our spectroscopic investigations of charged amino acids in a microsolvation environment are presented in the last two chapters. *Chapter 3* addresses the question of zwitterion formation in the water clusters of lithiated valine and discusses the hydration process of protonated valine for comparison. The results on protonated tryptophan are reported in *Chapter 4* and show the influence of increasing the complexity of the amino acid for the microsolvation process. The *Conclusions and perspectives* provide a summary of the important results obtained, discuss the limitations of our technique and give an outlook for spectroscopic investigations of biologically related molecules in the gas phase.

References

1. Yamashita, M. and Fenn, J. B., J. Phys. Chem. (1984), 88, 4451-4459.
2. Fenn, J. B., Mann, M., Meng, C. K., Wong, S. F., and Whitehouse, C. M., Science (1989), 246, 64-71.
3. Karas, M. and Hillenkamp, F., Anal. Chem. (1988), 60, 2301-2303.
4. Hillenkamp, F., Karas, M., Beavis, R. C., and Chait, B. T., Anal. Chem. (1991), 63, A1193-A1202.
5. Talley, J. M., Cerda, B. A., Ohanessian, G., and Wesdemiotis, C., Chemistry - A European Journal (2002), 8, 1377-1388.
6. Jennings, K. R., Int. J. Mass Spectrom. (2000), 200, 479-493.
7. Hofstadler, S. A., SannesLowery, K. A., and Griffey, R. H., Anal Chem (1999), 71, 2067-2070.
8. Tonner, D. S. and McMahon, T. B., Anal. Chem. (1997), 69, 4735-4740.
9. Dunbar, R. C. and McMahon, T. B., Science (1998), 279, 194-197.
10. Schnier, P. D., Price, W. D., Jockusch, R. A., and Williams, E. R., J. Am. Chem. Soc. (1996), 118, 7178-7189.
11. Zubarev, R. A., Horn, D. M., Fridriksson, E. K., Kelleher, N. L., Kruger, N. A., Lewis, M. A., Carpenter, B. K., and McLafferty, F. W., Anal. Chem. (2000), 72, 563-573.
12. Katta, V. and Chait, B. T., J. Am. Chem. Soc. (1993), 115, 6317-6321.
13. Suckau, D., Shi, Y., Beu, S. C., Senko, M. W., Quinn, J. P., Wampler, F. M., and McLafferty, F. W., Proc. Natl. Acad. Sci. U. S. A. (1993), 90, 790-793.
14. McLafferty, F. W., Guan, Z. Q., Haupts, U., Wood, T. D., and Kelleher, N. L., J. Am. Chem. Soc. (1998), 120, 4732-4740.
15. Freitas, M. A. and Marshall, A. G., Int. J. Mass Spectrom. (1999), 183, 221-231.
16. Wood, T. D., Chorush, R. A., Wampler, F. M., Little, D. P., Oconnor, P. B., and McLafferty, F. W., Proc. Natl. Acad. Sci. U. S. A. (1995), 92, 2451-2454.
17. El-Kabbani, O., Rogniaux, H., Barth, P., Chung, R. P. T., Fletcher, E. V., Van Dorsselaer, A., and Podjarny, A., Proteins (2000), 41, 407-414.
18. Rogniaux, H., Sanglier, S., Strupat, K., Azza, S., Roitel, O., Ball, V., Tritsch, D., Branlant, G., and Van Dorsselaer, A., Anal. Biochem. (2001), 291, 48-61.
19. Wyttenbach, T., Batka, J. J., Gidden, J., and Bowers, M. T., Int. J. Mass Spectrom. (1999), 193, 143-152.
20. Wyttenbach, T., vonHelden, G., and Bowers, M. T., J. Am. Chem. Soc. (1996), 118, 8355-8364.
21. Gill, A. C., Jennings, K. R., Wyttenbach, T., and Bowers, M. T., Int. J. Mass Spectrom. (2000), 196, 685-697.
22. Jarrold, M. F., Annu. Rev. Phys. Chem. (2000), 51, 179-207.
23. Jarrold, M. F., Acc. Chem. Res. (1999), 32, 360-367.
24. Dugourd, P., Antoine, R., Breaux, G., Broyer, M., and Jarrold, M. F., J. Am. Chem. Soc. (2005), 127, 4675-4679.
25. Antoine, R., Compagnon, I., Rayane, D., Broyer, M., Dugourd, P., Breaux, G., Hagemeister, F. C., Pippen, D., Hudgins, R. R., and Jarrold, M. F., J. Am. Chem. Soc. (2002), 124, 6737-6741.

26. Antoine, R., Compagnon, I., Rayane, D., Broyer, M., Dugourd, P., Breaux, G., Hagemeister, F. C., Pippen, D., Hudgins, R. R., and Jarrold, M. F., Eur. Phys. J. D (2002), 20, 583-587.
27. Compagnon, I., Hagemeister, F. C., Antoine, R., Rayane, D., Broyer, M., Dugourd, P., Hudgins, R. R., and Jarrold, M. F., J. Am. Chem. Soc. (2001), 123, 8440-8441.
28. Guevremont, R., J. Chromatogr. A (2004), 1058, 3-19.
29. Purves, R. W., Barnett, D. A., and Guevremont, R., Int. J. Mass Spectrom. (2000), 197, 163-177.
30. Valentine, S. J. and Clemmer, D. E., J. Am. Chem. Soc. (1997), 119, 3558-3566.
31. Mao, Y., Woenckhaus, J., Kolafa, J., Ratner, M. A., and Jarrold, M. F., J. Am. Chem. Soc. (1999), 121, 2712-2721.
32. Shelimov, K. B., Clemmer, D. E., Hudgins, R. R., and Jarrold, M. F., J. Am. Chem. Soc. (1997), 119, 2240-2248.
33. Hilderbrand, A. E., Myung, S., Barnes, C. A. S., and Clemmer, D. E., J. Am. Soc. Mass Spectrom. (2003), 14, 1424-1436.
34. Park, Y. D., Rizzo, T. R., Peteanu, L., and Levy, D. H., J. Chem. Phys. (1986), 84, 6539.
35. Park, Y. D., Rizzo, T. R., Peteanu, L. A., and H., L. D., J. Chem. Phys (1986), 84, 6593-6549.
36. Rizzo, T. R., Park, Y. D., Peteanu, L. A., and H., L. D., J. Chem. Phys (1985), 84, 2541-2534.
37. Rizzo, T. R., Park, Y. D., Peteanu, L. A., and H., L. D., J. Chem. Phys (1985), 83, 4819-4820.
38. Rizzo, T. R., Park, Y. D., Peteanu, L. A., and Levy, D. H., J. Chem. Phys. (1986), 84, 2534-2541.
39. Cable, J. R., Tubergen, M. J., and Levy, D. H., J. Am. Chem. Soc. (1987), 109, 6198-6199.
40. Carney, J. R. and Zwier, T. S., J. Phys. Chem. A (2000), 104, 8677-8688.
41. Snoek, L. C., Kroemer, R. T., Hockridge, M. R., and Simons, J. P., Phys. Chem. Chem. Phys. (2001), 3, 1819-1826.
42. Snoek, L. C., Robertson, E. G., Kroemer, R. T., and Simons, J. P., Chem. Phys. Lett. (2000), 321, 49-56.
43. Grace, L. I., Cohen, R., Dunn, T. M., Lubman, D. M., and de Vries, M. S., J. Mol. Spectrosc. (2002), 215, 204-219.
44. Hunig, I. and Kleinermanns, K., Phys. Chem. Chem. Phys. (2004), 6, 2650-2658.
45. Chin, W., Mons, M., Dognon, J. P., Piuzzi, F., Tardivel, B., and Dimicoli, I., Phys. Chem. Chem. Phys. (2004), 6, 2700-2709.
46. Chin, W., Mons, M., Piuzzi, F., Tardivel, B., Dimicoli, I., Gorb, L., and Leszczynski, J., J. Phys. Chem. A (2004), 108, 8237-8243.
47. Linder, R., Nispel, M., Haber, T., and Kleinermanns, K., Chem. Phys. Lett. (2005), 409, 260-264.
48. Chin, W., Mons, M., Dognon, J. P., Mirasol, R., Chass, G., Dimicoli, I., Piuzzi, F., Butz, P., Tardivel, B., Compagnon, I., von Helden, G., and Meijer, G., J. Phys. Chem. A (2005), 109, 5281-5288.
49. Lesarri, A., Cocinero, E. J., López, J. C., and Alonso, J. L., Angewandte Chemie - International Edition (2004), 43, 605-610.
50. Bakker, J. M., Aleese, L. M., Meijer, G., and von Helden, G., Phys. Rev. Lett. (2003), 91, -.
51. Robertson, E. G. and Simons, J. P., Phys. Chem. Chem. Phys. (2001), 3, 1-18.
52. Graham, R. J., Kroemer, R. T., Mons, M., Robertson, E. G., Snoek, L. C., and Simons, J. P., J. Phys. Chem. A (1999), 103, 9706-9711.
53. Snoek, L. C., Kroemer, R. T., and Simons, J. P., Phys. Chem. Chem. Phys. (2002), 4, 2130-2139.
54. Simons, J. P., C. R. Chim. (2003), 6, 17-31.
55. Fricke, H., Gerlach, A., Unterberg, C., Rzepecki, P., Schrader, T., and Gerhards, M., Phys. Chem. Chem. Phys. (2004), 6, 4636-4641.
56. Gerhards, M., Unterberg, C., and Gerlach, A., Phys. Chem. Chem. Phys. (2002), 4, 5563-5565.

57. Unterberg, C., Gerlach, A., Schrader, T., and Gerhards, M., Eur. Phys. J. D (2002), 20, 543-550.
58. Gerhards, M., Unterberg, C., Gerlach, A., and Jansen, A., Phys. Chem. Chem. Phys. (2004), 6, 2682-2690.
59. Carcabal, P., Kroemer, R. T., Snoek, L. C., Simons, J. P., Bakker, J. M., Compagnon, I., Meijer, G., and von Helden, G., Phys. Chem. Chem. Phys. (2004), 6, 4546-4552.
60. Dian, B. C., Florio, G. M., Clarkson, J. R., Longarte, A., and Zwier, T. S., J. Chem. Phys. (2004), 120, 9033-9046.
61. Dian, B. C., Longarte, A., Winter, P. R., and Zwier, T. S., J. Chem. Phys. (2004), 120, 133-147.
62. Dian, B. C., Longarte, A., and Zwier, T. S., Science (2002), 296, 2369-2373.
63. Okumura, M., Yeh, L. I., and Lee, Y. T., J. Chem. Phys. (1988), 88, 79-91.
64. Okumura, M., Yeh, L. I., Normand, D., Vandenbiesen, J. J. H., Bustamente, S. W., Lee, Y. T., Lee, T. J., Handy, N. C., and Schaefer, H. F., J. Chem. Phys. (1987), 86, 3807-3815.
65. Wang, Y. S., Chang, H. C., Jiang, J. C., Lin, S. H., Lee, Y. T., and Chang, H. C., J. Am. Chem. Soc. (1998), 120, 8777-8788.
66. Chang, H. C., Wang, Y. S., Lee, Y. T., and Chang, H. C., Int. J. Mass Spectrom. (1998), 180, 91-102.
67. Weinheimer, C. J. and Lisy, J. M., Int. J. Mass Spectrom. Ion Process. (1996), 159, 197-208.
68. Vaden, T. D., Weinheimer, C. J., and Lisy, J. M., J. Chem. Phys. (2004), 121, 3102-3107.
69. Weinheimer, C. J. and Lisy, J. M., J. Chem. Phys. (1996), 105, 2938-2941.
70. Shin, J.-W., Hammer, N. I., Diken, E. G., Johnson, M. A., Walters, R. S., Jaeger, T. D., Duncan, M. A., Christie, R. A., and Jordan, K. D., Science (2004), 304, 1137-1140.
71. Headrick, J. M., Diken, E. G., Walters, R. S., Hammer, N. I., Christie, R. A., Cui, J., Myshakin, E. M., Duncan, M. A., Johnson, M. A., and Jordan, K. D., Science (2005), 308, 1765-1769.
72. Dunbar, R. C., Int. J. Mass Spectrom. (2000), 200, 571-589.
73. Peiris, D. M., Cheeseman, M. A., Ramanathan, R., and Eyler, J. R., J. Phys. Chem. (1993), 97, 7839-7843.
74. Wang, L. S., Ding, C. F., Wang, X. B., and Barlow, S. E., Rev. Sci. Instrum. (1999), 70, 1957-1966.
75. Ideue, S., Sakamoto, K., Honma, K., and Clemmer, D. E., Chem. Phys. Lett. (2001), 337, 79-84.
76. Rodriguez-Cruz, S. E., Khoury, J. T., and Parks, J. H., J. Am. Soc. Mass Spectrom. (2001), 12, 716-725.
77. Danell, A. S. and Parks, J. H., Int. J. Mass Spectrom. (2003), 229, 35-45.
78. Nielsen, S. B., Lapierre, A., Andersen, J. U., Pedersen, U. V., Tomita, S., and Andersen, L. H., Phys. Rev. Lett. (2001), 8722.
79. Andersen, J. U., Andersen, L. H., Hvelplund, P., Lapierre, A., Moller, S. P., Nielsen, S. B., Pedersen, U. V., and Tomita, S., Hyperfine Interact (2003), 146, 283-291.
80. Andersen, J. U., Cederquist, H., Forster, J. S., Huber, B. A., Hvelplund, P., Jensen, J., Liu, B., Manil, B., Maunoury, L., Nielsen, S. B., Pedersen, U. V., Rangama, J., Schmidt, H. T., Tomita, S., and Zettergren, H., Phys. Chem. Chem. Phys. (2004), 6, 2676-2681.
81. Andersen, J. U., Hvelplund, P., Nielsen, S. B., Tomita, S., Wahlgreen, H., Moller, S. P., Pedersen, U. V., Forster, J. S., and Jorgensen, T. J. D., Rev. Sci. Instrum. (2002), 73, 1284-1287.
82. Nielsen, S. B., Andersen, J. U., Hvelplund, P., Liu, B., and Tomita, S., J. Phys. B-At. Mol. Opt. Phys. (2004), 37, R25-R56.
83. Talbot, F. O., Tabarin, T., Antoine, R., Broyer, M., and Dugourd, P., J. Chem. Phys. (2005), 122, -.
84. Kang, H., Dedonder-Lardeux, C., Jouvet, C., Gregoire, G., Desfrancois, C., Schermann, J. P., Barat, M., and Fayeton, J. A., J. Phys. Chem. A (2005), 109, 2417-2420.

85. Kang, H., Dedonder-Lardeux, C., Jouvet, C., Martrenchard, S., Gregoire, G., Desfrancois, C., Schermann, J. P., Barat, M., and Fayeton, J. A., Phys. Chem. Chem. Phys. (2004), 6, 2628-2632.
86. Kang, H., Jouvet, C., Dedonder-Lardeux, C., Martrenchard, S., Charriere, C., Gregoire, G., Desfrancois, C., Schermann, J. P., Barat, M., and Fayeton, J. A., J. Chem. Phys. (2005), 122.
87. Kang, H., Jouvet, C., Dedonder-Lardeux, C., Martrenchard, S., Gregoire, G., Desfrancois, C., Schermann, J. P., Barat, M., and Fayeton, J. A., Phys. Chem. Chem. Phys. (2005), 7, 394-398.
88. Nolting, D., Marian, C., and Weinkauf, R., Phys. Chem. Chem. Phys. (2004), 6, 2633-2640.
89. Oh, H. B., Lin, C., Hwang, H. Y., Zhai, H. L., Breuker, K., Zabrouskov, V., Carpenter, B. K., and McLafferty, F. W., J. Am. Chem. Soc. (2005), 127, 4076-4083.
90. Kapota, C., Lemaire, J., Maitre, P., and Ohanessian, G. o., J. Am. Chem. Soc. (2004), 126, 1836-1842.
91. Polfer, N. C., Paizs, B., Snoek, L. C., Compagnon, I., Suhai, S., Meijer, G., von Helden, G., and Oomens, J., J. Am. Chem. Soc. (2005), 127, 8571-8579.
92. Lucas, B., Gregoire, G., Lemaire, J., Maitre, P., Glotin, F., Schermann, J. P., and Desfrancois, C., Int. J. Mass Spectrom. (2005), 243, 105-113.
93. Lucas, B., Gregoire, G., Lemaire, J., Maitre, P., Ortega, J. M., Rupenyan, A., Reimann, B., Schermann, J. P., and Desfrancois, C., Phys. Chem. Chem. Phys. (2004), 6, 2659-2663.
94. Macleod, N. A. and Simons, J. P., Phys. Chem. Chem. Phys. (2004), 6, 2821-2826.
95. Lucas, B., Lecomte, F., Reimann, B., Barth, H. D., Gregoire, G., Bouteiller, Y., Schermann, J. P., and Desfrancois, C., Phys. Chem. Chem. Phys. (2004), 6, 2600-2604.
96. Lecomte, F., Lucas, B., Gregoire, G., Schermann, J. P., and Desfrancois, C., Phys. Chem. Chem. Phys. (2003), 5, 3120-3125.
97. Zhan, D., Rosell, J., and Fenn, J. B., J. Am. Soc. Mass Spectrom. (1998), 9, 1241-1247.
98. Lee, S. W., Freivogel, P., Schindler, T., and Beauchamp, J. L., J. Am. Chem. Soc. (1998), 120, 11758-11765.
99. Rodriguez-Cruz, S. E., Klassen, J. S., and Williams, E. R., J. Am. Soc. Mass Spectrom. (1997), 8, 565-568.
100. Kohtani, M. and Jarrold, M. F., J. Am. Chem. Soc. (2002), 124, 11148-11158.
101. Fye, J. L., Woenckhaus, J., and Jarrold, M. F., J. Am. Chem. Soc. (1998), 120, 1327-1328.
102. Wyttenbach, T., Liu, D., and Bowers, M. T., Int. J. Mass Spectrom. (2005), 240, 221-232.
103. Liu, D. F., Wyttenbach, T., Barran, P. E., and Bowers, M. T., J. Am. Chem. Soc. (2003), 125, 8458-8464.
104. Zwier, T. S., J. Phys. Chem. A (2001), 105, 8827-8839.
105. Iijima, K., Tanaka, K., and Onuma, S., J. Mol. Struct. (1991), 246, 257-266.
106. Jensen, J. H. and Gordon, M. S., J. Am. Chem. Soc. (1991), 113, 7917-7924.
107. Stepanian, S. G., Reva, I. D., Radchenko, E. D., Rosado, M. T. S., Duarte, M. L. T. S., Fausto, R., and Adamowicz, L., J. Phys. Chem. A (1998), 102, 1041-1054.
108. Stepanian, S. G., Reva, I. D., Radchenko, E. D., and Adamowicz, L., J. Phys. Chem. A (1998), 102, 4623-4629.
109. Blanco, S., Lesarri, A., Lopez, J. C., and Alonso, J. L., J. Am. Chem. Soc. (2004), 126, 11675-11683.
110. Stepanian, S. G., Reva, I. D., Radchenko, E. D., and Adamowicz, L., J. Phys. Chem. A (1999), 103, 4404-4412.
111. Chapo, C. J., Paul, J. B., Provencal, R. A., Roth, K., and Saykally, R. J., J. Am. Chem. Soc. (1998), 120, 12956-12957.
112. Rak, J., Skurski, P., Simons, J., and Gutowski, M., J. Am. Chem. Soc. (2001), 123, 11695-11707.
113. Price, W. D., Jockusch, R. A., and Williams, E. R., J. Am. Chem. Soc. (1997), 119, 11988-11989.
114. Xu, S., Nilles, J. M., Bowen, K. H., and, J., J. Chem. Phys. (2003), 119, 10696-10701.
115. Ramaekers, R., Pajak, J., Lambie, B., and Maes, G., J. Chem. Phys. (2004), 120, 4182-4193.

116. Jensen, J. H. and Gordon, M. S., J. Am. Chem. Soc. (1995), 117, 8159-8170.
117. Kassab, E., Langlet, J., Evleth, E., and Akacem, Y., J. Mol. Struct: THEOCHEM (2000), 531, 267-282.
118. Prabhakar, R., Blomberg, M. R. A., and Siegbahn, P. E. M., Theor Chem Acc (2000), 104, 461-470.
119. Hoyau, S. and Ohanessian, G., Chem.-Eur. J. (1998), 4, 1561-1569.
120. Hoyau, S. and Ohanessian, G., Comptes Rendus Acad. Sci. Ser. II C (1998), 1, 795-799.
121. Kish, M. M., Ohanessian, G., and Wesdemiotis, C., Int. J. Mass Spectrom. (2003), 227, 509-524.
122. Shoeib, T., Rodriquez, C. F., Siu, K. W. M., and Hopkinson, A. C., Phys. Chem. Chem. Phys. (2001), 3, 853-861.
123. Shoeib, T., Siu, K. W. M., and Hopkinson, A. C., J. Phys. Chem. A (2002), 106, 6121-6128.
124. Jockusch, R. A., Lemoff, A. S., and Williams, E. R., J. Phys. Chem. A (2001), 105, 10929-10942.
125. Jockusch, R. A., Lemoff, A. S., and Williams, E. R., J. Am. Chem. Soc. (2001), 123, 12255-12265.
126. Lemoff, A. S., Bush, M. F., and Williams, E. R., J. Am. Chem. Soc. (2003), 125, 13576-13584.
127. Lemoff, A. S. and Williams, E. R., J. Am. Soc. Mass Spectrom. (2004), 15, 1014-1024.
128. Lemoff, A. S., Bush, M. F., and Williams, E. R., J. Phys. Chem. (2005), 109, 1903-1910.
129. Ai, H., Bu, Y., and Han, K., J. Chem. Phys. (2003), 118, 10973-10985.
130. Wyttenbach, T., Witt, M., and Bowers, M. T., J. Am. Chem. Soc. (2000), 122, 3458-3464.
131. Rodgers, M. T. and Armentrout, P. B., Acc. Chem. Res. (2004), 37, 989-998.
132. Moision, R. M. and Armentrout, P. B., Phys. Chem. Chem. Phys. (2004), 6, 2588-2599.

Chapter 1

A NEW PHOTOFRAGMENT SPECTROMETER

This chapter presents the conception, operation and characterization of an electrospray (ESI) ion trap tandem mass spectrometer dedicated to structural studies of closed shell molecular ions isolated in the gas phase, using photodissociation spectroscopy. The following drawing (cf. *Fig. 1.1*) gives a schematic overview of the techniques combined together in the experiment. We first discuss some of the concepts of these techniques, along with the requirements and constraints related to photodissociation spectroscopy of closed shell molecular ions, which are important for the design of the instrument. A detailed description of the photofragment spectrometer follows, while we report thereafter operating conditions and finally some data characterizing the performances of the home-built apparatus.

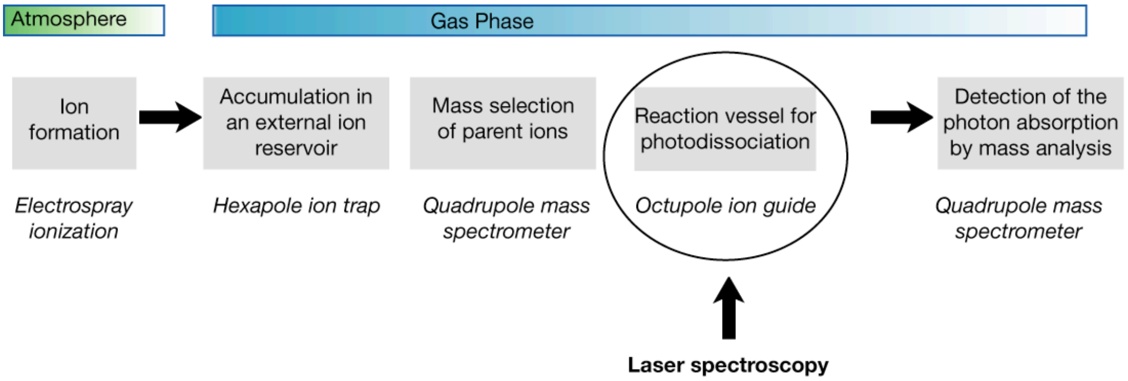

Fig. 1.1: Schematic overview of the techniques combined together.

1.1 CONCEPTION OF A PHOTOFRAGMENT SPECTROMETER FOR SPECTROSCOPIC STUDIES

1.1.1 Non-volatile closed shell ions in the gas phase and electrospray ionization

Due to its ability to bring in the gas phase large, non-volatile, charged biomolecules, we naturally oriented our choice towards the implementation of electrospray ionization (ESI) for our spectroscopic studies of biologically related ions. This ionization technique is routinely used in analytical mass spectrometry for the study of biological molecules, however its potential for spectroscopic applications was first shown on non-biologically related species by a few groups [1-4]. The flourishing number of publications especially since the beginning of this thesis work, demonstrates the importance of this technique for spectroscopic investigation of biologically related molecules [5-17].

1.1.1.1 How does ESI transfer molecular ions in the gas phase?

The earliest observation of the electrospray phenomenon was recorded in the 18th century, when the Abbé Nollet [18] discovered the effect of an electrostatic field upon human blood. However, the first description of electrospray was only made in 1917 by Zeleny [19], while Fenn and coworkers [20] demonstrated the successful implementation of this ionization method for mass spectrometric applications after the first attempt of Dole in 1968 [21]. We give here a description of the electrospray ionization process to help explain the potential of this technique for producing either bare or solvated non-volatile ions in the gas phase.

The principle is as follows: a conductive, dilute sample solution, flowing through a fine capillary (or needle) at sufficiently low flow rates ($< 20\ \mu L.min^{-1}$), can be sprayed at atmospheric pressure by the action of a strong electric field (on the order of a kV) applied between the needle and a counter electrode (cf. *Fig. 1.2*). The electric field provokes a separation of the charges in the liquid responsible for the formation of a Taylor cone at the tip of the spray capillary [22], which destabilizes the liquid and produces a spray of droplets. As the charged micro-droplets forming the spray travel towards the counter electrode under the influence of the electric field, sufficient energy is supplied through collisions with the surrounding gas at atmospheric pressure to vaporize the solvent in the droplets. The latter shrink in size until the charge density on their surface becomes large enough to reach the *Rayleigh limit*, where electrostatic repulsion forces start to overcome the surface tension.

This leads to the fission of parent droplets into highly charged daughter droplets, which undergo further solvent evaporation-droplet fission steps. Finally, this process results in droplets containing a single analyte molecule obtained either at the end of the coulomb fission cascade as described by the charge residue model [21], or by emission of ions from the surface of daughter droplets as described by the ion evaporation model [23, 24].

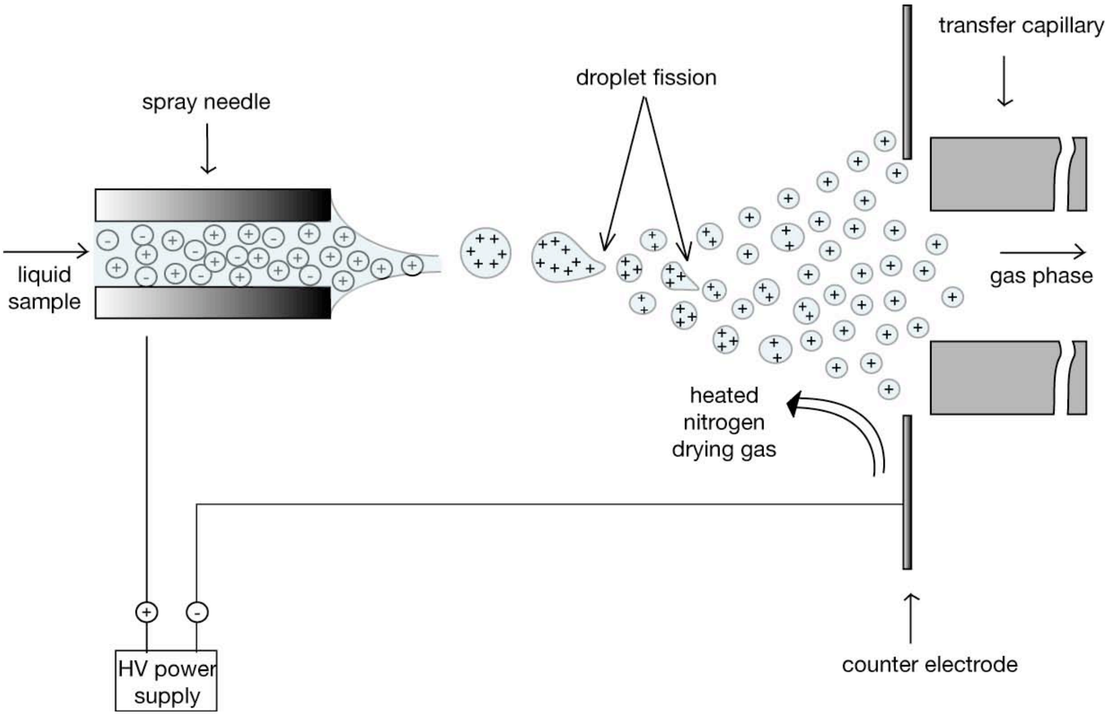

Fig. 1.2: Electrospray ionization.

Although the mechanism of ion formation is not fully understood, evidence was shown that both of the models mentioned above are valid and one may prevail over the other one, depending on the size of the molecular ion [25]. In both case, ions with a small number of solvent adducts reach the counter electrode at atmospheric pressure before they enter the vacuum interface (part of the electrospray source) through a transfer capillary. The vacuum interface is designed to achieve complete desolvation of ions by collisions with the residual gas in the first pumping stage of this region, since the electrospray ionization source is dedicated to produce adduct free species in a typical operation [26]. This interface usually comprises an ion guide to maximize the transmission of ions towards the mass analyzer.

Depending on the polarity of the voltages applied to initiate the spray either positive or negative ions can be generated. In the positive mode, the ions observed are mainly formed by proton or cation (X^+) attachment (the latter if there are salts in the sample solution) while the negative mode is more suitable for species apt to lose a proton. Small ions (such as amino acids) commonly possess a single protonation site and mainly produce $[M+H]^+$. Multiply charged ions ($[M+nH]^{n+}$, or $[M-nH]^{n-}$) tend to be formed for higher molecular masses as it is observed for proteins and typically give rise to a distribution of charge states in the mass spectra.

Even though electrospray is a ‘soft’ ionization technique based on the electrophoretic process of separation of opposite charges already existing in solution, there is some evidence that the biomolecular ions observed in ESI mass spectra are not the same as the ions preexisting in solution [2, 25, 27-29]. The charge state distributions observed for multiply charged proteins in the gas phase may not reflect the ones present in solution, mainly due to gas phase proton transfer reactions between the protein ions and solvent molecules during droplet fission or collisions in the vacuum interface [30]. Moreover, the transfer of molecular ions to the gas phase implies a change in their properties and structure: the basicity of protonation sites and electrostatic interactions between proximate charged sites may differ between solution and gas phase, thus influencing the charge states and conformations observed in the latter. For the structural studies we want to perform, this raises an important question of the relevance of the structures observed in the gas phase with respect to those existing in solution. To answer this question we produce hydrated species and probe their structure in a microsolvation environment.

1.1.1.2 Generation of bare or hydrated ions in ESI

As mentioned above, an electrospray ionization source is typically used to produce bare molecular ions for accurate molecular weight determinations. Thus, in addition to the vacuum interface which plays an important role in breaking weakly bound clusters, it is important to achieve an efficient desolvation of the droplets at atmospheric pressure before ions enter the transfer capillary. Thus, solvent evaporation from the electrospray droplets is facilitated by using a solvent of lower surface tension (typically a mixture of water with an organic content is used), but it is also assisted by a counter flow of heated nitrogen gas, which not only increases the evaporation rate of solvent in the droplets but also prevents solvent molecules from entering the vacuum interface and condensing on the ions cooled by the supersonic expansion formed at the exit of the transfer capillary.

However, electrospray ionization has been also largely employed in mass spectrometry to produce solvated species and study the influence of a microsolvation environment: large distributions of water clusters of ions result either from incomplete desolvation [31-35] or from desolvation and resolvation [11, 36-38] of the electrospray droplets in the atmospheric pressure region and further preservation of the weakly bound clusters in the vacuum interface using mild sampling conditions. A reduction of the counter-flow of nitrogen gas and its temperature together with the reduction of organic content in the solvent mixture favor the appearance of molecular ions with a number of water adducts in the mass spectra. Moreover, care should be taken to avoid large electrostatic accelerations of the ionic water clusters in the first vacuum pumping stages of the electrospray interface, where the pressure is high enough to yield energetic collisions capable of breaking apart the weakly bound complexes. Sei *et al.* [39] recently showed that cold spray ionization, a variant of ESI operating at low temperature, can favor formation of solvent clusters of ions produced during the ionization process. Another approach to favoring formation of solvent clusters of molecular ions consists in supplying solvent vapor in the vacuum interface of the electrospray source [40], although Williams and coworkers [41] have shown that in both of the aforementioned approaches, hydrated ions are formed via both incomplete solvent evaporation of the electrospray droplets and condensation of water molecules on ions cooled in the supersonic expansion in the electrospray interface.

1.1.1.3 Nanoelectrospray ionization

We produce hydrated ions by incomplete desolvation of the electrospray droplets, which is facilitated by spraying solutions from pure water. However, pure water is not a suitable solvent in conventional electrospray since its high surface tension necessitates a high electric field, causing a corona discharge before disruption of the liquid, as demonstrated by the following equation [42],

$$V_{on} \approx 0.2\sqrt{r\gamma}\ln\left(\frac{4000d}{r}\right) \qquad \textit{Eq. 1.1}$$

where V_{on} (kV) is the potential needed to initiate the spray at a distance d (mm), using a needle of radius r (μm) and a solvent of surface tension γ (N/m).

It appears that smaller diameter spray needles can be used to spray solvents characterized by a high surface tension such as water and allow reduction of the onset voltage for electrospray. Thus, nanoelectrospray ionization sources, which differ from electrospray by the use of narrower spray needles, appear to tolerate solvents of higher surface tension, but also higher concentrations of salts in the solution [43]. They lead to the formation of smaller droplets (~200 nm vs. 1-2 μm in diameter), allowing operation at reduced flow rates (~ 10 – 50 nL.min^{-1}).

The ability to spray solutions out of pure water is of great importance for our structural studies on biologically related molecules, since these species retain their structural and functional properties only in physiological conditions, namely in an aqueous environment.

Thus, nanoelectrospray ionization is not only suitable for microsolvation experiments, but also for the investigation of weakly bound complexes of analyte with metal ions, which are important in biology (cf. *Introduction*)

1.1.1.4 Ion currents and ionization efficiency

The ionization efficiency of the source controls the number of ions produced in the gas phase, which in turn determines the ion densities available for spectroscopic measurements. For instance, a 10 μM solution of amino acid infusing at a flow rate of 2μL.min^{-1} in an ESI source gives rise to a flux of singly charged ions on the order of 2.10^{11} cps. Mann and coworkers [44] report the detection of 1 out 200 000 electrosprayed molecular ions in a triple stage quadrupole mass spectrometer, which means that for the above example we should expect 10^6 cps on the final detector. On the other hand, a nanospray ionization source operating in the nL/min regime, produces a flux of ~2.10^9 cps from a 10 μM solution of amino acid (singly charged) flowing at 20nL/min. Despite the reduction of flux of two orders of magnitude relative to electrospray ionization, a 500 times higher ionization efficiency has been reported for nanospray by Mann and coworkers [44]. This represents, in our example, 5.10^6 cps on the detector, which means that nanospray ionization yields similar, or better, ion densities as electrospray and can be used for spectroscopic experiments.

However, the ionization efficiency is largely dependent on the nature of the species electrosprayed (gas phase basicity, hydrophobicity, molecular conformation), as well as on the solution conditions such as the analyte concentration showing a linear dependence within broad range of concentrations (10^{-7} M to 10^{-3} M), the solution pH, which affects the propensity of the analyte to get charged, and the solution conductivity, which might prevent the formation of the Taylor cone in solutions of too high conductivity when there is high concentrations of salts.

Electrospray ionization is versatile enough to produce a broad range of species of biological interest in the gas phase and offers an important potential for spectroscopic investigations of the species produced. One important advantage of such a source is that it produces ions in the gas phase with low enough internal energies [45] so that no fragmentation occurs under mild vacuum interface conditions.

1.1.2 Photodissociation spectroscopy of ions

The relatively low density of ions in the gas phase eliminates the possibility of using direct absorption spectroscopy. Knowing that the maximum ion density is determined by space charge effects and is on the order of $n_{max} \sim 10^6$ cm^{-3}, the maximum intensity variation (δI) expected in an absorption experiment is given by the Beer-Lambert law $\delta I/I = n_{max} l \sigma_{IR}$ and is estimated to be $\delta I/I < 10^{-11}$, assuming an infrared cross section $\sigma_{IR} \sim 10^{-18}$ cm^{-2} and a length of interaction, $l \sim 10$ cm. This requires a more sensitive action spectroscopy, in which one detects any consequence of the photon absorption. An extremely sensitive way of doing this is to measure the production of molecular fragments upon photon absorption, since daughter ions can be detected with efficiencies close to unity. Thus, photodissociation of molecular ions allows one to extract spectroscopic information and hence constitutes the heart of our experiment.

Lasers have been invaluable tools for the study of molecular ions as spectroscopic light sources, since they provide beam qualities carrying high photon fluxes, which help to compensate for the existing low ion concentrations. Although lasers can pump a considerable amount of energy into a molecule, allowing it in principle to reach the dissociation threshold, the success of photofragmentation spectroscopy relies upon achieving sufficientlty fast unimolecular dissociation rates so that photofragmentation can be detected within the time frame defined by the experiment. The ability to photodissociate the molecule depends mainly on the intrinsic spectroscopic properties of the molecular ion and the amount of energy deposited in the molecule. These aspects are discussed in more detail in *Chapter 2*, along with a description of the spectroscopic experiment. CW sources offer high laser fluences (J.cm^{-2}) insofar as ions experience long irradiation times (several seconds or minutes), even with low laser intensities (W.cm^{-2}). However these sources are only appropriate in trapping experiments where a long interaction time (> seconds) can be achieved between the ions and the laser radiation, although activation rates compete with radiation processes at these timescales. On the other hand, pulsed lasers are preferred for activating ions in flight, since excitation occurs before the molecule has time to irradiate. All laser sources used for the present work are nanosecond pulsed lasers, and the laser setup used to generate the IR radiation of sufficient power is also described in *Chapter 2*.

The ability to monitor photodissociation is of special importance for the design of the apparatus, as developed in the following paragraph.

1.1.3 Ion guide photofragment tandem mass spectrometry for spectroscopic studies

Tandem mass spectrometry is well-suited to performing photofragmentation spectroscopy of molecular ions [1, 46-49] as demonstrated on non biologically related molecules. With two mass selection stages it allows for separation of the species of interest from the ion beam for subsequent photodissociation, and mass analysis of the charged fragments upon photon absorption. However, the potential of such a technique for spectroscopic studies of biomolecular ions had not been realized at the time this thesis work was undertaken, although the implementation was straightforward with the development of electrospray ionization. Thus, we built a tandem ion guide mass spectrometer as a tool for laser photofragmentation spectroscopic studies of biologically related ions.

As depicted in *Fig. 1.3*, the apparatus consists of (1) a nanelectrospray ionization source, (2) a radiofrequency hexapole, part of the electrospray interface, typically used in commercial sources to focus the ion beam, (3) a quadrupole for mass selection of parent ions; (4) an octopole ion guide serving as the interaction region with the laser radiation, (5) and a final quadrupole for mass analysis of the products of photofragmentation as a function of wavelength. (6) Two electrostatic quadrupole deflectors bend the ion beam 90° providing a clear path for laser radiation, while a stack of electrostatic lenses at the exit of the first bender allow to refocus and decelerate the ions into the octopole ion guide.

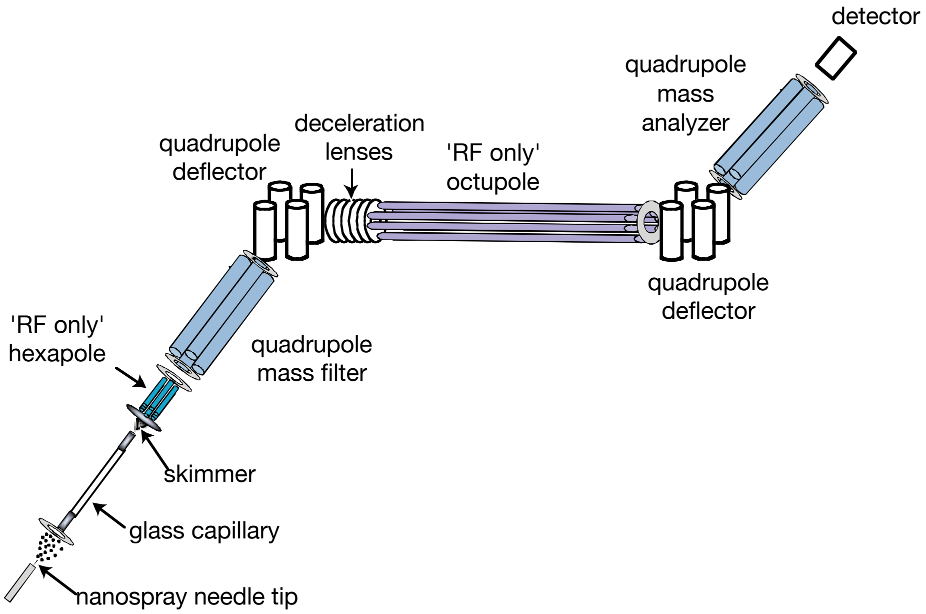

Fig. 1.3: Photofragment spectrometer.

As discussed in *§1.1.1.1*, electrospray ionization allows one to generate the ions of interest in the gas phase. It is generally coupled to a quadrupole mass spectrometer in commercial instruments, as discussed further in this section. Since the instrument is devoted to spectroscopic studies using a pulsed laser, the rf-only hexapole is meant to operate as an external ion reservoir to transform the continuous ion signal of the electrospray source into a pulsed ion signal, which can be synchronized with the laser pulses; while the octopole ion guide was selected for its capability to guide not only the parent ions, but also the fragments produced by photodissociation. Both of these features are discussed below in more detail.

1.1.3.1 Rf-only devices

1.1.3.1.1 Octopole

The rf-only linear octopole constitutes the central part of the instrument: it serves as the interaction region between the laser light and the molecular ions, and should guide all ions, both parents and photofragments, to the final mass spectrometer. The following discussion describes the properties of an rf-only octopole that make it suitable for our spectroscopic experiment.

The pioneering work of Teloy and Gerlich, [50, 51] revealed the importance of the ion guiding and trapping properties of higher order multipole fast oscillating fields. In particular, rf-only octopoles have served as a reaction vessel for dissociation [10, 38, 52-54] and spectroscopic experiments, with a large contribution of the work of Lee and coworkers devoted to lifetime measurements of excited states of ions [46, 55] and vibrational spectroscopy of ionic clusters [56-59]. More recent contributions have been made by Posey and coworkers [1, 60].

The effective potential

The motion of a charged particle in a time- and space-varying force field is described by non-linear coupled differential equations, which cannot usually be solved exactly. However, in the hypothesis of a smooth spatial inhomogeneity of the electric field and a fast oscillation frequency relative to the ion velocity [61], the equation of motion reduces to a simple equation of a particle moving in a field derived from an effective potential. The form of the effective potential depends on the geometry of the electrode arrangement. For a multipole device consisting of $2n$ cylindrical electrodes equally spaced on an inscribed circle of radius r_0, a potential $\Phi_0 = V_0 \cos(\Omega t)$, of a frequency Ω and amplitude V_0 is applied with opposite phase to alternate rods producing an effective potential given by [61]:

$$U_{eff}(r) = \frac{1}{4} n^2 \frac{q^2 V_0^2}{m\Omega^2 r_0^2} \left(\frac{r}{r_0} \right)^{2n-2} \qquad \textit{Eq. 1.2}$$

where m is the mass of the particle and q its charge.

Due to the cylindrical symmetry of the electrode arrangement, the effective potential confines the ions radially, transverse to the axis of the multipole over a broad range of masses without affecting the axial ion motion.

The mass dependence of the effective potential implies that species of different masses traversing the multipole experience a different effective potential. Since the latter is inversely proportional to the mass, products of photofragmentation of lower masses will experience a deeper potential well than their heavier parents. Moreover, transmission of heavier ions necessitates a higher RF amplitude V_0 than needed for light ions, and also a lower frequency, Ω.

In the particular case of an octopole (n=4), the effective potential varies as $(r/r_0)^6$ providing a wide potential well (four times deeper than the well of a quadrupole) with steep walls (cf. *Fig. 1.4*). Thus, the large field free region offers a large volume for confining the ions before space charge effects become important and does not perturb the energy of the ions except for the small perturbations of the kinetic energy in the high field region close to the electrodes.

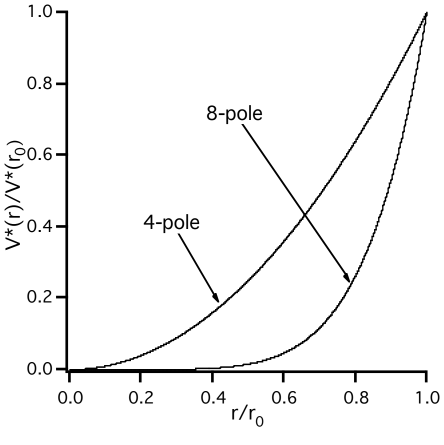

Fig. 1.4: Effective potential in a quadrupole and octupole.

Operating conditions

Under the conditions stated above, ions experience the time-averaged force of an overall effective potential and can be guided towards the exit of a multipole. However, safe transmission without loss of ions by collisions with the rods requires an additional condition concerning the total transverse energy E_m of ions inside the multipole. If this energy remains low enough so that ions stay in the well created by the effective potential, then the stability condition is fulfilled insuring bound trajectories within the poles.

Thus, based on the aforementioned conditions, two practical criteria (cf. *Eq. 1.3* and *Eq. 1.4*) have been defined by Teloy and Gerlich [50, 61] to estimate the minimal amplitude V_0, and frequency $f=\Omega/2\pi$ necessary to apply to the multipole rods to transmit a certain mass range of ions for a given multipole electrode geometry and for a given transverse energy E_m:

$$qV_0 \geq 8\frac{n-1}{n}\frac{E_m}{0.3.(0.8)^n} \quad \textit{[units V, eV]} \qquad \textit{Eq. 1.3}$$

$$\Omega^2 \geq 268.125\frac{(n-1)^2}{mr_0^2}E_m \quad \textit{[units MHz, amu, cm, eV]} \qquad \textit{Eq. 1.4}$$

where q, and m are the charge and mass of the particle, $2n$ the number of poles, r_0 is the inscribed circle radius of the multipole arrangement.

Equation 1.4 clearly shows how the operating frequency turns a multipole into a wide band pass filter. Indeed, depending on the number of poles, a range of masses can be transmitted simultaneously under safe conditions for a fixed frequency.

We use the above equations in the particular case of an octopole in order to determine the minimum amplitude, V_0, and minimum RF frequency necessary to guide ions without losses, taking into account our aim of building an instrument versatile enough to study a wide variety of species, ranging from amino acids and their water clusters to larger molecules such as peptides or proteins. Since the latter are multiply charged ions with higher masses they require lower RF amplitudes and threshold frequencies, while amino acids, which are typically singly charged and lighter, define the threshold values necessary to apply on the multipole to transmit the whole mass range of interest. We thus set $q = 1$ and $m = 200$ amu in the above equations. Ions produced by electrospray ionization possess an initial kinetic energy, when delivered in the mass spectrometer, which is defined in the vacuum interface of the source and is on the order of a few electron volts. We assume an upper limit of $E_m = 4$ eV for the ions in the octupole. Although this value is overestimated, it helps to get an estimate of boundary values. Thus, knowing that the inscribed radius of our octopole ($n = 4$) is $r_0 = 0.48$ cm, we calculate a minimum RF amplitude calculated with the above equation of $V_0 = 195$ V and a minimum frequency $f \approx 2$ MHz.

Summary

It follows that multipoles are well-suited to guide slow ions produced by electrospray with energies of a few electron volts. The rf-only octopole offers a large field-free region (for the ions confined in the effective potential well) between the poles, which does not distort the energy of the ions, and represents a large volume -- increasing with the length of the rods – through which reactant species are guided. Finally the large potential well arising from the oscillating field permits one to collect the products of photofragmentation regardless of scattering angles, thereby enhancing the detection sensitivity.

Our octopole ion guide consists of eight parallel rods, 60 cm long, 0.32 cm in diameter, equally spaced on a 0.96 mm diameter circle, with a 2.1 MHz RF frequency allowing to transfer a wide range of masses simultaneously. In order to obtain a maximum overlap between the reactant molecules and the laser beam, we decided upon a coaxial irradiation of the ions by a laser beam propagated along the central axis, parallel with the rods of the linear ocupole. The 60 cm length of the octopole allows a large number of ions to be irradiated. Such a configuration is optimal for a collimated, or unfocused laser beam with a waist that matches the inscribed diameter of the octopole rods, however it is not ideal for experiments requiring a focused laser beam, which would result in a very small volume of interaction.

Knowing that an electrospray ionization source produces ions with a few electron volts of kinetic energy we expect an ion time-of-flight of a few hundreds of microseconds in our 0.6 m long octopole. This has been confirmed experimentally by measuring a time-of-flight of ~300 μs for protonated amino acids along the octopole ion guide. Since typical electrospray ion currents detected in a tandem mass spectrometer configuration are in the order of a few 10^6 cps (cf. *§ 1.1.1.4*), we expect a lower limit of a few hundreds of ions in the octopole guide, based on the aforementioned time-of-flight. However in a photodissociation experiment, only a fraction of this number absorbs the incident radiation and subsequently dissociates, thereby reducing substantially the number of ions yielded from photofragmentation.

As discussed below in more detail it is possible to increase the ion density in the octopole by using the rf-only hexapole in the electrospray vacuum interface as an external reservoir, where ions are accumulated before being injected in bunches into the first mass filter and subsequently in the octopole.

1.1.3.1.2 Hexapole

We have discussed so far the main advantages of using higher-order multipoles, and in particular an octopole, for spectroscopic experiments: the wide field free region and the low kinetic energy distortions offered by such devices. The wide band pass characteristics of RF-only multipoles and trapping capabilities make them well-suited as ion guides in commercial mass spectrometers [62, 63] but also as external ion reservoirs [64-66].

It is possible to operate an rf-only multipole as an ion trap simply by raising the potentials on the endcap electrodes. As part of our electrospray ionization source, an rf-only hexapole primarily focuses the ion beam emerging from the transfer capillary and redirects divergent trajectories towards the quadrupole mass analyzer, thereby improving ion transmission efficiency. The ion beam is efficiently confined close to the central axis due to the collisions experienced in the moderate pressure region of the hexapole, resulting in a substantial reduction of the ion kinetic energy.

Moreover, since ions lose some kinetic energy by collisional cooling, a trapping potential created within the hexapole by simply raising the endcap electrode voltage prevents ions from leaving the trap, while the low voltage applied at the front-end allows filling the trap with the continuous ion beam from the electrospray. Collecting the ions in the hexapole before injecting them into the photofragment mass spectrometer converts the continuous electrospray ion signal into a pulsed signal that better matches the duty cycle of a pulsed laser experiment. However, excessively long accumulation times may lead to a significant degree of fragmentation when the space charge limit is attained. This phenomenon has been described by Hofstadler and coworkers, who used it for multipole storage assisted dissociation (MSAD) studies and showed its dependence on the analyte concentration, the source ionization efficiency, and on the depth of the trapping potential well [67, 68].

Our hexapole consisting of six rods on an inscribed circle of radius r_0=0.175 cm is operated in the rf-only mode at 5.3 MHz, with a 500 V amplitude. Based on the practical criterion defined earlier (cf. *§ 1.1.3.1.1, Eq. 1.3 and Eq. 1.4*), we conclude that safe transmission and confinement of ions is possible in our hexapole with a minimum frequency of $f \approx 4.5$ MHz and amplitude of $V_0 = 139$ V to transmit a singly charged amino acid of mass m = 200 amu with $E_m = 4$ eV.

1.1.3.2 Quadrupole mass filter

1.1.3.2.1 Ion motion in a quadrupolar field

The motion of ions in a quadrupolar field is governed by the general equations of motion of an ion moving in a fast oscillating, spatially inhomogeneous electric field. Although we discussed earlier the case of octupolar fields making use of the effective potential, the quadrupolar field is a special case among other multipole geometries, insofar as the equations of motions reduce to a set of decoupled one-dimensional differential equations, called the Mathieu equations. Oscillating quadrupolar fields have received a growing interest since the discovery of their mass analyzing and ion trapping properties by Paul and Steinwedel [69].

A voltage Φ_0 composed of an RF component, $V\cos(\Omega t)$, and a DC component, U, is applied with opposite polarity to alternate rods equally spaced on an inscribed circle of radius r_0:

$$\Phi_0 = U + V\cos(\Omega t) \qquad \textit{Eq. 1.5}$$

Ions entering the quadrupole experience forces in the x and y directions transverse to the propagation direction, resulting in particular trajectories which are described by the solutions of the Mathieu equations. The latter contain either a growing exponential factor or an oscillatory term depending on the ion mass, possibly leading to stable or unstable trajectories. One important property of the Mathieu equations is that the nature of the ion motion does not depend on the initial conditions but only on two dimensionless parameters [70]:

$$a = \frac{8e}{m_i r_0^2 \Omega^2} U$$

$$q = \frac{4e}{m_i r_0^2 \Omega^2} V \qquad \textit{Eq. 1.6}$$

1.1.3.2.2 Operation of a quadrupole mass analyzer

The above parameters define the conditions leading to a stable ion motion simultaneously in the x and y direction necessary to transmit the ions through the quadrupole before they hit the electrodes. The stability regions along each direction (x or y) can be visualized in a plot of a versus q, known as the stability diagram and shown in *Fig. 1.5.* Operation of the quadrupole at a fixed RF frequency Ω, requires given values of U and V such as the corresponding point (a,q) belongs to the stability diagram, insuring a stable trajectory for a particular mass m. Mass selection is achieved by varying the voltages U and V along the ‘mass scan line’, i.e, the line of fixed slope 2U/V intersecting the stability diagram.

For each point (U,V) on the line, the ensemble of points (a,q) $\{a \in \Delta a, q \in \Delta q\}$ in the region of intersection with the stability diagram, defines a set of masses possessing stable trajectories. The mass window transmitted depends on the slope of the line which determines the resolving power of the quadrupole, defined by R=m/Δm (Δm is the full half-width at half maximum of the peak at mass m). An increased mass resolution, along with a sacrifice in transmission, are obtained for an intersection at the tip of the stability diagram where the mass window reduces to a single mass.

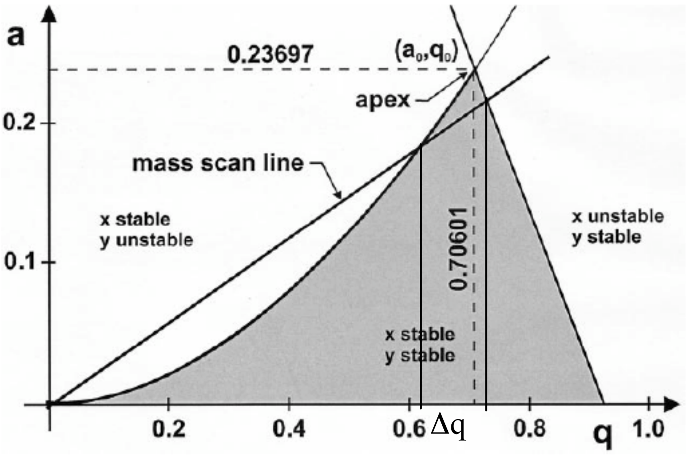

Fig. 1.5: Stability diagram of a quadrupole mass filter. Figure from K. Blaum et al. [71].

The quadrupole resolving power is mainly governed by the U/V ratio, but also depends on the number N of rf-cycles experienced by an ion during its flight time through the quadrupole [72],

$$R = \frac{m}{\Delta m} \approx N^2 / 12.25 \qquad \textit{Eq. 1.7}$$

which in turn is dependent on the axial kinetic energy (E) of the ion, the RF field frequency ($\Omega=2\pi f$), and the rod length (L), linked by the following relationship:

$$N = ft \approx fL\sqrt{\frac{m}{2E}} \qquad \textit{Eq. 1.8}$$

It thus appears that proper operation of a quadrupole mass analyzer requires a kinetic energy of the ions in the order of a few eV [71] and therefore is suitable for coupling with low energy ionization sources. Moreover, the mass range of a quadrupole is limited to 0 - 4000 amu, with a resolution lower than 5000. Electrospray ionization produces ions with the appropriate energy for mass analysis with a quadrupole and moreover generates multiply charged ions with m/z ratios falling within the detectable mass range of a quadrupole, thereby allowing mass analysis of species of molecular weights with practically no mass limit [73]. This provides good justification for coupling electrospray to quadrupole mass spectrometers.

1.1.3.2.3 Transmission

The transmission through a quadrupole mass filter is mainly controlled by the distance $2r_0$ between opposite pairs of electrodes. Although stable trajectories do not depend on the initial conditions, stability is insured only within an operating range requiring that the maximum radial displacement r_m of the ion subjected to the transversal acceleration of the RF field does not exceed r_0, the distance to the poles. Quadrupole mass filters designed with larger distances between the rods r_0 yield a better transmission. However the amplitude of r_m depends upon the combined effect of the initial ion position, ion velocity and RF field phase, implying that within a stability region only a limited number of combinations of the aforementioned factors yield 100% transmission [71, 74]. An increased resolution generally leads to smaller usable apertures and tends to decrease ion transmission. Typically, the quadrupole transmission efficiency is on the order of 30%.

Transmission of ions in a multiple stage instrument is also affected by the trajectories of ions exiting the quadrupolar field in almost any direction in the *xy*-plane. In our instrument, such a dispersion may result in severe transmission losses of the ions after the first mass selecting stage, which will dramatically reduce the number of ions in the octopole for photofragmentation.

Our quadrupole consists of 20 cm long, Ø 9.5 mm cylindrical rods with 8.5 mm inscribed radius, driven at an 1.2 MHz RF frequency with a 0 – 2000 amu mass range and is designed in such a way that it limits the aforementioned transmission losses. It consists of a central part to which the mass resolving voltages are applied, while two shorter sections, respectively at the front and back end are driven at an rf-only voltage. These sections, so-called pre- and a post- filter enhance the transmission through the quadrupole but also through the subsequent stages of the instrument by producing a more collimated beam exiting the quadrupole and directed towards the next stage.

As discussed above, operating at high resolution reduces the transmission efficiency. Since the principal function of this spectrometer is to allow for spectroscopic studies, high mass resolution may be sacrificed to gain transmission. For instance, the mass spectra of isolated amino acids produced by electrospray show under normal conditions a single peak corresponding to the singly protonated species. Thus, operation of the first quadrupole at high resolution is not essential and may be reduced at the benefit of transmission. This is also the case for water cluster distributions of singly charged amino acids, where the peaks are separated by 18 amu. However larger species exhibit a distribution of charge states on top of which a distribution of water clusters superimposes, and therefore result in a narrower separation of peaks which scales as the inverse of the number of charges q (i.e $18/q$ for the water clusters).

1.1.3.3 Quadrupole electrostatic deflector

We use two electrostatic deflectors, mainly to provide a clear path for propagating the laser beam along the octopole.

The deflector consists of four hyperbolically shaped vertical poles in a square configuration, and is typically operated by electrically connecting two diagonally opposite poles together. A static repelling voltage applied to one pair of poles and an attracting potential on the other pair result in a 90º deflection of the ion beam [75, 76] around the pole of attracting potential, while the difference in potential between two pairs of poles controls the energy window of the ion beam that can be deflected. Depending on the requirements of the experiment, we may tune the quadrupole deflector for high transmission and low energy discrimination, or tune it to perform as an energy band pass.

A quadrupole deflector provides an elegant way for merging the laser radiation with the ion beam [77], but also constitutes an important feature in the design of our photofragment spectrometer, since it allows deflection of the ion beam in two opposite directions by reversing the potential applied on each pair of poles. Hence the first bender offers the capability to bend ions either towards the octopole or towards a first detector used for tuning the instrument voltages to probe ion transmission along the first stage of the mass spectrometer (cf. *§ 1.3.1.4)*. Finally, it plays an important role in the separation of the ion beam from the neutrals transmitted from the source through the linear configuration of the first stage of the mass spectrometer as discussed in *§ 1.2.3*.

1.2 A HOME BUILT ESI ION TRAP TANDEM QUADRUPOLE MASS SPECTROMETER

We present here a detailed description of the apparatus, composed of a commercial electrospray ionization source and a custom-designed vacuum system, which houses the components of the ion guide tandem mass spectrometer according to the configuration of *Fig. 1.3* and takes into account the design considerations discussed so far.

1.2.1 Electrospray ionization

The home-built ion guide tandem mass spectrometer is equipped with a commercial electrospray ionization source (Analytica of Branford Inc., CT). At atmospheric pressure, the electrospray source head can be interchanged with a commercial nanoelectrospray ionization source head (Model ES025A, for Finnigan TSQ/SSQ mass spectrometers, delivered by Proxeon Biosystems, Dk) by means of a home made adapting piece. The nanoelectrospray ionization source was integrated afterward in the instrument, since it appeared more robust and stable to generate water clusters for the microsolvation experiments described in *Chapter 2*.

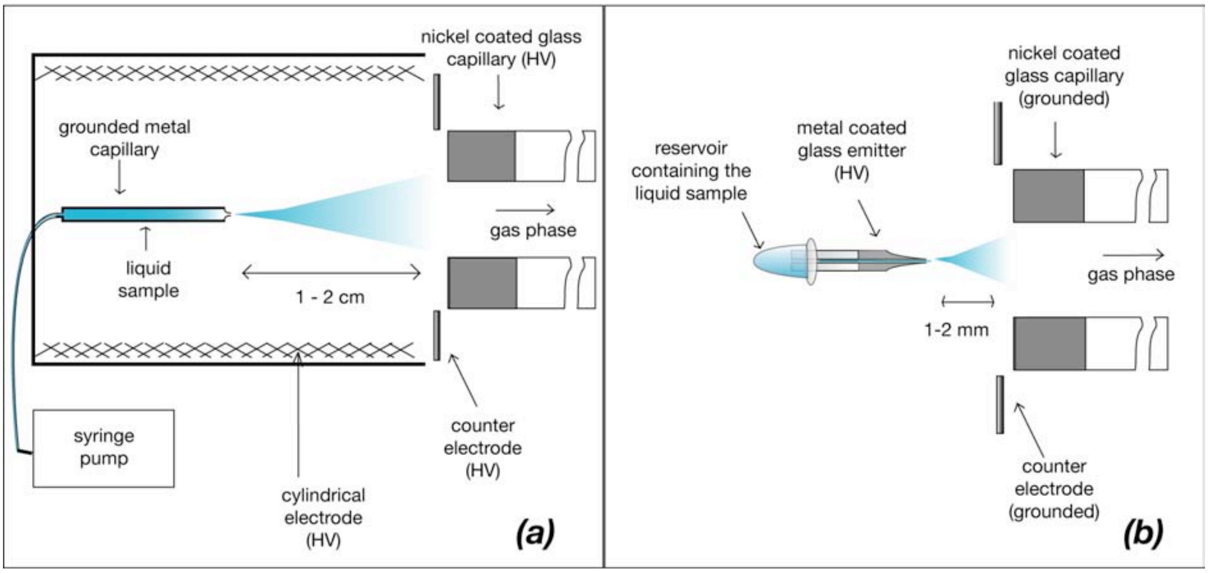

Fig. 1.6: Schematic of the (a) electrospray source and (b) nanospray source.

The atmospheric part of the electrospray source (*Fig. 1.6 (a)*) comprises a metal capillary serving as the spray needle, a cylindrical electrode and a counter electrode, which help shape the electric field and initiate the spray, and a nickel coated glass capillary that transfers the ions from atmospheric pressure to vacuum. The liquid sample is forced through the spray needle (~110 μm ID), by a syringe pump (KDS101, KD Scientific) at flow rates of 1 – 2 μL/min. The position of the latter, fixed on a manipulating mounting block, can be adjusted in the *x*, *y* and *z* directions. The needle is typically grounded, and a negative high voltage is applied to the nickel-coated glass capillary inlet (~3 kV) in order to attract the positive ions at the entrance of the vacuum system. Solutions for electrospray ionization are typically prepared by dissolving the analyte in a solvent mixture of 1:1 methanol/water (0.1% acetic acid) in order to obtain concentrations of 10 or 100 μM.

In the nanoelectrospray source (*Fig. 1.6 (b)*), the sample is loaded directly in a metal-coated (Au/Pd coating) borosilicate capillary emitter (~ 50 mm long, 1.2 mm OD, 0.7 mm ID, ~1 μm ID of spraying orifice) serving the role of the above-mentioned electrospray needle. Contrary to conventional electrospray, the spray is generated strictly by electrostatic means; no syringe pump is used and the liquid flow is driven solely by capillary forces through the emitter, which is immersed in an Eppendorf micro test tube reservoir containing the rest of the solution. The whole assembly is mounted on an *xyz*-micromanipulator for precise adjustment of the spray capillary tip relative to the glass capillary inlet. As opposed to the electrospray source, the spray is initiated by applying a high voltage (~1 kV) at the emitter tip, while the metal-coated inlet of the glass capillary is grounded, and the intermediate electrodes used to shape the electric field are removed. Moreover, the source includes two CCD cameras (with adjustable focal length, magnification up to × 60) allowing for the visualization of the spray. The flow rates of our source are between 10 and 40 nL/min depending on the nanoES emitter tip opening internal diameter. This source allows one to spray aqueous solutions of analyte prepared in pure water without addition of organic solvent.

Ions generated either by the electrospray or the nanospray ionization source enter the electrospray interface vacuum region (which is part of the commercial source Analytica of Branford Inc., CT) through the transfer glass capillary.

1.2.2 Electrospray interface

The electrospray interface is the region between atmospheric pressure and the first quadrupole mass spectrometer (cf. *Fig. 1.7*). It comprises a glass capillary (600 μm I.D aperture, 240 mm long), a skimmer cone, and an rf-only hexapole ion guide (6.2 cm long, Ø 1 mm rods, 5.3 MHz) with an endcap electrode.

Electrosprayed ions enter the glass capillary from the inlet at atmospheric pressure and are drawn in the vacuum system by viscous forces against the potential barrier. A supersonic expansion takes place at the back end of the capillary in the first stage of differential pumping between the capillary exit and a skimmer cone (Ø 1.2 mm), where a mechanical pump (Alcatel, Model 2063, 60 $m^3.h^{-1}$) maintains a pressure of 1 – 2 mbar. The metal-coated capillary exit acts itself as an electrostatic lens, and ions can be accelerated and focused through the skimmer. The acceleration potential in this region should not exceed ~100 V in order to avoid energetic collisions with neutrals in this moderate pressure region. Only the core of the free jet expansion passes through the skimmer orifice (Ø 1.2 mm) towards the hexapole. The latter traverses two stages of differential pumping defined between the skimmer cone and the hexapole exit lens, separated by the hexapole mounting-flange. A turbo-drag pump (60$L.s^{-1}$, TMU 071 P, DN 63 CF-F with TC 100, Pfeiffer Vacuum, DE) maintains a pressure of 2.10^{-3} mbar in the high-pressure end of the hexapole, while a bigger turbo-drag pump (520$L.s^{-1}$, TMU 521 DN 160 CF-F, Pfeiffer Vacuum, DE) evacuates the low-pressure end at 5.10^{-5} mbar. The continuous ion signal generated by the electrospray ionization source, is accumulated and confined in the rf-only hexapole by raising the voltage applied on the hexapole exit lens. Ions trapped in this external ion-reservoir for appropriate periods of time are subsequently released in the tandem photofragment mass spectrometer for parent mass selection, photodissociation and photofragment detection.

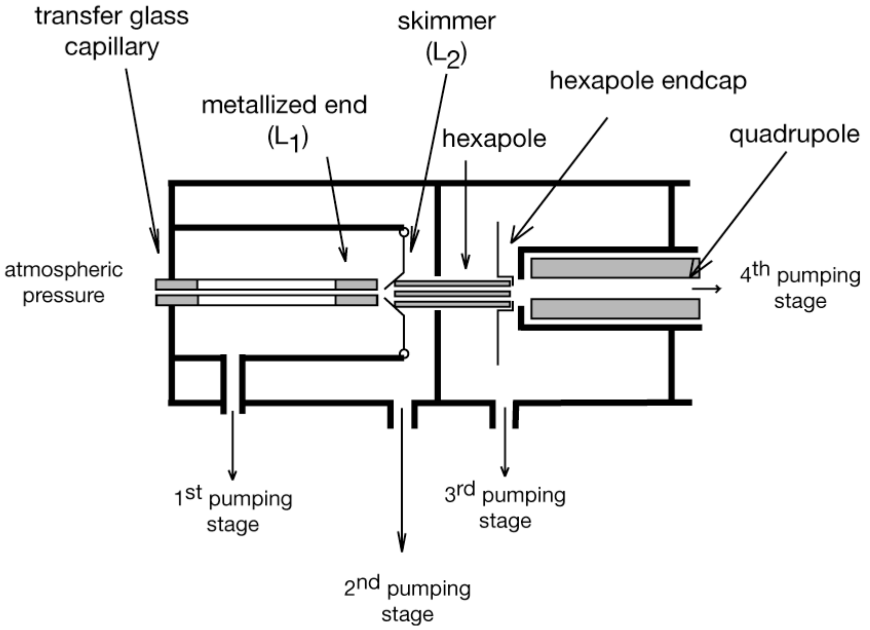

Fig. 1.7: Electrospray interface.

1.2.3 Vacuum system

A custom vacuum system was designed[1] to house the components of the tandem ion guide mass spectrometer and was specially adapted to fit the electrospray interface.

As discussed in *§ 1.1.2,* the successful implementation of the spectroscopic experiments we wish to perform relies upon the ability to dissociate the parent ion beam and efficiently detect the products of photofragmentation. The design of the photofragment spectrometer requires a very high vacuum in the region between the two mass selecting stages and especially in the region of interaction with the laser radiation in order to avoid collisions with the background gas molecules and allow to extract the spectroscopic information. Collisions with residual molecules can either lead to collision induced dissociation of the parent ions, deactivation of the laser excited molecules, or possible loss of the generated fragments through ion-molecule reactions. Thus, it is important to eliminate these

---

[1] Sébastien Mercier, PhD student in LCPM, EPFL.

processes, which would compete with the exclusive production of fragments by laser excitation and therefore bias the measurement of the spectrum. Pressures in the order of ~10^{-9} mbar result in ~ 5.10^{6} cm mean free path, which is largely above the dimensions of the instrument and provides a suitable collision free environment.

The vacuum chambers are manufactured in stainless steel (Just Industry, DE) and surfaces are treated by bead blasting for ultra high vacuum compatibility to reduce the adsorbing area of the metal surface so that low outgassing rates can be obtained. Moreover, all vacuum chambers, and vacuum components are cleaned to remove traces of hydrocarbon oils, inorganic salts or water adsorbed on the surface and degassing during pumping. In order to preserve a clean vacuum environment and avoid hydrocarbon contamination from pump oil, turbomolecular pumps backed by membrane pumps are used to evacuate the chamber.

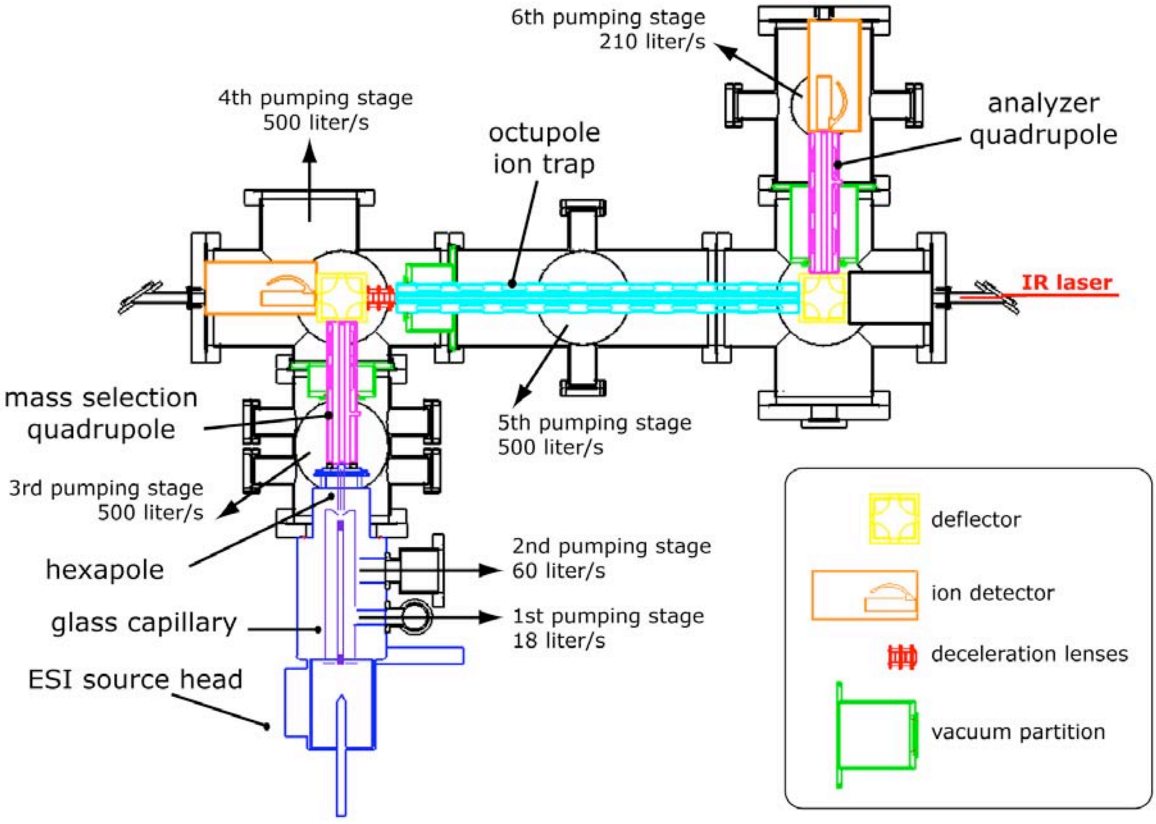

Fig. 1.8: Drawing of the vacuum chamber with the different ions optics components.

Our vacuum system is composed of six differentially pumped stages, through which ions are driven by forces of static and oscillating electric fields towards the detector, as shown in *Fig. 1.8.*

Besides the three vacuum stages of the commercial electrospray source, three more differential pumping stages have been designed to achieve high vacuum in the tandem ion guide mass spectrometer. Thus, the 3rd pumping stage of the electrospray interface (cf. *§ 1.2.2*), evacuating the low pressure region around the hexapole, is housed in the first chamber of our vacuum system, while a vacuum partition separates it from the 4th pumping region including the first mass selecting quadrupole, the first bender with the decelerating electrodes, and the first detector. This chamber is differentially pumped to 2.10^{-6} mbar, by a turbo-drag pump ($520L.s^{-1}$, TMU 521 DN 160 CF-F, Pfeiffer Vacuum, DE) positioned behind the bender, on the path of neutral molecules originating from the source. Indeed, the linear configuration of the ion source with the first quadrupole mass filter allows also transmission of some neutral molecules entrained with the flow of ions through the glass capillary. The neutrals are not affected by the electric field, and are efficiently removed from the ion beam through the bender, since they are not deflected but are efficiently pumped by the on-axis pump. This results in a better differential pumping in the 5th stage, allowing us to reach high vacuum in the region of the octopole and the second deflector, maintained at a pressure of 3.10^{-8} mbar by a turbo-drag pump ($520L.s^{-1}$, TMU 521 DN 160 CF-F, Pfeiffer Vacuum, DE). Due to the length of the octopole, the remaining stages of the spectrometer represent a large volume to evacuate, and the last vacuum partition was designed to evacuate the region of the second quadrupole analyzer and the final detector, and preserve low pressures (2.10^{-8} mbar) using a turbomolecular pump (230 $L.s^{-1}$, TMU 261 DN 100 CF-F, Pfeiffer Vacuum).

All components of the tandem mass spectrometer (mass resolving quadrupoles, benders, octopole ion guide, detectors and ion optics) with their corresponding electronics and the operating system (Merlin version 1.015) have been purchased from Extrel CMS, USA. The commercial software Merlin Automation controls the operation and tuning of the voltages of the ion guide tandem mass spectrometer, together with the display and acquisition of mass spectra in the absence of laser light. However due to synchronization of the data acquisition with the laser timing during a laser scan, the photofragmentation spectra are acquired through an independent data acquisition system controlled by a custom Labview program (cf. *Chapter 2*).

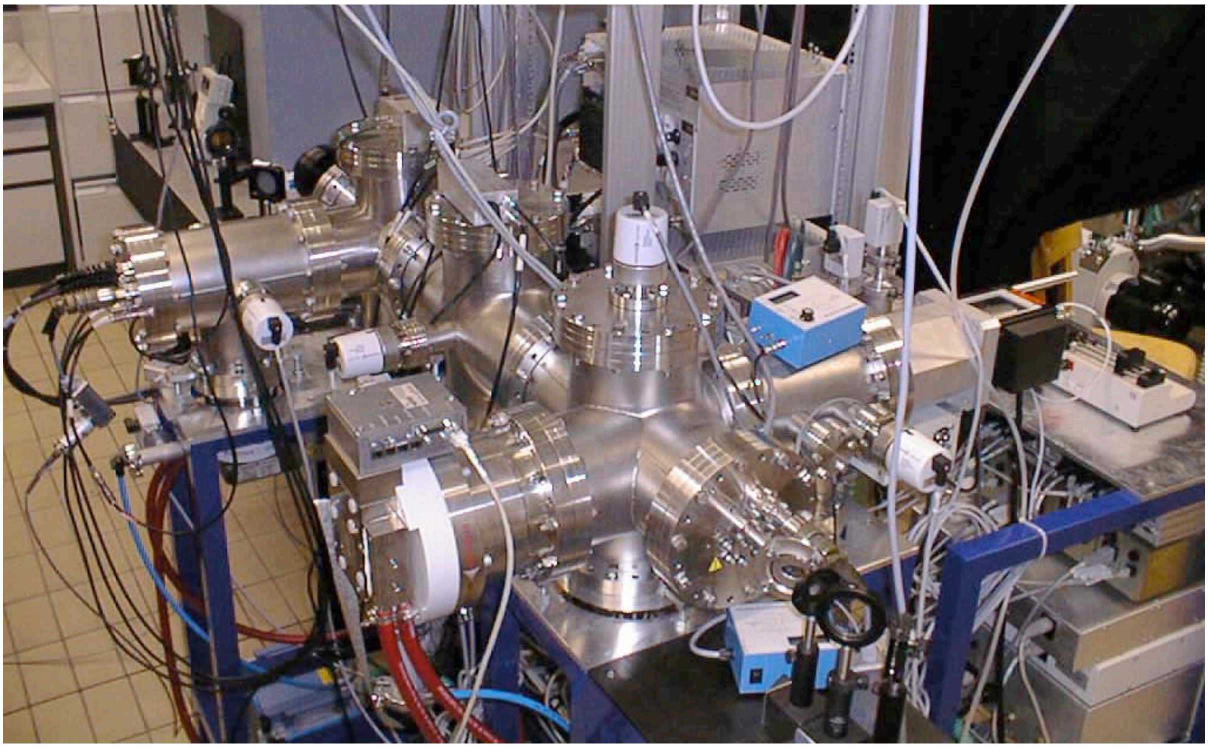

Fig. 1.9: Picture of the photofragment spectrometer.

1.2.4 Summary

Electrospray ionization continuously produces ionic species at atmospheric pressure, which are transferred into vacuum through a transfer glass capillary and accumulated in an external ion reservoir (hexapole) prior to mass analysis. The pulsed ion signal resulting from accumulation in the hexapole trap traverses a first quadrupole mass filter (20 cm, Ø 9.5 mm rods, 1.2 MHz, 0-2000 a.m.u mass range) for mass selection of the parent ions, which are deflected through the bender, and subsequently refocused and decelerated by a stack of five cylindrical electrodes (Ø 12.7 mm aperture) prior to entrance in the rf-only octopole ion guide (Ø 3.175 mm rods, 60 cm long, 2.1 MHz, Ø 9.5 mm of the inscribed circle). Photodissociation takes place in the octopole by propagating the laser beam along the axis of the ion guide through BaF_2 windows at the Brewster angle. The second electrostatic bender at the output of the octopole deflects the ion beam 90º to deliver the products of photodissociation to the final mass resolving quadrupole, which are detected by a pulse counting Channeltron electron multiplier with a conversion dynode.

1.3 OPERATION CONDITIONS AND CHARACTERIZATION OF THE SPECTROMETER

1.3.1 Simion simulations

We used the software package SIMION 3D Version 7.0 (Idaho National Laboratory, Idaho Falls, ID) [78] to model ion trajectories in the high vacuum part of our instrument from the first quadrupole to the final analyzing quadrupole. The goal of the simulations is to explore different conditions (i.e., sets of voltages) necessary to transfer ions through the photofragment spectrometer ion optics, and to identify the elements critical for ion transmission.

Ion trajectory simulations using SIMION require: (1) drawing the ion optics; (2) applying the appropriate potentials on the different electrodes and letting the software solve the Laplace equation to determine the potentials in the spatial region between the electrodes; (3) defining a group of ions characterized by a certain mass, kinetic energy, initial positions and velocity components, and visualizing the ion motion in the electric field created by the different ion optics.

1.3.1.1 Ion optics modeled in Simion

The different components of the instrument modeled for simulations appear in *Fig. 1.10* and comprise both quadrupole mass analyzers (Q_1, Q_2) with their respective electrostatic entrance and exit lenses (Q_{1in}, Q_{1out} and Q_{2in}, Q_{2out}), both benders (B_1 and B_2), each including two pairs of poles (B_1^-, B_1^+ and B_2^-, B_2^+) and two pairs of electrostatic lenses (named for convenience B_{1in}, B_{1out} and B_{2in}, B_{2out}), the stack of five electrostatic lenses (L_1-L_5) and finally the octopole ion guide with its entrance and exit lenses (O_{in} and O_{out}) (cf. *Appendix*).

Note that all multipole assemblies possess electrically isolated entrance and exit electrodes, which serve to minimize fringe field effects by accelerating ions in the boundary regions of the multipole. Similarly the quadrupole deflector possesses four lenses located on the axes of the gaps between the four vertical rods of the bender to minimize the fringe fields at the entrance and exit of the ion beam. The deflector entrance lens is electrically connected to its opposite counterpart and held at a potential which is half-way between the potential of the poles, while an independent voltage is applied to the remaining pair of lenses to aid in shaping the emergent ion beam.

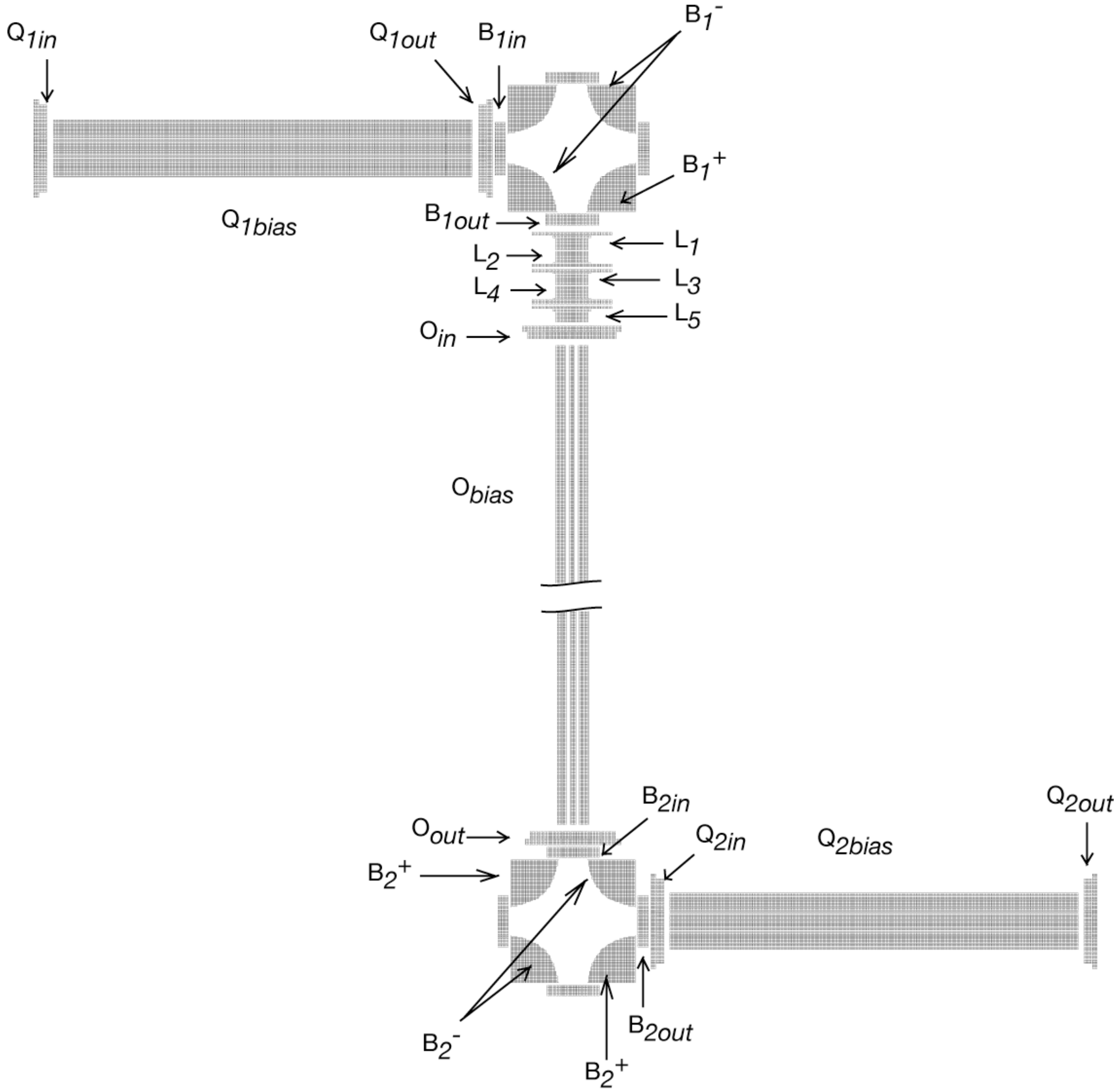

Fig. 1.10: Schematic of the ion optics.

To have realistic simulations, we reproduced within SIMION the exact electrode geometries of the instrument components based on drawings provided by *Extrel CMS*.

1.3.1.2 Electrostatic and time-dependent voltages

All of the aforementioned ion optics are operated by electrostatic voltages, except for the rods of the quadrupole mass analyzers, the RF-only octopole, which employ time-dependent electric fields for mass analysis and ion guiding. On top of the time-dependent voltage, a static bias voltage can be applied on the rods of each multipole (O_{bias}, Q_{1bias}, Q_{2bias}) allowing one to offset the potential on the central axis between the poles with respect to ground and thereby change the axial ion kinetic energy within the multipole.

The electrostatic voltages of the different ion optics are defined as adjustable parameters in the simulations and can be optimized for maximum ion transmission, within the physically accessible voltage range defined by the electronics. On the other hand, time-varying potentials applied on the rods of the multipoles comply with the manufacturer RF- frequency and amplitude specifications, while proper waveforms and constraints are defined for the operation of the octopole as an ion guide and the quadrupole as a mass filter.

1.3.1.3 Tuning voltages and probing different initial conditions

A considerable number of independent voltages seems to control the efficient transmission of the ion beam through the different stages of the instrument, and this makes it difficult to find the appropriate set of parameters that maximizes the ion signal at the final detector. Nevertheless, the ability to visualize ion trajectories significantly aids in understanding the effect of changing the voltage on a particular element and therefore develops intuition for tuning the voltages in the real instrument.

Ions are generated in the simulations with random time of birth, initial position, velocity components and kinetic energy within an acceptable range in order to reproduce the dispersion of the beam originating from the ion source. It is thus possible to identify the critical parameters affecting the ion trajectories by probing a wide range of initial conditions, while tuning the voltages in parallel to restore favorable conditions for transmission of the ion beam allows one to identify those voltages to which ion trajectories are most sensitive.

1.3.1.4 Results

Fig. 1.11 shows the result of a SIMION trajectory simulation for ions born in the quadrupole region with an initial 5 eV kinetic energy, a 10 % spread in ion kinetic energy, a 2º cone angle divergence and a maximum offset of 1 mm with respect to the central axis. Visualization of the ion trajectories revealed the several important features concerning the ion transmission.

The potentials on the turning quadrupoles are critical for good ion transmission. Losses in the first bender come from destabilization of the ion trajectories at the exit of the quadrupole mass filter or in the case of the second bender, at the exit of the octopole ion guide, due to fringe field effects that cause divergence of the ion beam. This divergence is amplified by the turning quadrupole, which does not possess any focusing properties in the direction orthogonal to propagation to refocus the ion beam. An accelerating potential between the multipole endcap electrode and the bender entrance lens limits the dispersion of the ion beam. The stack of decelerating lenses at the exit of the first bender plays an important role in compensating the dispersion of the ion trajectories by reshaping the ion beam at the entrance of the octopole ion guide. The latter tolerates a wider dispersion of the incoming beam relative to the quadrupole. The voltages of the octopole exit lens and second bender should be appropriately tuned for optimum transmission, since they are critical for the passage of ions through the second deflector, which directs the ion beam without any intermediate focusing lens towards the entrance of the final quadrupole. Since we do not expect extensive fragmentation of the molecules in our IR studies of solvated amino acids, except for the loss of a water molecule, the resolving power of the second quadrupole may be sacrificed for enhanced ion transmission (cf. *§ 1.1.3.2.3*).

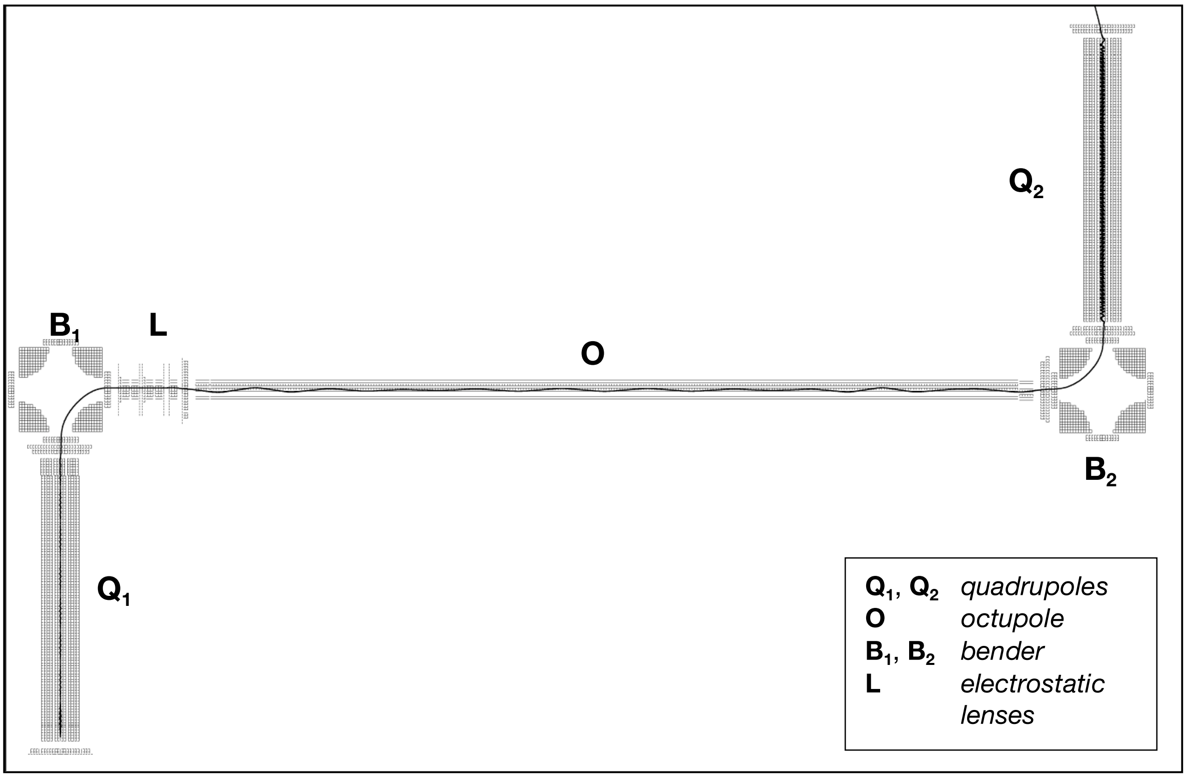

Fig. 1.11: Ion trajectory simulation for TrpH+ (mass 205 amu,, 5 eV kinetic energy).

SIMION simulations also demonstrate that the deflector poles give rise to fringe field effects, that destabilize ion trajectories emerging from the bender. The deflector exit lens voltage appears to largely influence the exiting ion trajectories, and adjustment of this voltage independently from the potential of the bender poles is critical to restore trajectories along the optical axis of the ion optics following the bender.

It appears from the simulations that various sets of voltages applied on the electrodes can transmit ions through the spectrometer modeled in SIMION, so optimization of the voltages is necessary in the real experiment to obtain ion signal on the final detector, although the tuning procedure is greatly facilitated by the intuition developed using the simulations. We also verify that the set of voltages resulting from tuning of the real instrument, when put into SIMION, gives ion trajectories showing a good transmission along the ion optics modeled.

1.3.2 Obtaining mass spectra

Before performing spectroscopic experiments, our primary concern is to obtain mass spectra and fully characterize the performance of the home-built electrospray ion guide tandem mass spectrometer to verify whether the species of interest can be experimentally generated and transmitted efficiently through the instrument in high enough yield for spectroscopic studies.

1.3.2.1 Tuning the ion optics voltages for optimum ion transmission

Optimization of the instrument voltages was accomplished using the ion signal of arginine in the mass spectrum. For this purpose, a solution of arginine (100 μM, in Methanol/Water 1:1 with 0.1 % acetic acid) is electrosprayed under regular conditions to produce fully desolvated ions (cf. *§ 1.1.1.2*) of protonated arginine,

During this tuning procedure, we do not apply any trapping potential to the hexapole, but we use it as a simple ion guide to obtain a continuous ion signal; the first quadrupole acts as a mass filter, while the octopole and the final quadrupole both operate as ion guides. Since a large number of voltages controls the ion transmission through the spectrometer, we first optimize the elements up to the first bender by turning the ion beam towards the first detector (simply by reversing the voltages on the bender pairs of poles, cf. *§ 1.1.3.3*). These potentials are then readjusted and the remaining ion optics are tuned to optimize the transmission to the final detector. With these conditions, we monitor a total ion current to the final detector of ~ 2 pA for protonated arginine, which corresponds to ~ 12.5 10^6 counts/s at the final detector. This is measured with the first quadrupole operating in a mass resolving mode and the final quadrupole acting as an ion guide. Operation of the final quadrupole as a mass filter yields an important loss in ion signal (~ factor of 3), which is consistent with the conclusions drawn from SIMION ion trajectory simulations (cf. *§ 1.3.1.4*). Despite the losses, such ion currents are enough to perform spectroscopic experiments.

Note that the ion current reported above is only indicative of what can be achieved in our spectrometer, since the ion currents detected depend, among other things, on the nature of the species electrosprayed (cf. *§1.1.1.4*). Therefore, an amino acid less basic than arginine such as tryptophan, yields lower ion currents (2.10^6 counts/s) due to its lower ionization efficiency, whereas a protein such as cytochrome C, which gives rise to a distribution of multiply charged ions in electrospray ionization, results in a partition of the total ion current over the different charge states observed (~ 6.10^5 counts/s is measured for the $[M+10H]^{10+}$ charge state).

1.3.2.2 Mass spectra

We investigated the capability of our instrument to produce low-mass ions such as amino acids, but also higher molecular weight compounds such as proteins. The latter were ionized both from denaturing (1:1 water/methanol, 0.1% acetic acid) and native (pure water, no acetic acid) solution conditions. Moreover, water clusters of amino acids were generated and detected with the spectrometer, demonstrating the ability to preserve non-covalently bound complexes in the instrument.

Below are presented mass spectra obtained for tryptophan ($M = 204$ g.mol^{-1}) and horse cytochrome C ($M = 12360$ g.mol^{-1}) (cf. *Fig. 1.12*) using a 100 μM solution for the former in 1:1 water/methanol and 0.1 % acetic acid, and a 10 μM solution of the latter in the same mixture of solvents. The electrospray source is operated under the conditions discussed in *§1.1.1.2*.

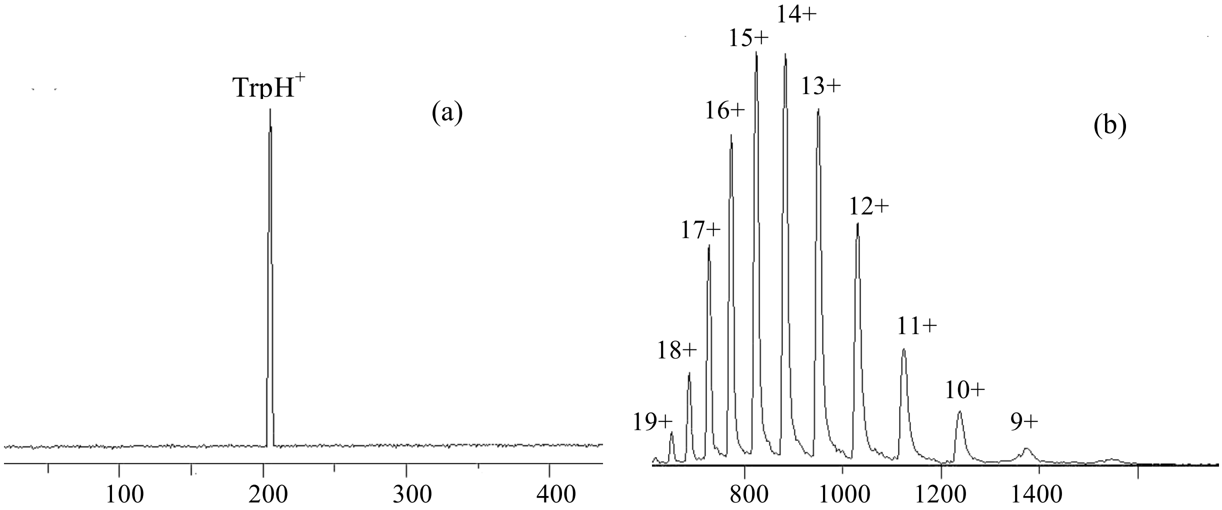

Fig. 1.12: Electrospray mass spectra of (a) tryptophan and (b) horse Cytochrome C.

The spectrum of *Fig. 1.12 (a).* shows a single peak corresponding to protonated tryptophan ($m/z = 205$) with no lower mass fragment ions. Noticeably absent are also higher mass peaks, suggesting that no multimers or clusters of the parent ion with water or methanol molecules form.

In contrast to that of tryptophan, the mass spectrum of cytochrome C (*Fig. 1.12 (b)*) shows a distribution of charge states indicating that the protein exists in various forms accommodating a different number of protonated sites. A comparison with the mass spectrum of cytochrome C obtained from a 10 μM solution in pure water (*Fig. 1.13*) clearly reveals a shift of the distribution towards lower charge states (higher m/z ratios), probably resulting from the fact that the folded protein has less basic sites exposed for protonation.

Fig. 1.13: Mass spectrum of Cyctochrome C electrosprayed from pure water.

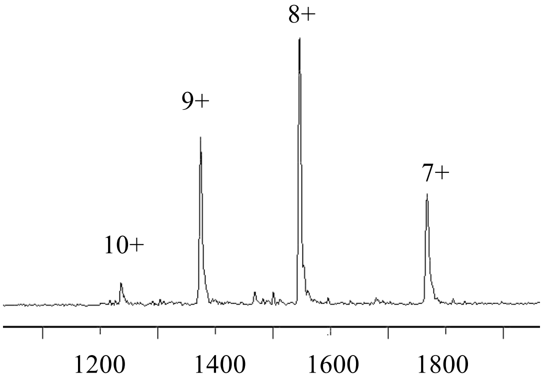

The home built spectrometer therefore offers the ability to generate proteins in folded and unfolded conformations, and allows us to perform conformation specific spectroscopic studies if we wish so.

As opposed to the data reported so far, formation of water clusters necessitates not only different solution conditions, but also different electrospray parameters as discussed in *§1.1.1.2*. The mass spectrum in *Fig. 1.14* shows a distribution of valine water clusters obtained with a nanospray ionization source, with a 1 mM solution of valine in pure water, and using a reduced flow of unheated nitrogen gas in order to form to water clusters from incomplete desolvation of electrospray droplets. Furthermore, gentle acceleration potentials have been used in the electrospray interface to prevent collision induced dissociation of the weakly bound water clusters. A distribution of water clusters of protonated valine containing up to 20 water molecules can be successfully formed and preserved through the spectrometer, demonstrating the possibility to perform microsolvation spectroscopic studies.

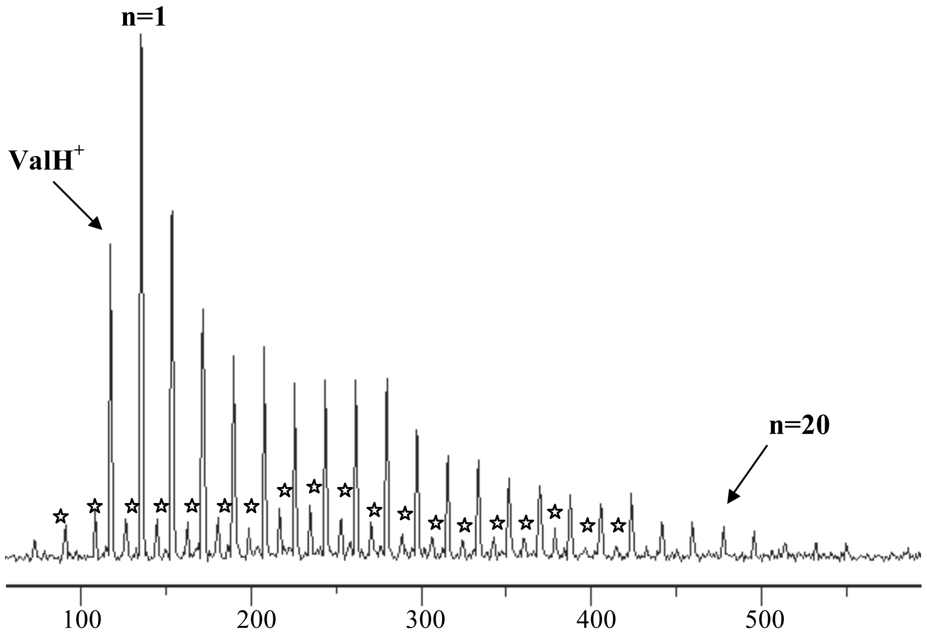

Fig. 1.14: Mass spectrum of protonated valine water clusters. The stars depict pure water clusters peaks $(H_2O)_nH_3O+$.

1.3.2.3 Trapping in the hexapole

As discussed in *§ 1.1.3.1.2* we use the rf-only hexapole as an external reservoir to accumulate ions prior to mass selection and laser irradiation, thereby transforming the continuous electrospray ionization source into a pulsed source which better matches the duty cycle of our lasers.

Ions are accumulated and confined in the rf-only hexapole by pulsing high the exit electrode during some period of time. We have performed a series of experiments to characterize the ion packet released from the hexapole ion trap in terms of number of ions, flight time and width of the ion pulse through the instrument. These characterizations are important for synchronizing the laser irradiation of the ion pulse (cf *Chapter 2*). For these experiments we used a 100 µM solution of Trp in methanol/water with 0.1 % acetic acid, electrosprayed at a flow rate of 1.2 µL/min, with a trapping potential barrier of 14 V.

1.3.2.3.1 Ion currents in the pulsed experiment

By monitoring on the final detector the ion signal mass selected in both stages of the tandem mass spectrometer, as a function of accumulation time in the hexapole, we obtain the following result:

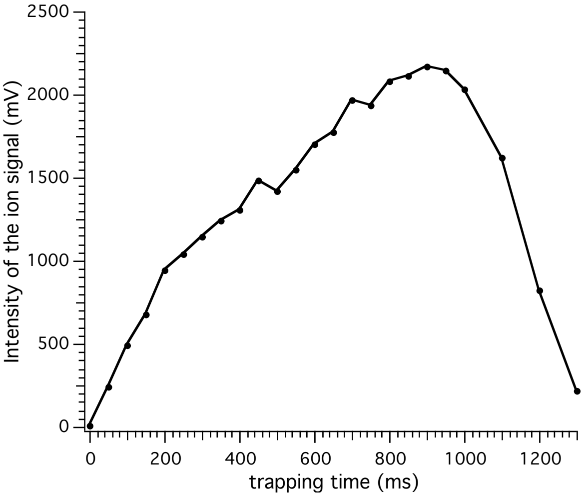

Fig. 1.15: TrpH$^+$ 100 µM solution of Trp in methanol/water, 0.1% acetic acid electrosprayed at a flow rate of 1.2 µL/min, with a trapping potential barrier of 14 V

Figure 1.15 shows an increase in ion signal with accumulation time, reaching a maximum after which the signal decays. At the maximum of the curve we measure a gain of ion signal up to three orders of magnitude higher than that observed in continuous operation of the electrospray source. The hexapole can confine only a limited number of ions before space charge effects take place, leading to fragmentation of the stored ions. Hofstadler *et al.* [67, 68] reported similar results and performed extensive studies to understand and control this phenomenon for multipole storage assisted dissociation applications (see also *§ 1.1.3.1.2*).

The increase of ion signal resulting from accumulating ions in the hexapole implies a higher ion density in the octopole ion guide for laser irradiation. For instance, a pulsed laser experiment at 20 Hz repetition rate limits trapping times in the hexapole to 50 ms, which represents for protonated tryptophan molecular ions a gain in ion signal of about two orders of magnitude. Space charge effects are negligible for these trapping times (*Fig. 1.16*).

It is important to note that the position and height of the maximum in the curve displaying ion signal as a function of accumulation time, depends on the nature of the species confined in the hexapole, namely the ionization efficiency and the number of charges carried by the ion [67]. Moreover weakly bound water clusters produced for hydration studies dissociate more easily during storage in the ion trap due to collisions in the moderate pressure region of the hexapole. Thus, performing spectroscopy on trapped ions requires a compromise between the storage time necessary to obtain the maximum gain in ion signal without dissociation of the ions in the hexapole, and the trapping time allowed by the spectroscopic experiment, which is mainly governed by the repetition rate of the lasers. This should be adapted depending on the nature of the species under investigation.

1.3.2.3.2 Flight time and width of the ion packet

The TrpH$^+$ containing ion packet released from the hexapole exhibits a full width at half maximum (FWHF) of ~ 600 μs and a flight time of ~ 800 μs to the final detector. Using a series of synchronized pulses on the hexapole endcap electrode and the octopole entrance and exit electrodes, we determine the ion time of flight through the octopole ion guide. Briefly the delay between the hexapole dumping pulse and the pulse raising the voltage of the octopole entrance lens, is varied so that the flight time from the hexapole to the entrance of the octopole is determined. In a subsequent step, this delay is set to transmit a slice of the ion packet through the octopole, while a third pulse is applied to the octopole endcap electrode to block the transmission of the ions. By varying the delay between the octopole entrance lens and exit lens pulses, we determine the flight time of the ions through the octopole. Comparison of this flight time with the 600 μs width of the ion packet shows that the latter overfills the octopole ion guide when released from the trap. Moreover, the ion time of flight through the octopole allows us to translate the ion signal levels of

Fig. 1.15 in terms of number of ions in the octopole as a function of trapping time shown in *Fig. 1.16*, for the range of trapping times allowed in a 20 Hz laser experiment. This figure shows that ~ 10 000 ions can be irradiated in the octopole ion guide, thus implying that we have the ability to generate acceptable signal levels in order to obtain spectroscopic information.

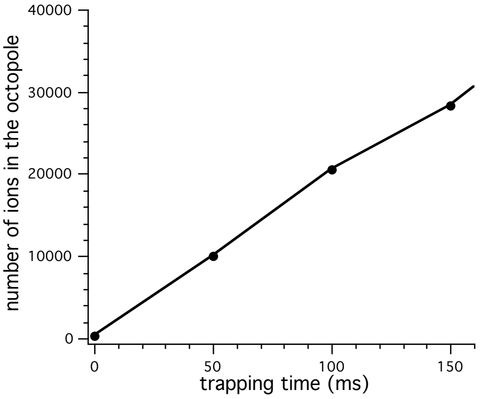

Fig. 1.16: Ion signal enhancement in a 20 Hz laser experiment arising from trapping in the hexapole

Table 1.1 summarizes the flight times measured for TrpH$^+$, along the different stages of the instrument, which are important parameters for a successful implementation of the spectroscopic experiment. The ion time of flight from the output of the hexapole to the entrance of the octopole determines the synchronization between the laser irradiation and the arrival of the ions in the octopole, so that a maximum overlap between the ion packet and the laser pulse is obtained. On the other hand, the flight time to the detector determines the timescale allowed for dissociation of the excited ions in our instrument. It follows that laser activated ions should dissociate within a few hundreds of microseconds for us to be able to measure a photofragment signal as a function of wavelength.

	Time of flight (μs)
Hex_{exit}-$Oct_{entrance}$	200
$Oct_{entrance}$-O_{exit}	250
Hex_{exit}-Detector	800

Table 1.1: Flight time of $TrpH^+$ ions through the instrument.

1.4 CONCLUSIONS

The characterization of the home-built electrospray ionization guide mass tandem spectrometer aids in determining the conditions required to obtain an optical spectrum of the parent ion by monitoring the appearance of fragments. The versatility of our apparatus suggests a variety of spectroscopic applications, however we have focused our interest on hydration studies of amino acids, motivated by the issue of possible zwitterion formation upon microsolvation of amino acids isolated in the gas phase.

References

1. Burns, T. D., Spence, T. G., Mooney, M. A., and Posey, L. A., Chem. Phys. Lett. (1996), 258, 669-679.
2. Chillier, X. F. D., Monnier, A., Bill, H., Gulacar, F. O., Buchs, A., McLuckey, S. A., and VanBerkel, G. J., Rapid Commun. Mass Spectrom. (1996), 10, 299-304.
3. Wang, L. S., Ding, C. F., Wang, X. B., Nicholas, J. B., and Nicholas, B., Phys. Rev. Lett. (1998), 81, 2667-2670.
4. Thompson, C. J., Husband, J., Aguirre, F., and Metz, R. B., J. Phys. Chem. A (2000), 104, 8155-8159.
5. Ideue, S., Sakamoto, K., Honma, K., and Clemmer, D. E., Chem. Phys. Lett. (2001), 337, 79-84.
6. Rodriguez-Cruz, S. E., Khoury, J. T., and Parks, J. H., J. Am. Soc. Mass Spectrom. (2001), 12, 716-725.
7. Khoury, J. T., Rodriguez-Cruz, S. E., and Parks, J. H., J. Am. Soc. Mass Spectrom. (2002), 13, 696-708.
8. Danell, A. S. and Parks, J. H., Int. J. Mass Spectrom. (2003), 229, 35-45.

9. Boye, S. V., Nielsen, I. B., Nielsen, S. B., Krogh, H., Lapierre, A., Pedersen, H. B., Pedersen, S. U., Pedersen, U. V., and Andersen, L. H., J. Chem. Phys. (2003), 119, 338-345.
10. Nonose, S., Iwaoka, S., Tanaka, H., Okai, N., Shibakusa, T., and Fuke, K., Eur. Phys. J. D (2003), 24, 335-338.
11. Nonose, S., Iwaoka, S., Mori, K., Shibata, Y., and Fuke, K., Eur. Phys. J. D (2005), 34, 315-319.
12. Nolting, D., Marian, C., and Weinkauf, R., Phys. Chem. Chem. Phys. (2004), 6, 2633-2640.
13. Kang, H., Dedonder-Lardeux, C., Jouvet, C., Martrenchard, S., Gregoire, G., Desfrancois, C., Schermann, J. P., Barat, M., and Fayeton, J. A., Phys. Chem. Chem. Phys. (2004), 6, 2628-2632.
14. Kang, H., Jouvet, C., Dedonder-Lardeux, C., Martrenchard, S., Gregoire, G., Desfrancois, C., Schermann, J. P., Barat, M., and Fayeton, J. A., Phys. Chem. Chem. Phys. (2005), 7, 394-398.
15. Yang, X., Wang, X. B., Vorpagel, E. R., and Wang, L. S., Proc. Natl. Acad. Sci. U. S. A. (2004), 101, 17588-17592.
16. Oh, H. B., Lin, C., Hwang, H. Y., Zhai, H. L., Breuker, K., Zabrouskov, V., Carpenter, B. K., and McLafferty, F. W., J. Am. Chem. Soc. (2005), 127, 4076-4083.
17. Talbot, F. O., Tabarin, T., Antoine, R., Broyer, M., and Dugourd, P., J. Chem. Phys. (2005), 122, -.
18. Felici, N. J., Direct Current (1959), 4, 3-12.
19. Zeleny, J., Phys. Rev. (1917), 10, 1-6.
20. Yamashita, M. and Fenn, J. B., J. Phys. Chem. (1984), 88, 4451-4459.
21. Dole, M., Mack, L. L., and Hines, R. L., J. Chem. Phys. (1968), 49, 2240-&.
22. Taylor, G., Proc R Soc Lon Ser-A (1964), 280, 383-&.
23. Iribarne, J. V. and Thomson, B. a., J. Chem. Phys. (1976), 64, 2287-2294.
24. Smith, J. N., Flagan, R. C., and Beauchamp, J. L., J. Phys. Chem. A (2002), 106, 9957-9967.
25. Felitsyn, N., Peschke, M., and Kebarle, P., Int. J. Mass Spectrom. (2002), 219, 39-62.
26. Fenn, J. B., Mann, M., Meng, C. K., Wong, S. F., and Whitehouse, C. M., Mass Spectrom. Rev. (1990), 9, 37-70.
27. Schnier, P. D., Gross, D. S., and Williams, E. R., J. Am. Chem. Soc. (1995), 117, 6747-6757.
28. Schnier, P. D., Gross, D. S., and Williams, E. R., J. Am. Soc. Mass Spectrom. (1995), 6, 1086-1097.
29. Iavarone, A. T. and Williams, E. R., Int. J. Mass Spectrom. (2002), 219, 63-72.
30. Williams, E. R., J. Mass Spectrom. (1996), 31, 831-842.
31. Chowdhury, S. K., Katta, V., and Chait, B. T., Rapid Commun. Mass Spectrom. (1990), 4, 81-87.
32. Smith, R. D. and Lightwahl, K. J., Biol. Mass Spectrom. (1993), 22, 493-501.
33. Rodriguez-Cruz, S. E., Klassen, J. S., and Williams, E. R., J. Am. Soc. Mass Spectrom. (1997), 8, 565-568.
34. Lee, S. W., Freivogel, P., Schindler, T., and Beauchamp, J. L., J. Am. Chem. Soc. (1998), 120, 11758-11765.
35. Spence, T. G., Burns, T. D., Guckenberger, G. B., and Posey, L. A., J. Phys. Chem. A (1997), 101, 1081-1092.
36. Zhan, D., Rosell, J., and Fenn, J. B., J. Am. Soc. Mass Spectrom. (1998), 9, 1241-1247.
37. Zhan, D. and Fenn, J. B., Int. J. Mass Spectrom. (2002), 219, 1-10.
38. Nonose, S., Tanaka, H., Okai, N., Shibakusa, T., and Fuke, K., Eur. Phys. J. D (2002), 20, 619-626.
39. Sei, Y., Shimotakahara, S., Ishii, J., Shindo, H., Seki, H., Yamaguchi, K., and Tashiro, M., Analytical Sciences (2005), 21, 449-451.
40. Klassen, J. S., Blades, A. T., and Kebarle, P., J. Phys. Chem. (1995), 99, 15509-15517.
41. Rodriguez-Cruz, S. E., Klassen, J. S., and Williams, E. R., J. Am. Soc. Mass Spectrom. (1999), 10, 958-968.
42. Smith, D. P. H., Ieee T Ind Appl (1986), 22, 527-535.

43. Wilm, M. S. and Mann, M., Int. J. Mass Spectrom. Ion Process. (1994), 136, 167-180.
44. Wilm, M. and Mann, M., Anal. Chem. (1996), 68, 1-8.
45. Drahos, L., Heeren, R. M. A., Collette, C., De Pauw, E., and Vekey, K., J. Mass Spectrom. (1999), 34, 1373-1379.
46. Bustamente, S. W., Okumura, M., Gerlich, D., Kwok, H. S., Carlson, L. R., and Lee, Y. T., J. Chem. Phys. (1987), 86, 508-515.
47. Weinheimer, C. J. and Lisy, J. M., Int. J. Mass Spectrom. Ion Process. (1996), 159, 197-208.
48. Wang, L. S., Ding, C. F., Wang, X. B., and Barlow, S. E., Rev. Sci. Instrum. (1999), 70, 1957-1966.
49. Puskar, L. and Stace, A. J., J. Chem. Phys. (2001), 114, 6499-6501.
50. Teloy, E. and Gerlich, D., Chem. Phys. (1974), 4, 417.
51. Gerlich, D., J Chem Soc Faraday T (1993), 89, 2199-2208.
52. Muntean, F. and Armentrout, P. B., J. Chem. Phys. (2001), 115, 1213-1228.
53. Armentrout, P. B., Int. J. Mass Spectrom. (2000), 200, 219-241.
54. Armentrout, P. B., J. Am. Soc. Mass Spectrom. (2002), 13, 419-434.
55. Okumura, M., Yeh, L. I., Normand, D., Vandenbiesen, J. J. H., Bustamente, S. W., Lee, Y. T., Lee, T. J., Handy, N. C., and Schaefer, H. F., J. Chem. Phys. (1987), 86, 3807-3815.
56. Boo, D. W. and Lee, Y. T., Int. J. Mass Spectrom. Ion Process. (1996), 159, 209-229.
57. Price, J. M., Crofton, M. W., and Lee, Y. T., J. Phys. Chem. (1991), 95, 2182-2195.
58. Wang, Y. S., Chang, H. C., Jiang, J. C., Lin, S. H., Lee, Y. T., and Chang, H. C., J. Am. Chem. Soc. (1998), 120, 8777-8788.
59. Jiang, J. C., Wang, Y. S., Chang, H. C., Lin, S. H., Lee, Y. T., Niedner-Schatteburg, G., and Chang, H. C., J. Am. Chem. Soc. (2000), 122, 1398-1410.
60. Spence, T. G., Trotter, B. T., and Posey, L. A., J. Phys. Chem. A (1998), 102, 7779-7786.
61. Gerlich, D., Adv Chem Phys (1992), 82, 1-176.
62. Marto, J. A., Marshall, A. G., May, M. A., and Limbach, P. A., J. Am. Soc. Mass Spectrom. (1995), 6, 936-946.
63. Huang, Y. L., Guan, S. H., Kim, H. S., and Marshall, a. G., Int. J. Mass Spectrom. Ion Process. (1996), 152, 121-133.
64. Wang, Y., Shi, S. D. H., Hendrickson, C. L., and Marshall, A. G., Int. J. Mass Spectrom. (2000), 198, 113-120.
65. Freitas, M. A. and Marshall, A. G., Int. J. Mass Spectrom. (1999), 183, 221-231.
66. Hofstadler, S. A., Sannes-Lowery, K. A., and Griffey, R. H., Rapid Commun. Mass Spectrom. (1999), 13, 1971-1979.
67. Sannes-Lowery, K. A. and Hofstadler, S. A., J. Am. Soc. Mass Spectrom. (2000), 11, 1-9.
68. SannesLowery, K., Griffey, R. H., Kruppa, G. H., Speir, J. P., and Hofstadler, S. A., Rapid Commun Mass Spectrom (1998), 12, 1957-1961.
69. Paul, W. and Steinwedel, H., Z Naturforsch A (1953), 8, 448-450.
70. Dawson, P. H., Mass Spectrometry Reviews (1986), 5, 1-37.
71. Blaum, K., Geppert, C., Muller, P., Nortershauser, W., Otten, E. W., Schmitt, A., Trautmann, N., Wendt, K., and Bushaw, B. A., Int. J. Mass Spectrom. (1998), 181, 67-87.
72. Paul, W., Reinhard, H. P., and Vonzahn, U., Z Phys (1958), 152, 143-182.
73. Fenn, J. B., Dalton Trans. (2003), 42, 3871-3894.
74. Dawson, P. H., Quadrupole Mass Spectometry and its applications. 1976, Amsterdam: Elsevier Scientific Publishing Company.
75. Zeman, H. D., Rev. Sci. Instrum. (1977), 48, 1079-1085.
76. Mahaffy, P. R. and LAI, K., J Vac Sci Technol A (1990), 8, 3244-3246.
77. Huber, B. a., Miller, T. M., Cosby, P. C., Zeman, H. D., Leon, R. L., Moseley, J. T., and Peterson, J. R., Rev. Sci. Instrum. (1977), 48, 1306-1312.
78. Dahl, D. a., Int. J. Mass Spectrom. (2000), 200, 3-25.

Chapter 2

IMPLEMENTING IR PHOTOFRAGMENTATION SPECTROSCOPY OF NON-COVALENT SPECIES IN TANDEM MASS SPECTROMETRY

The experiments described below are performed in the home-built photofragment spectrometer described in *Chapter 1*. The goal of our studies, defined in the *Introduction*, is to gain insight into the structure of amino acids formed by electrospray ionization in a microsolvation environment. As already discussed in the *Introduction*, experimental work on neutral amino acids showed that they are non-zwitterionic in the gas phase, although it is well established that the most stable form is zwitterionic in aqueous solution under near neutral pH conditions. The solvent clearly plays a role in molecular structure but the nature of this role is not completely understood.

Our motivation is to bridge the gap between gas- and solution phase experiments. In the work presented here, we follow by IR laser spectroscopy in the gas phase, the stepwise structural modifications of charged amino acids ($Val{\bullet}Li^+$, $ValH^+$ and $TrpH^+$) upon solvation. To help in structural assignments, we also measure the vibrational spectra of protonated tryptamine hydrates. Tryptamine is a tryptophan analogue, which does not possess the carboxylic group. Since all of the solvent molecules in a bulk solution do not interact with the solute, we take advantage of electrospray ionization and eliminate the solvent medium, leaving a restricted number of solvent molecules around the ion forming the microsolvation shell.

There are three important aspects related to such studies: (1) amino acids are flexible molecules that can adopt many different conformations of comparable energy already in the absence of solvent; (2) hydration of flexible molecules may reduce the number of populated conformers or may even populate new conformations not accessible to the bare molecule [1]; (3) reciprocally, the solute may also influence the organization of the solvation shell. Thus, structure and solvation are intimately related, relying on a delicate balance of non-covalent solute-solute, solute-solvent and solvent-solvent interactions.

By following the hydration process we try to unravel the relative importance of these intramolecular and intermolecular non-covalent interactions in order to identify the preferred binding sites of water and understand how hydration can affect the amino acid conformation. This was done by measuring vibrational spectra in the light atom stretch region between 2900 and 3800 cm^{-1}, looking for spectroscopic signatures of the free and H-bonded OH and NH stretches.

2.1 THE PARTICULARITY OF STUDYING WEAKLY-BOUND COMPLEXES

2.1.1 Experimental conditions

Clusters of analyte molecules inherently form in ESI with the solvent. The parameters influencing the formation of these weakly bound clusters are discussed in *§ 1.1.1.2.* Here, we report only the experimental conditions employed to produce water clusters of lithiated-valine ($Val{\bullet}Li^+$) and protonated - valine ($ValH^+$), - tryptophan ($TrpH^+$) and - tryptamine ($TRAH^+$) from partial desolvation of the droplets formed by nanoelectrospray ionization.

L-valine (Val), L-tryptophan (Trp) and tryptamine (TRA) were purchased from Sigma-Aldrich Co. (Switzerland) and lithium chloride was obtained from AppliChem GmbH (Germany). In the present experiment, solutions containing the analyte are electrosprayed from the nanospray emitter, generally at a distance of 2 – 3 mm from the glass capillary inlet and slightly off axis to limit contamination of the vacuum components by the important amount of neutrals easily entrained in the spectrometer when the emitter is centered on the transfer capillary orifice. By cutting the tip of the commercial nanospray emitters (borosilicate off-line emitters type 'long' from Proxeon Biosystems, Dk) to an appropriate length, we get control over the distributions of water clusters observed in the mass spectra and stability of the ion signal. The latter is also influenced by the solvent mixture, spraying voltage and the drying gas. Adjustment of these parameters depends on the nature of the analyte in solution.

In general, we apply a voltage of 800 – 1000 V on the metallized spray needle tip with respect to the grounded inlet of the transfer capillary in order to initiate the spray. A very low countercurrent flow of N_2 drying gas (heated if necessary) is used to control the formation of partially desolvated ions. A solution of 1 mM of L-Valine and 1 mM of lithium chloride in deionized water is used to form either protonated or lithiated valine water clusters without heating the nitrogen drying gas. A spraying voltage of ~ 1 kV and long nanospray emitter tips favor the formation of protonated valine hydrates whereas the lithiated valine ones are produced using slightly shorter spray needles and a lower voltage (~ 800 V). Water clusters of protonated tryptophan are obtained from a 2.10^{-4} M solution in 1:1 H_2O/MeOH with 0.2 % acetic acid, using a spraying voltage of ~ 1 kV and heating the drying gas to 125 ºC. Even though tryptamine is a tryptophan analog, different conditions are necessary to generate the hydrates of protonated tryptamine. A 2.10^{-4} M solution of TRA in 1:1 H_2O/MeOH with 0.2 % acetic acid is diluted 2 times in pure methanol and sprayed at ~ 800 – 900 V, while the nitrogen gas is heated at 100 ºC.

Besides the conditions reported above, some of the voltages in vacuum are readjusted depending on the nature of the ion core in the water clusters. Thus, the potential difference between the transfer capillary and the skimmer cone in the electrospray vacuum interface is critical for the preservation of non-covalently bound complexes in this region of moderate pressure. It is refined within a ± 10 V range depending on the strength of interactions between the amino acid ion core and the solvent adducts. In conventional operation of the electrospray source, which yields adduct free species, this potential difference controls the acceleration of ions through the residual background gas and helps complete desolvation of the molecular ions (cf. *§ 1.1.1.1*). Another voltage sensitive to the nature of species electrosprayed is the hexapole pole bias, which controls the kinetic energy of the ions produced by the source. Fine-tuning of this voltage may significantly enhance transmission of ions through the photofragment spectrometer. All other voltages of the photofragment spectrometer are not modified, since transmission through the higher vacuum parts of the instrument does not change substantially for species of similar charge and kinetic energy. Typical voltages used to transmit ions through the spectrometer are presented in *Fig 2.1* in the form of a potential energy-diagram.

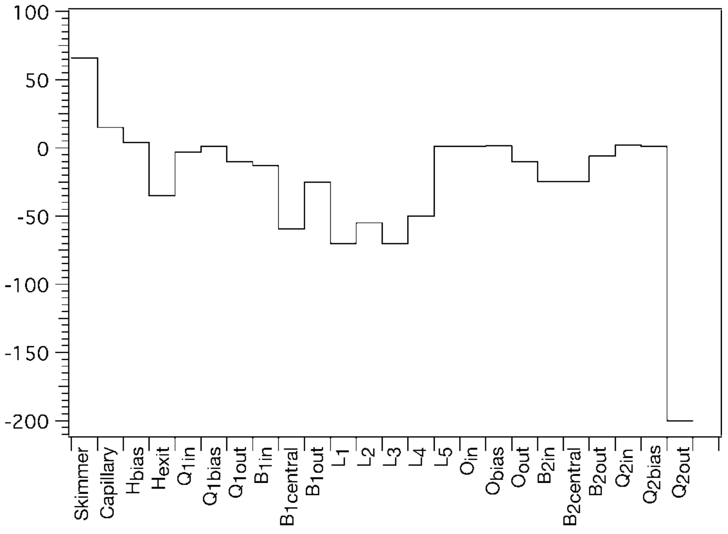

Fig 2.1: Potential energy diagram

We successfully form hydrates of protonated valine with up to ~ 20 water molecules, up to five water adducts for protonated tryptophan, with up to six for protonated tryptamine and up to four in the case of lithiated-valine (cf. *Fig. 2.2 - 2.5*).

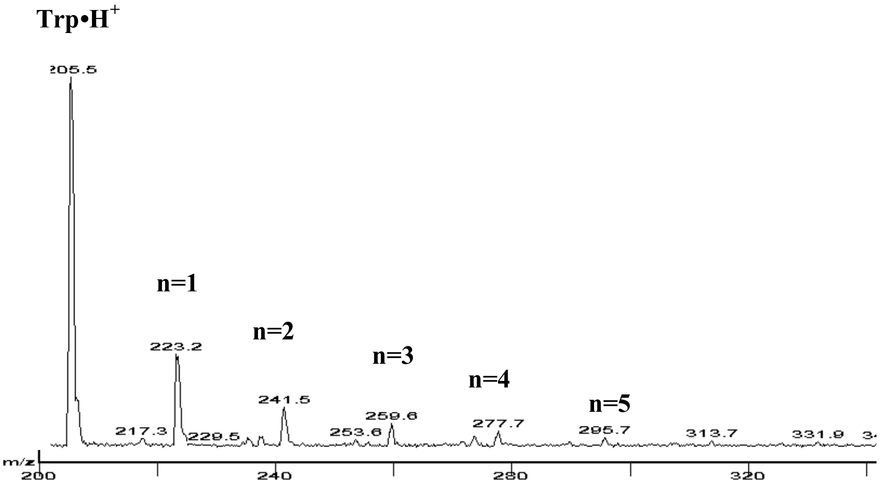

Fig 2.2: Disttribution of water clusters obtained for Trp•H^+(H_2O)$_n$

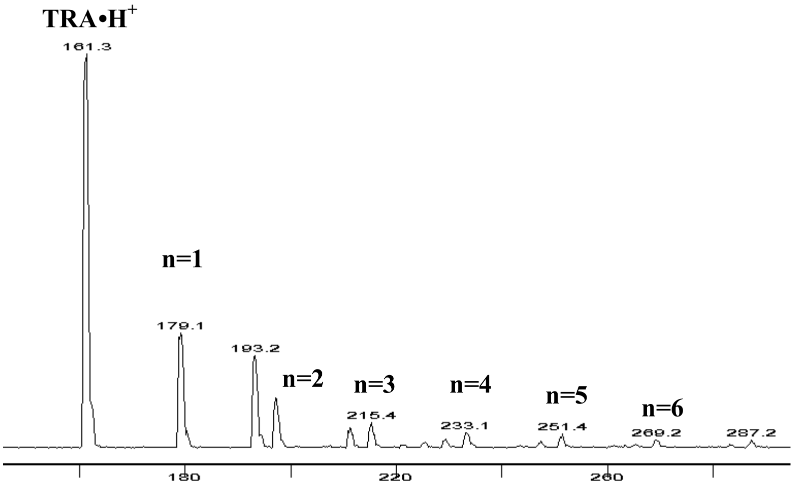

Fig 2.3: Disttribution of water clusters obtained for TRA•H^+(H_2O)$_n$

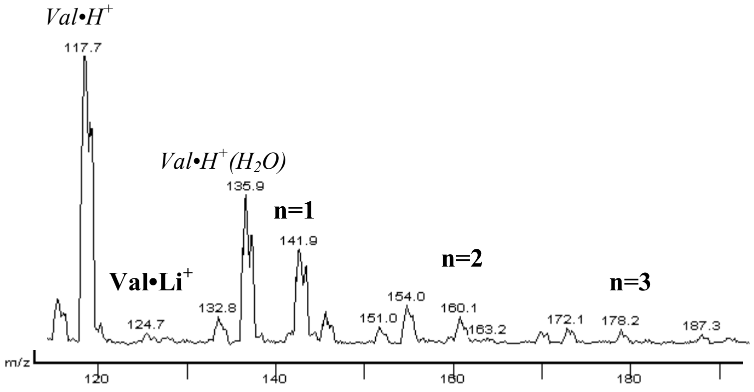

Fig 2.4: Disttribution of water clusters obtained for Val•Li$^+$(H$_2$O)$_n$

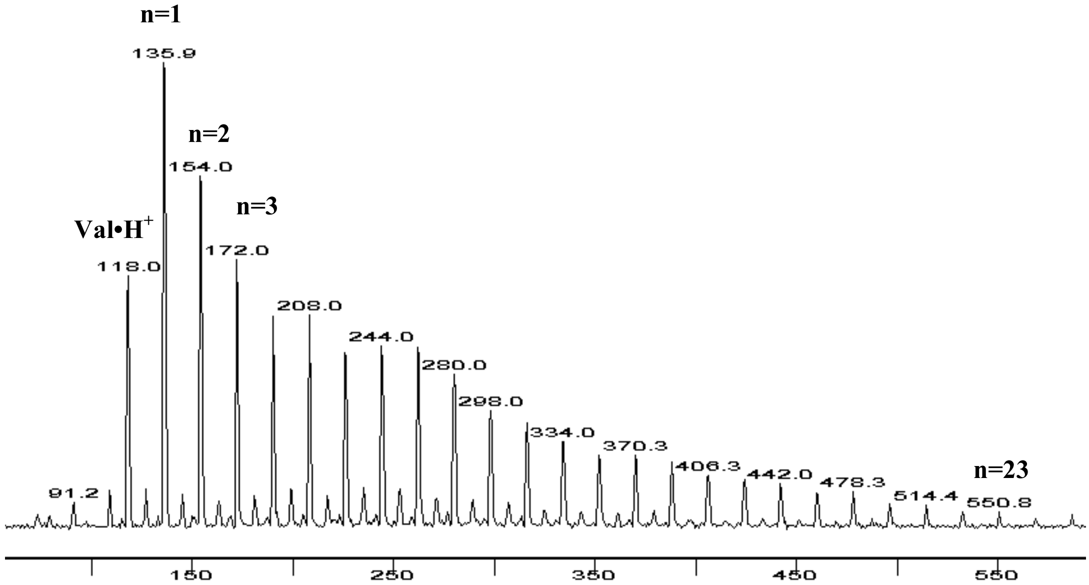

Fig 2.5: Disttribution of water clusters obtained for Val•H$^+$(H$_2$O)$_n$

2.1.2 Nature and strength of non-covalent interactions in the complexes formed

The aforementioned water clusters are held together by non-covalent interactions. The latter are in general substantially weaker in solution than covalent bond forces, as shown in *Table 2.1*. However in the gas phase, electrostatic interactions are substantially reinforced since vacuum is characterized by a dielectric constant of 1 (compare to 80 for water) and in contrast to the water medium it does not play an efficient role in shielding one charge from another.

Type of interaction		Energy in solution (kcal/mol)	Energy in vacuum (kcal/mol)
Covalent		90	90
Non-covalent	Electrostatic	3 - 7	x 80 vs. solution
	Hydrogen bonding	3 - 7	4 - 15
	Van der Waals	1	0 - 2
	Hydrophobic	---	weakened

Table 2.1: Typical energies of interaction for non-covalent forces in solution and in the gas phase.

Hydrogen-bonding is the principal type of interaction between water and TRA•H$^+$, Trp•H$^+$ or Val•H$^+$, due to the presence of many H-bonding sites in each amino acid as shown in *Fig 2.6.* Indeed, each of these molecular ions possesses several neutral functional groups either in the carboxylic acid end or in the residue, which are propitious for H-bonding, while the protonated amino group offers a stronger interaction due to the presence of the charge. It is therefore obvious from *Table 2.1* that the above hydrates are held together by non-covalent bonds (< 15 kcal/mol), which are clearly weaker than covalent ones (~ 90 kcal/mol).

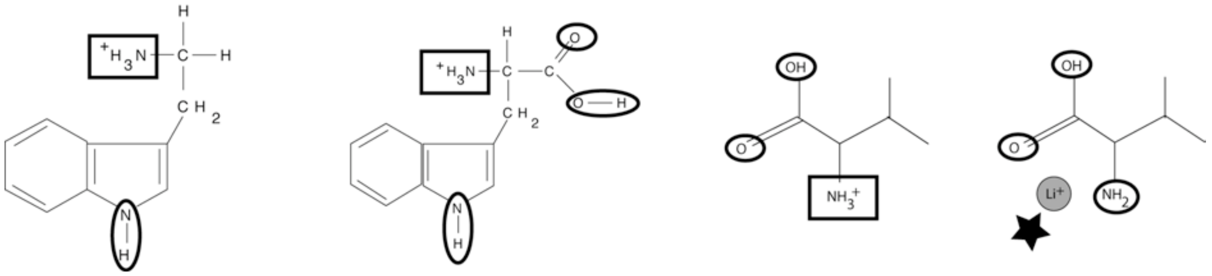

Fig 2.6: Hydrogen-bonding sites (in oval frame), mixed hydrogen-bonding/electrostatic (square frame) and pure electrostatic interaction (★) sites of protonated- tryptoptamine, -tryptophan, -valine, and lithitated valine (from left to right).

On the other hand, Val•Li$^+$ carries its charge by binding to the lithium cation. The latter provides an additional type of electrostatic interaction with the water dipole even stronger than hydrogen bonding: the binding energies of Val•Li$^+$ $(H_2O)_{n=1-3}$ were determined by Williams and coworkers [2]. They measured a threshold dissociation energy of ~ 20 kcal/mol for the more strongly bound monohydrate of lithiated valine, showing that these complexes are more strongly bound than non-covalently bound edifices.

All of the species produced in the present study are fragile clusters that can break apart more easily than covalently bonded edifices due to the weaker interactions involved between their different constituents. However they are stable enough to allow for their investigation in the photofragment spectrometer. Although nanoelectrospray appears to be a gentle enough ionization technique, which permits to generate water clusters of amino acids in the gas phase, our photofragment spectrometer should also provide suitable conditions to preserve the clusters intact and avoid substantial dissociation as they travel through the different stages of the apparatus. Thus, photofragmentation spectroscopic studies are possible in our instrument, if the main contribution to dissociation arises from laser irradiation.

2.2 THE FATE OF WEAKLY BOUND CLUSTERS IN THE PHOTOFRAGMENT SPECTROMETER

This section gives an overview of the different processes that may affect the lifetime of non-covalent complexes in the spectrometer. Since the instrument is described in detail in *Chapter 1*, we only refer here to the features relevant for the discussion.

2.2.1 Collision induced dissociation (CID)

Ions entering in the gas phase experience collisions through the first few pumping regions of the electrospray interface.

As the ions emerge from the transfer capillary they are accelerated by an electrostatic potential of 40 -50 V towards the skimmer but they also experience collisions with the residual gas at the pressure of ~ 1 mbar maintained in this region. The kinetic energy (E_0) acquired by the ions can be high enough for energetic collisions to occur with the room temperature gas (G). It is possible to estimate an upper limit for the translational energy loss ($\Delta E_{kin,inelastic}$) [3] and the maximum kinetic energy converted into internal energy ($\Delta E_{\text{int},inelastic}$) [4] assuming a ‘head-on’ completely inelastic collision:

$$\Delta E_{kin,inelastic} = -E_{C.M}\frac{2m_P + m_G}{m_P + m_G} \qquad \text{Eq. 2.1}$$

$$\Delta E_{\mathrm{int},inelastic} = E_{C.M} = E_0\frac{m_G}{m_G + m_P} \qquad \text{Eq. 2.2}$$

where $E_{C.M}$ is the kinetic energy in the reference framework moving with the center of mass of the collision partners *G* (gas) and *P* (projectile or ions) [4]. *Equation 2.2* gives an absolute maximum of the energy converted. It is important to note that the energy transferred in the real collisions is much lower not only because of the efficiency drop due to the impact parameter but also because the collision does not involve the entire projectile [4]. Partially inelastic collisions occur in reality so that the amount of translational energy converted into internal energy is smaller than $E_{C.M}$ and depends on the degree of inelasticity (η) of a collision, which is itself a function of $E_{C.M}$. For partially inelastic collisions:

$$\Delta E_{\mathrm{int}} = \eta E_{C.M} \qquad \text{Eq. 2.3}$$

Assuming a 50 V acceleration potential applied on the singly charged ion of Val•Li$^+$ (H_2O) (M = 142 g/mol) colliding with air molecules (M = 30 g/mol) between the transfer capillary and the skimmer cone, we evaluate the kinetic energy loss in one collision $\Delta E_{\mathrm{kin},inelastic} \approx 16$ eV and $\Delta E_{\mathrm{int},inelastic} \approx 9$ eV. This energy is largely higher than the binding energy of water in the monohydrate of lithiated valine (0.90 eV) [2], although it is clearly overestimated as mentioned above. Assuming $\eta = 0.1\Delta E_{\mathrm{int}}$ for a partially elastic collision, the amount of energy transferred is still on the order of the dissociation energy of the most strongly non-covalently bound clusters studied here. This shows that collision induced dissociation may occur in the first pumping region of the vacuum system, especially for clusters with lower binding energies than that of lithiated valine monohydrate.

CID can easily be controlled by the acceleration potentials applied on the ions in this region (cf. *§ 1.1.1.1*). Since we typically employ 40 – 50 V of acceleration for obtaining a good ion signal of the clusters investigated, it is probable that the hydrates of small sizes observed in our mass spectra are formed from fragmentation of higher order clusters in the electrospray interface region.

2.2.2 Collisional focusing and cooling

The rf-only hexapole traverses two differential pumping stages maintained at the pressures of 2.10^{-3} and 5.10^{-5} mbar respectively (cf. *§ 1.2.2*). Collisions occur between the background gas and singly charged ions entering the hexapole. The ion injection energy is determined by the voltage difference between the skimmer and the pole bias of the multipole (~ 10 eV). It has been shown [5-7] that in rf-only multipoles, ions with energies of a few electron-volts give rise to low energy and substantially inelastic collisions so that collisional focusing and cooling is observed. Since, ions lose radial and axial kinetic energy by collisions in the hexapole, their translational energy is assumed to be close to the multipole pole bias (~ 4 eV) with some energy spread of a few electron volts. Collisions experienced in the hexapole should lead to thermalization of the energy of the ion beam [8] with the bath gas at room temperature. This should occur if ions find themselves at the bottom of the effective potential well and do not undergo large accelerations in the RF field near the poles.

2.2.3 Multipole storage assisted dissociation

As explained in *§ 1.3.2.3*, long accumulation times in the hexapole can result in fragmentation of the trapped ions. Thus, for non-covalent complexes, the onset of dissociation appears at shorter trapping times due to the lower binding energies involved in these weakly bound species. We therefore choose the accumulation time for each cluster investigated such as to avoid any loss of the ion signal.

2.2.4 Unimolecular dissociation observed in the absence of laser light

In the subsequent stages of the spectrometer, the high vacuum conditions maintained from the first quadrupole up to the final detector involve pressures below 10^{-7} mbar. Assuming a hard-sphere collision between the molecular ions and air, and the cross-section on the order of ~ 50 – 100 $Å^{-2}$ [9], we estimate the mean free path at such a pressure to be higher than 20 m for the larger clusters produced, which is beyond the dimensions of our instrument and implies a collision free environment. It is important to maintain the clusters intact after mass selection of the parent ion beam to insure that the major contribution to the fragmentation ion signal comes from photodissociation by laser irradiation.

Although collisional activation of the non-covalent complexes of amino acids is unlikely to occur after the first quadrupole, the mass spectra recorded in the absence of laser light in the final quadrupole show evidence for the loss of one water molecule from a mass selected precursor complex. In both protonated ($X=H^+$) and lithiated ($X=Li^+$) amino acid (AA) water clusters, we observe the following unimolecular dissociation reaction, which is independent of the degree of hydration:

$$AA \bullet X^+(H_2O)_n \rightarrow AA \bullet X^+(H_2O)_{n-1} + H_2O$$

We show in *Fig 2.7* a typical fragmentation mass spectrum obtained in the absence of laser light, when performing mass analysis in the last quadrupole of the mass selected parent ion beam. The loss of water in the absence of laser irradiation presumably arises from thermally induced unimolecular dissociation indicating that clusters have an excess of internal vibrational energy.

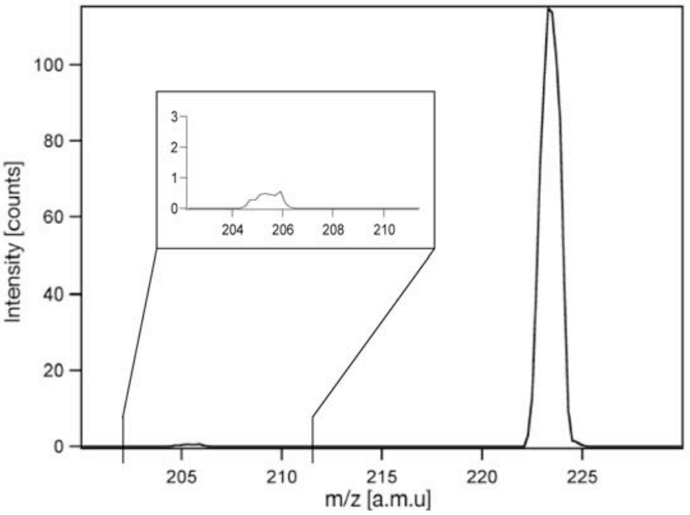

Fig 2.7: Mass spectrum of Trp•H$^+$(H$_2$O) illustrating thermally induced dissociation.

2.2.4.1 Unimolecular dissociation rates

For each degree of hydration of Val•Li$^+$ (H$_2$O)$_{n=1\text{-}4}$ and Trp•H$^+$ (H$_2$O)$_{n=1\text{-}4}$, we calculate the fraction of molecules dissociated I_f/I_0 from the mass spectra measured. We use this value to estimate an average unimolecular dissociation rate <*k*> of the parent cluster according to the following equation:

$$\langle k \rangle = -\frac{1}{t}\ln\left(1-\frac{I_f}{I_0}\right) \qquad \textit{Eq. 2.4}$$

where I_f is the intensity of the fragment ion measured on the dissociation channel mass, I_0 represents the sum of intensities of the fragment and parent ions and t is time-of-flight from the first quadrupole to the final one. In this calculation we assume that dissociation occurs within the timeframe determined by t. Moreover, the use of *Eq. 2.4* implies that we assume equal detection efficiency for the parent clusters and the fragments, which is unlikely to occur since they have different kinetic energies and their transmission through the different ions optics of our instrument can be therefore affected. We have experimental evidence that the detection efficiency of the fragments in the final stage of the spectrometer is less than that of the parent ions, however it is difficult to quantify it.

The average rates calculated (from *Eq. 2.4*) for each hydrate of lithiated valine and protonated tryptophan are shown in *Fig 2.8*. This figure shows in the case of Trp•H$^+$ $(H_2O)_n$ that higher order clusters are more weakly bound than the lower ones. It follows that weaker interactions seem to be involved in these hydrates as the number of water molecules increases. The same trend is observed for the hydrates of lithiated valine containing up to three water molecules. This is consistent with the threshold dissociation energies reported by Williams and coworkers [2] for Val•Li$^+$ $(H_2O)_{1-3}$, ranging from 0.9 eV for the cluster of the monohydrate to 0.61 eV and 0.5 eV for the dihydrate and the trihydrate respectively.

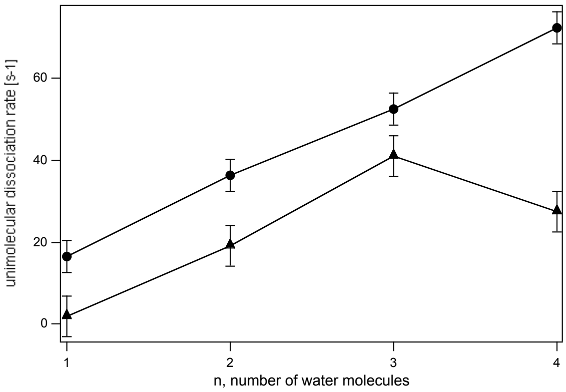

Fig 2.8: Unimolecular dissociation rates for the loss of one water molecule for: Trp•H$^+$ $(H_2O)_n$ (●) and Val•Li$^+$ $(H_2O)_n$ (▲).

A noticeable change in the variation of the dissociation rates of Val•Li$^+$ $(H_2O)_n$, measured in our instrument, appears between n=3 and n=4. This might reflect a structural modification of the hydrate upon addition of the fourth water molecule. These observations provide some preliminary information about the structures investigated and should be confirmed by the spectroscopic results.

2.2.4.2 Characterization of the temperature of the clusters formed in the nanoES source

Based on the above unimolecular dissociation rates extracted from the mass spectra in the absence of laser excitation, we use the statistical model of Rice-Ramsperger-Kassel-Marcus (RRKM) [10] to get a crude estimate of the temperature of clusters released from the hexapole. A fundamental assumption of this theory is that energy flows statistically among all oscillators so that a microcanonical ensemble is maintained. This implies that any arrangement of the internal energy of the system is equiprobable, and dissociation is determined by the probability of concentrating in one vibrational mode, an energy equal or above the dissociation energy (E_0).

To evaluate the temperature of the clusters, we use the canonical expression of the RRKM rate $k(T)$, assuming a Boltzmann energy distribution for a system at constant temperature T. The expression of *k(T)* results from the averaging of the microcanonical RRKM rate *k(E)* over the distribution of internal energies at *T* and is given by [10]:

$$k(T) = \frac{k_B T Q^{\ddagger}(T)}{hQ(T)} e^{-E_0/k_B T} \qquad \textit{Eq. 2.5}$$

where *Q* and $Q^{\ddagger}$ are respectively the partition function of the system and that of the transition state, E_0 the dissociation energy, *h* is Planck's constant and k_B Boltzmann constant.

The general expression of the partition function is:

$$Q(T) = \prod_i \frac{1}{1 - e^{-\nu_i/k_B T}} \qquad \textit{Eq. 2.6}$$

where ν_i are the vibrational frequencies of the system. In $Q^{\ddagger}(T)$ the ν_i are those of the transition state.

With the above equations, we calculate the dissociation rate *k(T)* of ValLi$^+$• (H_2O) for different temperatures. We use for *Q(T)* the scaled vibrational frequencies obtained from density functional theory (DFT) calculations performed for the lowest energy conformer of this cluster, (cf. *§ 2.4* for details). The frequencies of the transition state for $Q^{\ddagger}(T)$ are assumed to be those of the monohydrate minus the frequency of the mode that dissociates. Finally, E_0 is assumed to be the threshold dissociation energy measured from BIRD experiments (0.9 eV) for this particular hydrate [2]. By comparing the unimolecular dissociation rate *k(T)* at different temperatures, with the dissociation rate ($2 \pm 0.5\ s^{-1}$) deduced from the experimental mass spectrum, a temperature of 370 ± 20 K is estimated. This calculation takes into account the uncertainty on the binding energy together with that on the dissociation rates estimated in *§ 2.2.4.1*. Moreover, it is important to note that this estimate of the temperature relies among others on the assumption that parent clusters and fragments are detected with equal efficiency. As discussed in *§ 2.2.4.1*, this is unlikely to occur and it therefore introduces an additional uncertainty on the estimate of the clusters temperature. Assuming that we only detect 10 % of the fragments, then the above calculation underestimates the temperature of ValLi$^+$•(H_2O) by ~ 15 %.

Despite the crude estimate, it appears that the temperature of the ions released from the hexapole is higher than what we would have expected after thermalization in the multipole (cf. *§ 2.2.2*). Ions could be heated in the hexapole by energetic collisions as they are accelerated either in the rf field near the poles or by the potential applied to dump them from the trap. It is also important to note that the temperatures obtained may be overestimated if there is no statistical randomization of the energy in the system among all of the different degrees of freedom, in which case the RRKM model would not apply.

The temperature of the ion beam estimated above is high enough so that several conformers of comparable energies may be populated. An important implication for the spectroscopic experiment is that the vibrational spectrum measured for one particular hydrate most probably results from the overlap of the contributions of many different conformers. However, the latter will depend mainly upon the height of the barriers between different conformations and how those compare to the ion internal energy. For instance, we could have more than one conformer even at a few degrees Kelvin if the energy barriers are very low.

2.3 PHOTODISSOCIATION EXPERIMENT COUPLING PULSED LASERS WITH A PULSED ION SIGNAL

2.3.1 Spectroscopic scheme

The energy level diagram, shown in *Fig 2.9*, illustrates the spectroscopic scheme employed for the photodissociation of protonated or lithiated amino acid water clusters. Tunable IR laser radiation in the light atom stretching region (2900 – 3800 cm^{-1}) is used to excite the parent cluster $AA{\bullet}X^{+}(H_2O)_n$ in the octopole ion guide, which dissociates by loss of one water molecule. Infrared photons can be absorbed either by the amino acid functional groups and backbone, or by the water adducts forming the cluster. Thus, resonant excitation of the fundamental X-H stretch (X = O, N or C) promotes molecules from the ground vibrational state to the first vibrationally excited state, which probably dissociate after intramolecular vibrational redistribution (IVR) provided that the energy supplied is above the dissociation threshold. Since we see unimolecular dissociation already in the absence of laser light, the ions must be warm enough to dissociate. An action spectrum can be obtained if the addditional energy from the IR photon increases sufficiently the dissociation rate so that it is possible to discriminate between the photo-induced ion signal and that originating from spontaneous dissociation.

We use the hydride stretch spectral region to probe structural changes of the hydrated amino acids, based on the band shifts of functional OH and NH groups or their appearance/disappearance upon addition of water molecules in the solvation shell.

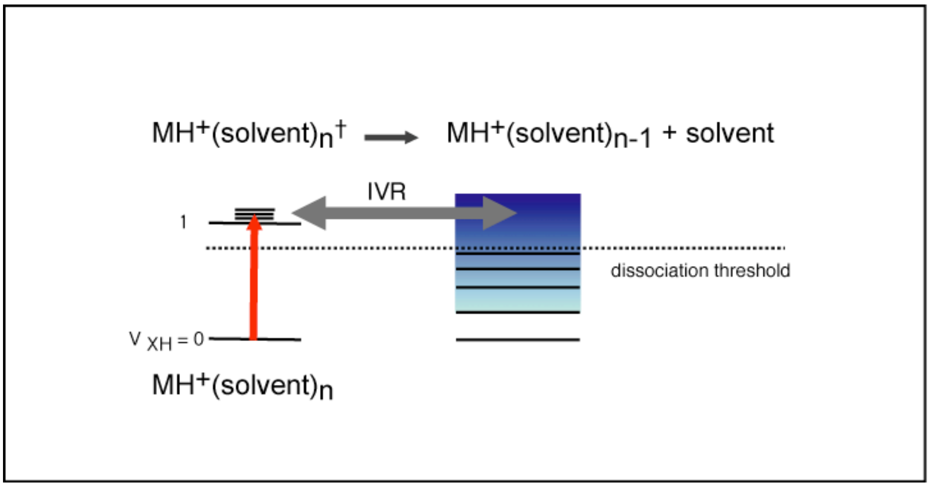

Fig 2.9: IR spectroscopic scheme.

2.3.2 Tunable infrared generation optical layout

Fig 2.10 depicts the optical layout of the laser system that generates tunable infrared radiation around 3 μm. IR pulses of energy up to 6 mJ/pulse are produced by a two-stage difference frequency mixing (DFM) setup. The second-harmonic output of a single-mode Nd:YAG laser (Spectra Physics GCR-270) pumps a dye laser (Lamba Physik Scanmate) which generates tunable visible radiation between 629 and 666.5 nm (50 mJ) using DCM laser dye. The 1064 nm fundamental of the same single mode Nd:YAG laser passes through a λ/2 plate and a polarizing beam splitter, which produces a *p*-polarized beam of 150 mJ/pulse and an *s*-polarized beam of 300 - 400 mJ/pulse. By rotating the λ/2 plate one can adjust the power partition between *p*- and *s*-polarized light. The output of the dye laser is propagated through a beam-expanding Galileo telescope (3:1 magnification, F= - 50 cm and F= 150 cm lenses) to match the beam diameter of the 150 mJ *p*-polarized fundamental. Both beams are combined on a CaF_2 dichroic mirror (HR at 540 - 740 nm, HT at 1064 nm) before difference frequency mixing in a $LiNbO_3$ crystal. The crystal is installed in an Inrad Autotracker II, where it is automatically rotated at the phase matching angle when scanning the wavelength of the dye laser. The resulting 4 – 5 mJ/pulse beam near 1.6 μm emerging from the first DFM stage is separated from the 1064 nm pump beam by a CaF_2 dichroic mirror while the residual visible light is absorbed on a silicon plate. The remaining 300 – 400 mJ of the Nd:YAG *s*-polarized fundamental is directed through a λ/2 plate and combined with the 1.6 μm signal wave on an infrared fused silica dichroic mirror for a second stage difference frequency mixing using two 25 mm long $KTiOPO_4$ (KTP) crystals (11×11mm aperture) arranged in a walkoff-compensated configuration and stabilized against temperature drifts induced by the pump beam. They are mounted in a custom rotating stage for phase matching angle tracking during a laser scan. This second DFM stage generates up to 6 mJ/pulse of idler around 3 μm. The KTP crystals allow tuning of the infrared frequency from 3300 to 3800 cm^{-1}, while a pair of KTA ($KTiAsO_4$) crystals provides access to lower frequencies (2900 – 3300 cm^{-1}). Note that we generate the signal wave at 1.6 μm in the first DFM stage to overcome problems related to the fact that there is strong water absorption in the 3 μm region.

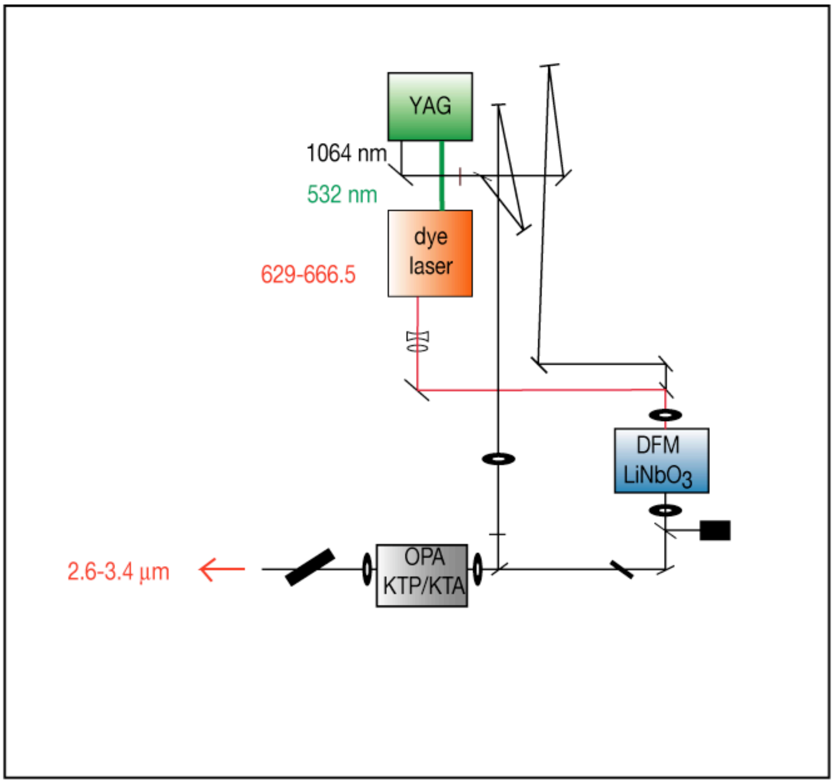

Fig 2.10: Schematic overview of the laser setup.

The residual 1064 nm pumping radiation is separated from the s-polarized 3 μm beam using a CaF_2 dichroic mirror, and a pair of silicon plates reflects the remainder 1.6 μm beam. The *p*-polarized 3 μm radiation is then directed towards the vacuum chamber housing the second quadrupole deflector through a BaF_2 window mounted at Brewster angle and counter-propagates to the ion beam towards the octopole ion guide and the first deflector emerging out of the vacuum system through a BaF_2 window at Brewster angle.

A Labview program controls communications with the data acquisition card, steps the dye laser wavelength, rotates the second-stage DFM crystals for phase angle matching at each laser step (wavelength), and retrieves data from the gated photon counter. Instrument control and data acquisition of laser-on and laser-off counts are operated through GPIB interfaces.

2.3.3 Timing of the sequence of events

The nanoES source continuously produces a distribution of non-covalently bound complexes, which are accumulated and trapped in the ‘rf only’ hexapole using a potential barrier of 10 V above ground potential in the present experiments. This voltage is applied on the hexapole exit electrode, which is pulsed at 40 Hz and transforms the continuous electrospray ion current into a pulsed signal.

Dumping the hexapole ion reservoir (at 40 Hz, twice faster than the 20 Hz frequency of the pulsed lasers) allows for measurement of the non-irradiated ion signal between each laser shot for normalization purposes. The optimum storage time in the hexapole is different for each cluster investigated and relies upon a compromise between the duty cycle of the experiment, enhancement of ion signal by accumulation in the hexapole, and dissociation of the weakly-bound edifices by collisions or space charge effects in the moderate pressure region of the multipole. Typical trapping times range between 10 and 20 ms, with shorter storage times necessary for the most fragile clusters of protonated tryptamine while the hydrates of amino acids are more strongly bound and can be stored almost for the whole duration of one cycle (25 ms at 40 Hz).

As discussed in (*§ 1.1.3.1.1* and *§ 1.3.2.3.2*) the successful implementation of laser photodissociation in the ion guide of the spectrometer requires a good overlap between laser light and the ion packet, both in space and time. Thus, the width of the ion pulse released from the hexapole and its time-of-flight to the entrance of the octopole ion guide are important parameters for adjusting the delay between the hexapole dumping pulse and the laser firing pulse. We roughly adjust this delay so as to irradiate the ion packet once it fills the length of the octopole ion guide. Moreover, due to the pulsed nature of the ion signal, the detection of fragments at the final stage of the mass spectrometer should also be synchronized with either the hexapole dumping pulse or laser radiation pulse.

Since, the ion densities achieved in these hydration experiments require counting of the fragments at the detector (cf. *§ 2.3.4*), we employ a gated detection scheme, where ions are counted within an adjustable gate determined by the width in time of the ion packet arriving at the detector. The delay of the detection pulse depends on the time-of-flight of fragments to the detector.

The sequence of pulses delivered by an 8-channel pulse delay generator (Model 555, Berkeley Nucleonics Corporation, USA) and used to extract spectroscopic information is illustrated in *Fig 2.11*. It consists of the following events: (1) trapping of the ions in the hexapole, (2) release of an ion packet from the ion trap, (3) irradiation of the mass selected parent beam in the octopole ion guide for every other ion packet dumped from the hexapole, (4) counting of the fragmentation ion signal arising alternatively from spontaneous unimolecular dissociation or enhancement of the latter by photodissociation upon absorption of the laser light and finally (5) data acquisition of laser-on and laser-off fragment ion signals.

A coarse adjustment of the delays between the pulses synchronizing this sequence of events (cf. *Fig 2.11*) is based on the times-of-flight mentioned above. However fine-tuning of the laser and detection pulse delays, along with the determination of the detection gate width, is achieved upon optimization of the photofragmentation ion signal measured at a fixed wavelength for which absorption occurs. Photon absorption is monitored by the increase of the fraction of molecules dissociated. Parking the laser at the maximum of a transition, while performing mass analysis of the fragments in the final quadrupole, shows that for each degree of hydration (n = 1 – 4) investigated, only the fragment mass corresponding to the loss of a unique water molecule is appreciably detectable, as it is also observed in the absence of laser activation.

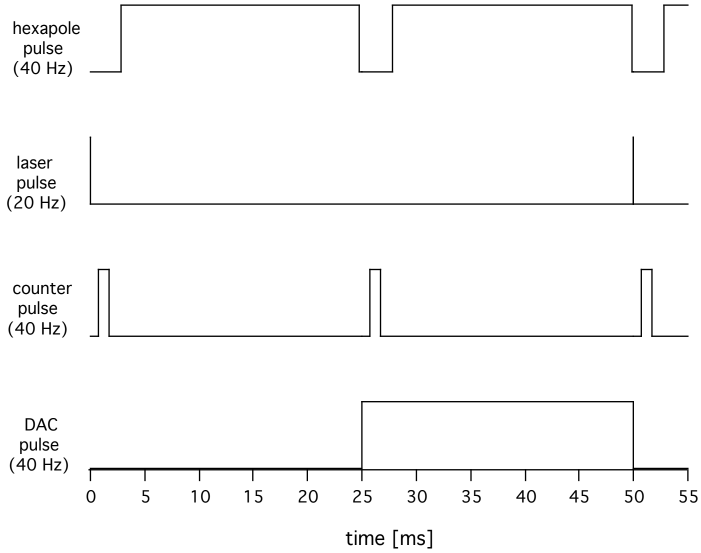

Fig 2.11: Timing of the experiment.

2.3.4 Infrared action spectra

The vibrational action spectrum is generated by counting the photo-fragmented ions (laser-on) as a function of the wavelength when the first quadrupole mass filter is tuned to select a specific mass (AA•$X^+(H_2O)_n$) from the distribution of clusters emerging from the hexapole, and the final quadrupole sits on the mass of AA•$X^+(H_2O)_{n-1}$. We only detect a photodissociation signal of up to a couple of counts/shot for the hydrates of lithiated valine and up to 4 – 5 counts /shot for those of protonated valine. Protonated tryptophan and protonated tryptamine water clusters give rise to a higher photofragmentation signal with up to ~10 counts/shot detected. Each data point on the infrared spectra recorded represents an averaged fragment ion signal of 200 laser shots. Depending on the nature of the amino acid core, we observe less than 5 % photo-dissociation yield for the hydrates, and the fraction dissociated is smaller for low hydration levels.

A two-channel gated photon counter (Stanford Research Systems SR400), measures the product ion signal within a 1 ms gate width after amplification by a fast-timing preamplifier (Model VT 120, Ortec, USA). A data acquisition card (National Instruments PCI-6110 S) is synchronized with the hexapole trapping pulse and collects laser-on and laser-off data at 40Hz. We assume that the number of fragments produced by spontaneous unimolecular dissociation is proportional to the number of parent ions and can be used to normalize the photo-fragmentation ion signal with respect to the parent ions.

Assuming that a photon energy of 3000 cm^{-1} is added to the monohydrate of lithiated valine complex, this represents an increase of energy of ~ 50 cm^{-1} / vibration, or put otherwise, an increase of 80 K in the temperature of the cluster ($\Delta E = k_B.\Delta T$). Based on the temperature of the clusters estimated in *§ 2.2.4.2* and adding the aforementioned increase of temperature we evaluate a photodissociation rate of 2.5 10^2 s^{-1} for this cluster. This corresponds to a 4 ms dissociation timescale, which is long in comparison to the time-of-flight of ions in the spectrometer (hundreds of microseconds). Thus, the action spectrum measured in our instrument may not reflect the absorption spectrum of the molecules, and the amount of photofragmentation signal detected depends on the delay time between laser irradiation and detection of the photofragments. Moreover, if some vibrational modes are associated with slower dissociation kinetics they will show up with low intensities or may not be detected at all, therefore skewing the intensities observed. It is also probable that the features observed in the spectra are dominated by the contribution of ions with the higher internal energy from the distribution produced, indicating that our detection scheme is not sensitive to low-energy conformers. Thus, although action spectroscopy is a very sensitive technique for the detection of photon absorption upon laser excitation, it can introduce some bias in the experiment under the conditions discussed above. Note, that IR photofragmentation spectra of pure protonated water clusters measured in three different and independent studies by Headrick *et al.* [11], Shin *et al.* [12] and Jiang *et al.* [13] do not show a good overlap of the spectral features. In these studies, the clusters have been prepared by different means and are probably characterized by different temperatures, which could explain the inconsistency of the features observed in the low-energy end of the spectra.

2.4 THEORETICAL STUDIES

The non-covalent complexes investigated here are characterized by a structural diversity arising from the variety of binding sites and motifs of solvent molecules in the clusters, but also from the flexible backbone of amino acids, which can adopt many different conformations. These small structural changes may give rise to many conformers of comparably low energy. Our spectroscopic technique is not conformer-specific, and thus it is possible, and even likely, that more than one conformer of the hydrated charged amino acids contributes to each infrared spectrum. In order to disentangle the number of different conformers appearing in each spectrum, we have recourse to theoretical calculations. Before presenting the experimental results and making use of theory for the interpretation of the photofragmentation spectra obtained, we report below the theoretical methods employed for this task.

The work presented in this thesis largely results from experimental studies. However, theoretical studies are necessary for the interpretation of the data. We use theory to predict possible low-energy structures of the clusters investigated and their vibrational frequencies. The goal is to compare the calculated spectra to the experimental ones and infer structural information on the hydrates experimentally observed. We report in this part the general procedure and methods employed for the computations.

2.4.1 General approach

The computational work consists first in sampling the conformational space before performing more accurate, but also more computationally demanding, electronic structure calculations.

Low-energy structures are identified through a conformational search using the appropriate force field and aided by chemical intuition. The resulting geometries of energy lower than a certain threshold value are refined using density functional theory (DFT), which is less computationally demanding than *ab initio* methods and is applicable to the study of clusters [14] but also for investigations of flexible biomolecules [15].

In all of these calculations, the non-covalent complex is treated as an ensemble and no separate computations are performed on the isolated amino acid core. However, non-zwitterionic and zwitterionic structures necessitate separate searches, while some hydrogen bonding motifs or cis/trans isomerizations (missing from the conformational search) are also sampled, demonstrating the importance of chemical intuition.

All of the computational work for lithiated and protonated valine water clusters was done at University of California, Berkeley in Pr. E. R. Williams group, including extensive conformational searches and high-level DFT calculations of a large number of structures. These theoretical studies provided a strong support for the analysis of the experimental data for valine and allowed us to establish a relationship between some typical frequencies or frequency shifts and structural signatures characteristic of amino acids functional groups involved in some particular H-bonding with water.

For protonated tryptophan, such an exhaustive study was not realistic on the timescale of this thesis with the computational means of our laboratory, and the interpretation of the experimental spectra was largely based on the comparison with those of protonated valine and protonated tryptamine. Calculations were used to confirm or rule out some of the assignments when the conclusions drawn from this comparative study were not strong enough to infer structural information. Thus, DFT calculations (at the same level of theory as for valine) were performed on the hydrates of protonated tryptophan, based on candidate structures proposed by chemical intuition. The exact procedures followed in each case are described below.

2.4.2 Calculations for Val•$H^+(H_2O)_n$ and Val•$Li^+(H_2O)_n$

Geometries for the low-energy structures of Val•$Li^+(H_2O)_{1\text{-}3}$ at a B3LYP/6-31++G** level of theory have been reported in the literature by Williams and coworkers [2]. They were used for the interpretation of blackbody infrared dissociation (BIRD) rates and to infer structural information about these hydrates. Since the BIRD data reported for Val•$Li^+(H_2O)_3$ imply a possible observation of zwitterionic valine in this complex, more exhaustive calculations were carried out for the present work.

Candidate low-energy structures of Val•$Li^+(H_2O)_3$ and Val•$H^+(H_2O)_{1\text{-}3}$ were determined using a combination of conformational searching and chemical intuition. Initial structures for these clusters were generated using Monte Carlo conformation searching with the MMFF94 force field using Macromodel 8.1 (Schrodinger, Inc., Portland, OR). For the initial search, no constraints were placed on the molecules, and at least 10,000 conformations were generated. In these simulations, the significant hydrogen bonding motifs were identified within the first several thousand conformations generated. In the case of Val•$Li^+(H_2O)_3$, separate searches were performed for the non-zwitterionic cluster and the zwitterionic cluster in which the amine nitrogen is protonated and the carboxylic acid deprotonated. For Val•$H^+(H_2O)$, the amine nitrogen and carbonyl oxygen were each evaluated as potential protonation sites. In addition, a salt bridge containing cluster with a protonated amine, a deprotonated carboxylic acid, and a hydronium was considered. In subsequent quantum mechanical calculations, all structures within 30 kJ/mol of the lowest-energy structure minimized to forms without a salt-bridge and with the amine group protonated. Based on these results, the amino acid in Val•$H^+(H_2O)_{2\text{-}3}$ was assumed to adopt a structure with a protonated amine and a neutral carboxylic acid group. Additional candidate structures were generated by altering structures found in the Monte Carlo simulations by incorporating an additional water molecule or by changing the cis/trans conformation of the carboxylic acid.

After identifying low-energy structures, hybrid method density functional calculations using the Becke3 hybrid functional with the Lee-Yang-Parr correlation functional (B3LYP) were performed using Jaguar v. 5.5 (Schrodinger, Inc., Portland, OR) with the 6-31G* basis set. Final geometries were then obtained by subsequent minimization using the 6-31++G** basis set. Vibrational frequencies and intensities were calculated using numerical derivatives of the B3LYP/6-31++G** energy minimized Hessian. A constant scale factor of 0.956 was applied to all calculated frequencies in all spectra to account for anharmonicity and other factors. This single scale factor was obtained by an approximate best fit to all measured spectra.

2.4.3 Calculations for Trp•$H^+(H_2O)_n$

Based on the results obtained from the extensive computational work on lithiated and protonated valine water clusters, a less exhaustive search was performed for the hydrates of protonated tryptophan. The general procedure is as follows. We first calculate the lowest-energy conformers of bare tryptophan and use them as starting structures for the amino acid core, while chemical intuition provides the initial guess for the possible binding sites of water. We then sample the conformers of the candidate structures proposed, by simple dynamics trajectory simulations at 300 K using CAChe WS Pro 6.1 software package (Oxford Molecular Ltd, Fujitsu). Finally, selection of a few structures representative of the significant binding motifs of water are optimized in subsequent DFT calculations using Gaussian 03, Inc, Wallingford, CT, USA [16]. Geometries are first optimized at the B3LYP/6-31G* level of theory, while B3LYP/6-31++G** is used for final energy minimizations and harmonic frequency calculations. All harmonic frequencies are scaled to account for systematic errors and anharmonicity. The scaling factor (0.956) is determined empirically from the approximate best fit to all measured spectra, as in the case of charged valine water clusters.

2.4.4 Comparing theory and experiment

A few notes of caution are in order regarding the comparison of experiment and theory to avoid misleading conclusions. The remarks below deal more specifically with the aspects of calculations and are complementary to those discussed in *§ 2.3.4*.

2.4.4.1 Energies

A well-known problem of DFT calculations is the poor treatment of dispersion interactions [17]. Therefore, structure predictions for increasing cluster sizes should be treated with care: in general, one should not make too much distinction between two species that have energies within 10 kJ/mol

Since the temperature of the clusters formed in our instrument has been estimated to be above room temperature *§ 2.2.4.2*, the structures calculated are not compared on the basis of zero point corrected energies but include thermal energy corrections accounting for the effects of molecular translation, vibration, and rotation at this particular temperature. The values reported on the spectra correspond to enthalpies at 298 K.

Although computations aim at finding the low energy structures, higher energies structures are also sampled through the conformational space search and calculated at a higher level of theory with DFT methods. Calculations of higher energy structures are important, since several conformers may be present in the ion beam as discussed in *§2.2.4.2*.

2.4.4.2 Intensities

The intensities predicted by theory are those of an absorption spectrum. Thus, they do not necessarily reflect the intensities of the action spectra measured in our experiments and should be treated with care. Indeed, as discussed in *§ 2.3.4* the spectral intensities in the experiment depend upon the kinetics of photofragmentation. For instance, it is not unlikely that some of the vibrational modes are not strongly coupled (or coupled at all) to dissociation so that they would not appear in the action spectrum.

2.4.4.3 Frequencies

In non-covalent complexes, the weak bonds and possibly the large amplitude vibrational motions involved may give rise to important anharmonic effects, which cannot be described in the harmonic approximation [11] [18]. Application of a scaling factor to harmonic frequencies as we do, is sometimes not enough to account properly for anharmonicity. Thus, possible discrepancies between some of the stretching modes predicted by theory and those observed experimentally may arise from the lack of a real treatment of anharmonic effects. On the other hand, in the same spectrum, other modes can be predicted with a high level of accuracy if they don't fall within these limitations.

It is important to note that because the spectra are calculated in the "double-harmonic" approximation (i.e., linear dipole moment function and harmonic vibrations), the calculated results will not predict any overtone vibrations.

References

1. Zwier, T. S., J. Phys. Chem. A (2001), 105, 8827-8839.
2. Lemoff, A. S. and Williams, E. R., J. Am. Soc. Mass Spectrom. (2004), 15, 1014-1024.
3. Drahos, L. and Vekey, K., J. Mass Spectrom. (2001), 36, 237-263.
4. Bordas-Nagy, J. and Jennings, K. R., Int. J. Mass Spectrom. Ion Process. (1990), 100, 105-131.
5. Douglas, D. J., J. Am. Soc. Mass Spectrom. (1998), 9, 101-113.
6. Douglas, D. J. and French, J. B., J. Am. Soc. Mass Spectrom. (1992), 3, 398-408.
7. Tolmachev, A. V., Udseth, H. R., and Smith, R. D., Rapid Commun. Mass Spectrom. (2000), 14, 1907-1913.
8. Gerlich, D., Adv Chem Phys (1992), 82, 1-176.
9. Wyttenbach, T., Witt, M., and Bowers, M. T., J. Am. Chem. Soc. (2000), 122, 3458-3464.
10. Baer, T. and Hase, W. L., Unimolecular reaction Dynamics. Theory and Experiments. 1996, New York: Oxford University Press.
11. Headrick, J. M., Diken, E. G., Walters, R. S., Hammer, N. I., Christie, R. A., Cui, J., Myshakin, E. M., Duncan, M. A., Johnson, M. A., and Jordan, K. D., Science (2005), 308, 1765-1769.
12. Shin, J.-W., Hammer, N. I., Diken, E. G., Johnson, M. A., Walters, R. S., Jaeger, T. D., Duncan, M. A., Christie, R. A., and Jordan, K. D., Science (2004), 304, 1137-1140.
13. Jiang, J. C., Wang, Y. S., Chang, H. C., Lin, S. H., Lee, Y. T., Niedner-Schatteburg, G., and Chang, H. C., J. Am. Chem. Soc. (2000), 122, 1398-1410.
14. Jiang, J. C., Chang, H. C., Lee, Y. T., and Lin, S. H., J. Phys. Chem. A (1999), 103, 3123-3135.
15. Robertson, E. G. and Simons, J. P., Phys. Chem. Chem. Phys. (2001), 3, 1-18.
16. Gaussian 03, R.-B., M. J. Frisch, G. W. Trucks, H. B. Schlegel, G. E. Scuseria, M. A. Robb, J. R. Cheeseman, J. A. Montgomery, Jr., T. Vreven, K. N. Kudin, J. C. Burant, J. M. Millam, S. S. Iyengar, J. Tomasi, V. Barone, B. Mennucci, M. Cossi, G. Scalmani, N. Rega, G. A. Petersson, H. Nakatsuji, M. Hada, M. Ehara, K. Toyota, R. Fukuda, J. Hasegawa, M. Ishida, T. Nakajima, Y. Honda, O. Kitao, H. Nakai, M. Klene, X. Li, J. E. Knox, H. P. Hratchian, J. B. Cross, V. Bakken, C. Adamo, J. Jaramillo, R. Gomperts, R. E. Stratmann, O. Yazyev, A. J. Austin, R. Cammi, C. Pomelli, J. W. Ochterski, P. Y. Ayala, K. Morokuma, G. A. Voth, P. Salvador, J. J. Dannenberg, V. G. Zakrzewski, S. Dapprich, A. D. Daniels, M. C. Strain, O. Farkas, D. K. Malick, A. D. Rabuck, K. Raghavachari, J. B. Foresman, J. V. Ortiz, Q. Cui, A. G. Baboul, S. Clifford, J. Cioslowski, B. B. Stefanov, G. Liu, A. Liashenko, P. Piskorz, I. Komaromi, R. L. Martin, D. J. Fox, T. Keith, M. A. Al-Laham, C. Y. Peng, A. Nanayakkara, M. Challacombe, P. M. W. Gill, B. Johnson, W. Chen, M. W. Wong, C. Gonzalez, and J. A. Pople, Gaussian, Inc., Wallingford CT, 2004.
17. Hobza, P., Sponer, J., and Reschel, T., J. Comput. Chem. (1995), 16, 1315-1325.
18. Hammer, N. I., Diken, E. G., Roscioli, J. R., Johnson, M. A., Myshakin, E. M., Jordan, K. D., McCoy, A. B., Huang, X., Bowman, J. M., and Carter, S., J. Chem. Phys. (2005), 122.

Chapter 3

IR SPECTROSCOPY OF LITHIATED- AND PROTONATED-VALINE WATER CLUSTERS

The spectroscopic experiments on lithiated valine reported here address the question of the combined effect of metal ion binding and hydration on zwitterion formation. As discussed in the *Introduction* of this thesis, electrostatic interactions between amino acids (or related molecules) and a metal ion may stabilize the zwitterion form through formation of a salt-bridge structure. However, such a structure is in competition with a charge solvated structure, where the amino acid (or the related molecule) retains its neutral form and the backbone solvates the charge.

The combined effect of metal ion binding and hydration has been investigated by collision induced dissociation (CID) [1, 2] and BIRD experiments [3-5] as well as theoretical calculations [6]. In an extensive set of studies, Williams and coworkers measured the dissociation rates and water binding energies of hydrated valine-cation clusters [4, 5, 7] and compared them with model compounds known to exist in either zwitterionic or non-zwitterionic structures and with theoretical calculations. Although their data clearly showed a change in structure upon addition of a third water molecule to the cluster, it was not possible to determine unambiguously the number of water molecules necessary to stabilize the zwitterionic form versus the non-zwitterionic form for valine. One of the motivations of the present work was to measure the IR spectra of $\mathrm{Val{\bullet}Li^+(H_2O)_{n=1\text{-}4}}$ using our optical technique to investigate more fully the issue of zwitterion formation in these clusters. In parallel with this, we also investigate the protonated analogs of these clusters, $\mathrm{Val{\bullet}H^+\,(H_2O)_{n=1\text{-}4}}$, since they provide valuable insight on the assignments of the vibrational spectra as well as an interesting comparison to the lithiated species.

3.1 NOTATION CONVENTIONS

We use the following nomenclature for calculated cluster conformations: a first letter (H or L) to distinguish protonated and lithiated clusters followed by a number (indicating the number of water molecules) and a letter (A, B, C, etc.) to distinguish different conformations of the same cluster. Thus, H1_A would be a calculated conformation of mono-hydrated, protonated valine while L3_C would be that of a lithiated valine cluster with three water molecules.

We adopt certain notation conventions to characterize the bonding properties of solvent molecules and the amino acid isomers. Depending on the hydrogen-bonding motif, we use the convention of "donor" if the water molecule donates the hydrogen atom and "acceptor" when the interaction involves the free lone pair of the oxygen atom. Hence we label in parenthesis a single-acceptor water molecule (A), a single donor (D), a double-acceptor (AA), and a single-acceptor-single-donor (AD).

The following definitions characterize the amino acid conformation based on the orientation of the amino group (NH_2 or NH_3^+) relative to the carboxylic group (COOH). We refer to a *syn* conformer if the amino or ammonium group faces the carbonyl oxygen of COOH, and to an *anti* conformer if it faces the O-H of COOH after rotation of the carboxylic group about the C-C^a bond (cf. *Fig. 3.1*). Moreover, we adopt the abbreviations NZ to describe a charge solvated structure in which the amino acid is in its neutral (i.e., non-zwitterionic) form, whereas Z stands for a salt-bridge structure where the amino acid is a zwitterion.

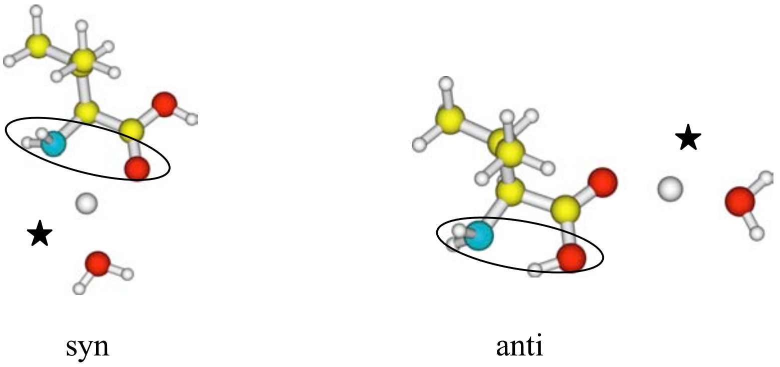

Fig. 3.1: Illustration of syn and anti conformations (in circle); and NO- vs. OO-coordination of the lithium ion (★)

In lithiated water clusters, we distinguish different structures based on the coordination site of the lithium cation. An "NO-coordinated" structure denotes Li^+ bonded between the nitrogen atom of the amino group and the carbonyl oxygen of the C-terminus, whereas “OO-coordination” indicates binding of the lithium cation between the oxygen atoms of the carboxylic acid (cf. *Fig. 3.1*).

3.2 COMPARISON OF IR SPECTRA FOR PROTONATED- AND LITHIATED-VALINE WATER CLUSTERS

Infrared photofragmentation action spectra obtained for Val•$H^+(H_2O)_{n=1-4}$ in the region 2900 - 3800 cm^{-1} are shown in *Fig. 3.2*, and those for Val•$Li^+(H_2O)_{n=1-4}$ in *Fig. 3.3*. Our general approach to interpreting these spectra is as follows. We first assign the major features of each spectrum by comparison with the IR spectra of isolated gas-phase valine, [8] hydrated alkali metal ion clusters, [9, 10] protonated amine water clusters [11, 12] as well as hydrated clusters of other protonated amino acids measured in our laboratory. We then compare assigned spectra to those calculated for low energy structures of the corresponding species to identify likely conformations. In doing so, it is important to remember that there may be more than one stable conformer formed for a given cluster size, each of which would contribute to a particular spectrum (cf. *Chapter 2*).

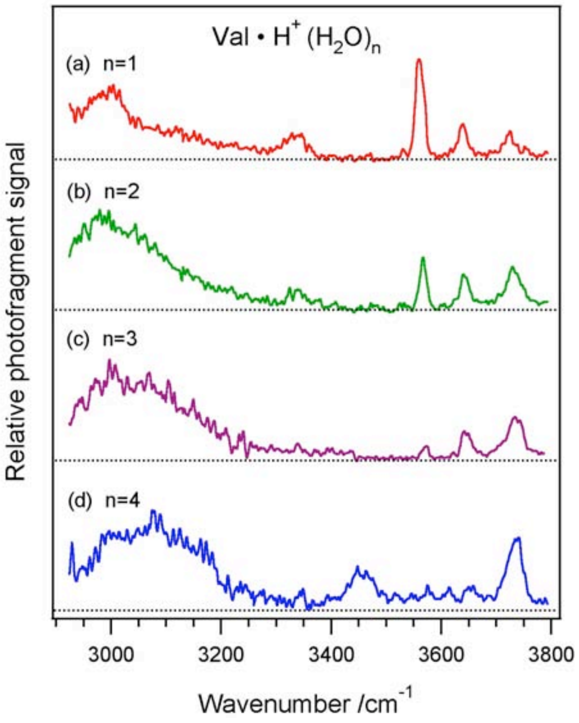

Fig. 3.2: Infrared photofragment spectra of Val•$H^+(H_2O)_{n=1-4}$

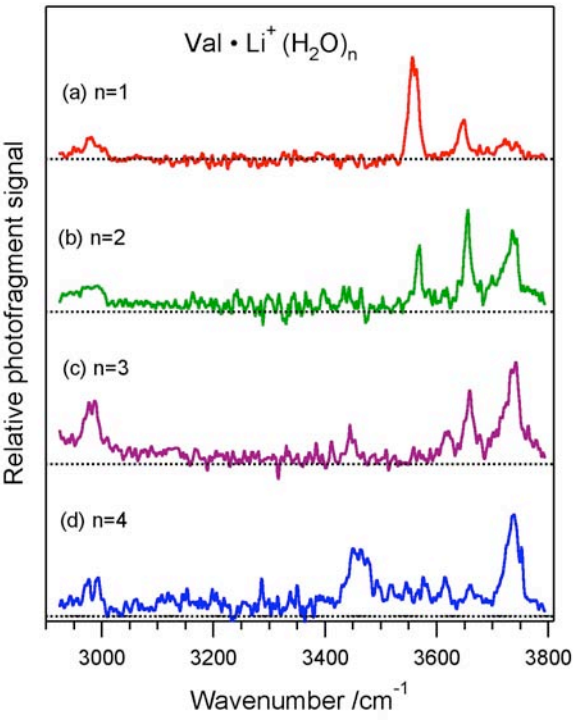

Fig. 3.3: Infrared photofragment spectra of Val•$Li^+(H_2O)_{n=1-4}$

At first glance, it is worth noting that although these two families of clusters are different species with a completely different charge carrier, their spectra show remarkable similarities in the high frequency portion of the corresponding spectra. We discuss in detail below both the similarities and differences in the spectra of these two cluster families and the implications for understanding the solvation of these species.

3.3 IR SPECTRA OF PROTONATED VALINE WATER CLUSTERS

3.3.1 Protonated valine water clusters Val•H$^+$ $(H_2O)_n$

The hydration process is controlled by a delicate balance of non-covalent interactions between neighboring groups within the molecule and between the molecule and its solvent environment. The isopropyl residue side chain of valine is neither likely to interact through H-bonding with water molecules nor give rise to intra-molecular self-solvation of the amino acid, leaving the N-terminus and the C-terminus as the only possible sites for water attachment during microsolvation. Water may attach to the two oxygen atoms, the hydrogen atom of the carboxylic group, or to one of the three hydrogen atoms of the protonated amino group.

Protonation occurs at the amino group of valine, which removes the free lone pair of the nitrogen atom and thus limits the hydrogen-bonding mode of the N-terminus to a “donor-only” site. This should have important structural consequences, since the conformational preferences of neutral amino acids [8, 13] are influenced by stabilization of the intermolecular hydrogen bond established between the free lone pair of the nitrogen and the donating proton of the carboxylic acid terminus. Moreover, the presence of the charge introduces an additional electrostatic driving force for intermolecular non-covalent interactions, especially with the water molecules.

3.3.2 ValH$^+$•(H_2O)

Three groups of transitions are visible in the spectrum of ValH$^+$•(H_2O): a strong absorption band at 3560 cm^{-1}, two weaker bands at 3640 and 3725 cm^{-1} and some broader features below 3400 cm^{-1}. We make preliminary spectral assignments by comparison with spectroscopic results of analogous chemical compounds, either obtained experimentally in our lab or available in the literature. As shown in *Fig. 3.4*, the three highest frequency bands are also present in the ValLi$^+$•(H_2O) and TrpH$^+$•(H_2O) spectra, which suggests that they arise from vibrations common to these clusters: two water O-H stretches, the carboxylic acid O-H stretch and the N-H stretches of the amino group. In order to identify unambiguously which of these three common features belongs to the carboxylic acid O-H stretch, we also measured the IR spectrum of water clusters of tryptamine, a tryptophan analog containing no carboxylic acid group: upon removal of the COOH, the 3560 cm^{-1} band disappears.

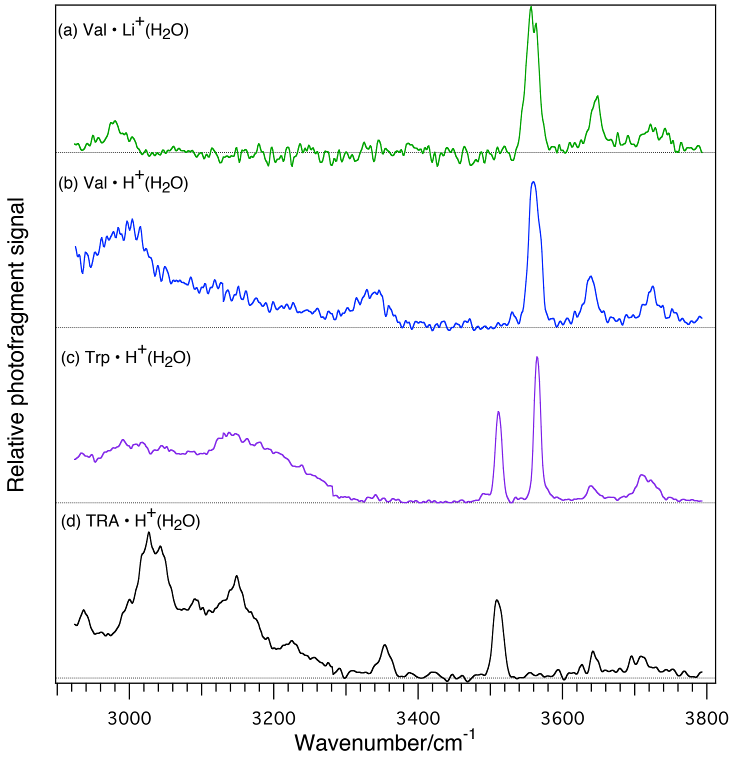

Fig. 3.4: Comparison of infrared spectra of (a) Val•Li$^+$(H$_2$O); (b) Val•H$^+$(H$_2$O); (c) Trp•H$^+$ (H$_2$O) and TRA•H$^+$ (H$_2$O).

We assign the bands at 3649 and 3731 cm^{-1} to free water O-H stretches. Indeed, isolated gas-phase water exhibits two bands, the symmetric O-H stretch at 3657 cm^{-1} and the antisymmetric stretch at 3756 cm^{-1} [14]. In Val•H$^+$(H$_2$O) these bands are shifted to lower frequency and the symmetric stretch presents a higher IR relative intensity over the antisymmetric stretch as also reported by Lee and coworkers in the spectra of hydrated, protonated amines [11, 12]. We assign the feature at 3337 cm^{-1} to non-hydrogen bonded NH stretches, as these fall in the region observed in vibrational spectra of protonated ammonia and protonated amines [11, 15], where they appear to gain intensity compared to neutral amines [16]. Upon forming a hydrogen bond, ammonium NH stretches tend to shift to lower frequency and broaden [12], and this can account for the broad structures below 3200 cm^{-1}, which we observe in all hydrated amino acids where we expect to have a solvated, protonated amine (see for example, the hydrated tryptophan spectrum in *Fig. 3.4 (c)*. The CH stretch bands should appear in the region of 3000 cm^{-1}, but these are likely to be buried below the stronger hydrogen-bonded ammonium stretch bands.

While these assignments provide information about the light-atom stretch vibrations in the cluster as well as hydrogen-bonding sites, they do not provide a detailed picture of the cluster conformation. More detailed structural information can only be obtained by comparison with calculated spectra of stable conformers, as shown below in *Fig. 3.5*.

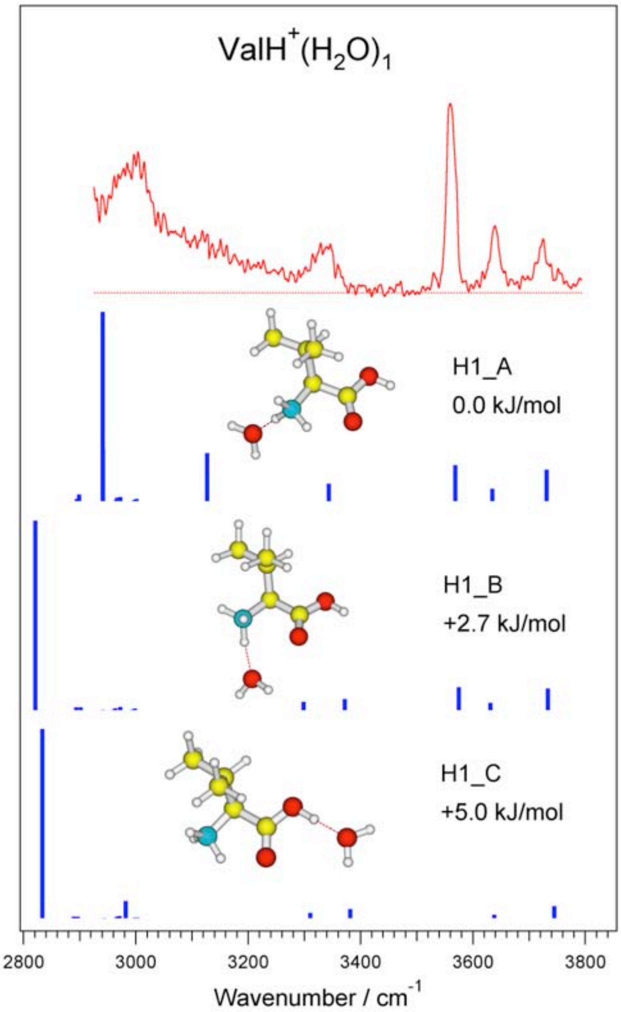

Fig. 3.5: Comparison of measured infrared spectra of Val•H$^+$(H$_2$O) with calculated spectra corresponding to the structures shown.

All lowest energy structures calculated for ValH$^+$•(H$_2$O) clusters are in a *syn* conformation (i.e., with the carbonyl facing the ammonium). In structures H1_A and H1_C (cf. *Fig. 3.5*), an additional stabilizing interaction occurs between the ammonium group and the carbonyl oxygen. In structure H1_B the water interacts along an N-H bond facing the carbonyl oxygen and breaks this intramolecular interaction. The major difference between H1_A and H1_C is the hydrogen-bonding site of the water, which occurs on the ammonium group in the former and the carboxylic acid OH group in the latter. It is surprising that the calculations predict only a 5 kJ/mol energy difference between these two structures, as we would expect electrostatic interactions to cause a substantially larger stabilization upon hydration of the ammonium. This can be attributed to a significant destabilization of the amino-carboxylic oxygen interaction upon binding a water molecule to the amino group.

The observed spectrum is not consistent with that calculated for conformer H1_C, in which the COOH stretch is predicted to be red-shifted beyond the region of our measured spectrum. The strong absorption observed at 3560 cm^{-1} for the free COO-H thus rules out the possibility of water binding to the carboxylic acid. Structures H1_A and H1_B correctly predict the position of the free COOH band as well as the two free water stretches and the attachment of water to the ammonium group. The latter is consistent with the observed broad absorption band peaking around 3000 cm^{-1}.

The structures H1_A and H1_B differ by the orientation of the water molecule and the ammonium, which may influence the intramolecular stabilization of the ammonium charge by the carbonyl oxygen. There is good agreement between experimental spectrum and the calculated spectrum of H1_A, while the agreement with H1_B is noticeably worse in the low frequency part of the spectrum due to a stronger red-shift of hydrogen-bonded ammonium band. Because the shift causes the band to fall out of the frequency range accessed by our experiment, we cannot eliminate the possibility of the H1_B conformer contributing to the spectrum.

It is worth noting that calculations of the lowest energy conformer of bare $ValH^+$ predict a *syn* structure with an intramolecular interaction between the ammonium group and the carbonyl oxygen.

The calculated IR spectrum of $ValH^+$ (*Fig. 3.6*) indicates free NH stretch absorptions between 3300 and 3400 cm^{-1} and an N-H stretch interacting with the carbonyl ~ 3080 cm^{-1}. The conformer H1_A of $ValH^+\bullet(H_2O)$ also reveals an interaction between one of the ammonium NH and the carbonyl oxygen. This band is predicted in H1_A at higher frequency than that predicted for its counter part in bare protonated valine, which may suggest a weakening of the intramolecular interaction upon hydration of the ammonium group. It appears that the conformational preference of protonated valine is preserved upon addition of the first water molecule.

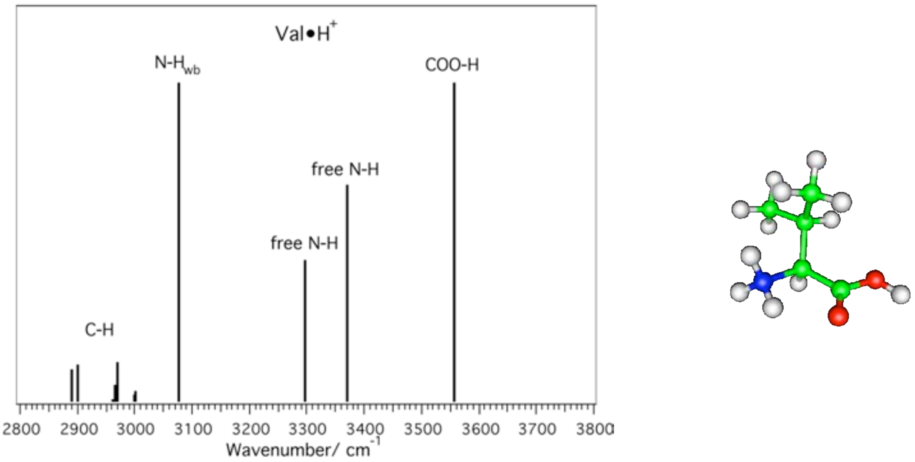

Fig. 3.6: Calculated spectrum for bare protonated valine.

3.3.3 $ValH^+•(H_2O)_2$

The spectrum of $ValH^+•(H_2O)_2$ (*Fig. 3.2*) is similar to that of the mono-hydrated species. All of the bands are slightly blue-shifted in the doubly hydrated species, and noticeable differences exist in the observed relative band intensities. The $ValH^+•(H_2O)_2$ spectrum is marked by a weaker absorption of the free NH stretch at 3340 cm^{-1} relative to the hydrogen bonded NH absorption centered at ~ 3020 cm^{-1}, which is broader in comparison with the spectrum of the singly hydrated species. Moreover, the free water vibrations at 3641 and 3730 cm^{-1} gain in relative intensity and become comparable to the free COO-H stretch at 3567 cm^{-1}.

As shown in *Fig. 3.7*, the minimum energy structure calculated for $ValH^+•(H_2O)_2$, H2_B, exhibits (somewhat surprisingly) a hydrogen bond between the carboxylic acid OH and the second water molecule, with the first water remaining on the ammonium. The persistence of the free COO-H stretch absorption at 3567 cm^{-1} in the observed spectrum, albeit at slightly reduced relative intensity, suggests that this conformer cannot be the dominant structure, although we cannot rule out its contribution to the observed spectrum since the hydrogen-bonded COOH falls outside our spectral range.

Calculations also show evidence for a stable conformer, H2_C, where the second water molecule resides in the outer solvent shell. Based on the calculated vibrational frequencies of this structure, the hydrogen-bonded ammonium would be red-shifted beyond our detectable frequency range, while the OH bond bridging the inner and outer-shell water molecules would give rise to a strong absorption band at 3284 cm^{-1}. While the experimental spectrum does indeed show a band near 3300 cm^{-1} which could in principle correspond to this shifted OH stretch, the persistence of the broad absorption around 3000 cm^{-1} in the measured spectrum and total absence of bands in this region of the calculated spectrum suggests that H2_C is not the dominant conformer.

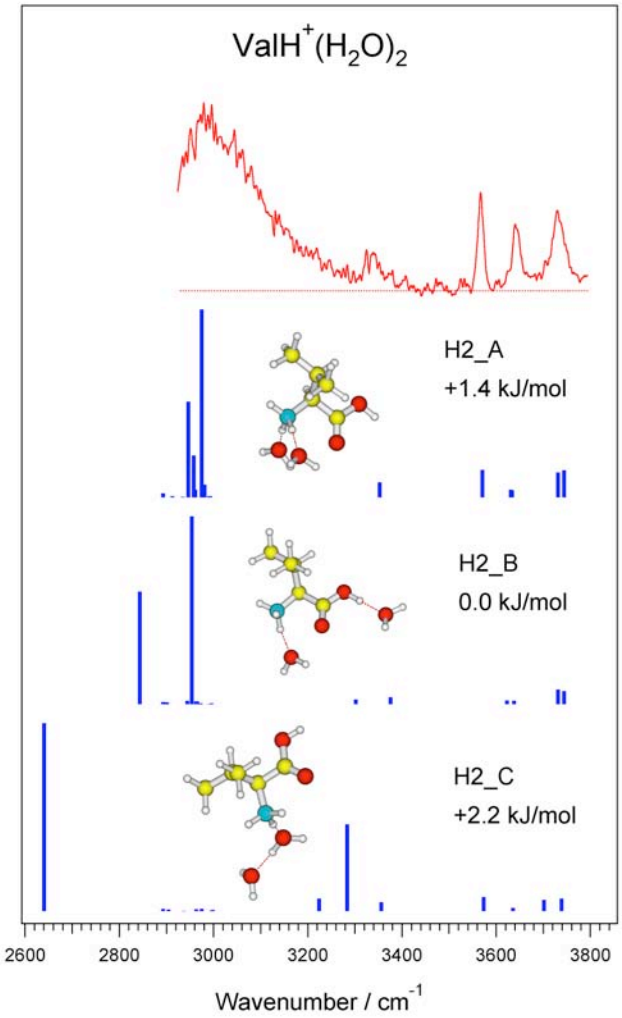

Fig. 3.7: Comparison of measured infrared spectra of Val•$H^+(H_2O)_2$ with calculated spectra corresponding to the structures shown.

In contrast to the conformers H2_B and H2_C discussed above, we find good agreement between the calculated IR spectrum of conformer H2_A and the experimental spectrum of $ValH^+•(H_2O)_2$. The good prediction of the position of the hydrogen bonded ammonium, slightly blue-shifted in comparison with $ValH^+•(H_2O)$, together with the decrease in intensity of the free ammonium NH stretch band over that of the hydrogen bonded ammonium are consistent with the presence of two hydrogen-bonded NH stretch and only one free NH stretch. Moreover, the free OH stretch water bands are almost doubled in intensity relative to the free COO-H compared to $ValH^+•(H_2O)$, which is consistent with the presence of twice the number of OH absorbing vibrations upon addition of a second water molecule. The fact that the water symmetric and antisymmetric stretch bands are close to that of free water, both in the measured spectrum and the calculated one for this conformer, indicates that neither of the water molecules acts as hydrogen bond donors.

3.3.4 $ValH^+•(H_2O)_3$

The infrared spectrum of $ValH^+•(H_2O)_3$ (*Fig. 3.2*) is similar to those of the smaller water clusters, albeit with several noticeable changes. The feature assigned to the non-hydrogen bonded ammonium decreases to the point where it is not obvious that it still appears, and the free COO-H band decreases in intensity relative to both the free water stretches and the broad hydrogen-bonded ammonium absorption. All the major features (hydrogen-bonded ammonium stretches, free COOH stretch and free water stretches) shift slightly to the blue compared to the smaller clusters.

As shown in *Fig. 3.8*, DFT calculations predict a minimum energy structure having one water hydrogen bonded to the carboxylic acid and two water molecules on the ammonium NH bonds (H3_B), whereas the other energetically competing structure (H3_C) contains two inner shell waters on the ammonium and the third in the outer shell acting as a double hydrogen-bond acceptor, forming a cyclic water structure. Surprisingly, the first low energy conformer hydrating the ammonium group with water molecules interacting with each of the NH bonds (H3_A) lies 11.5 kJ/mol higher in energy than the previously cited structures. Such an energy difference starts to be larger than the uncertainty of the calculations, suggesting that DFT predicts H3_A to be a higher energy conformer given the level of our calculation.

The free COO-H band, at 3571 cm^{-1} in the measured spectrum, rules out the exclusive presence of H3_B, although we cannot eliminate the possibility of a small contribution from this conformer. The calculated vibrational spectrum of H3_C exhibits characteristic absorptions of the H-bonded water OH stretches around 3500 cm^{-1}, which do not appear in the experimental spectrum. Moreover, the cyclic water structure would show a substantial red-shift of the H-bonded ammonium bands below 3000 cm^{-1}, which is not observed. Taken together, this allows us to rule out the contribution of such a conformer to our spectrum.

The spectrum of the higher energy conformer predicted by DFT (H3_A) seems to agree best with the experimental data. It reproduces well the free COOH band at 3571 cm^{-1} and it is consistent with the relative increase in intensity of the hydrogen-bonded ammonium bands and the free water bands that come with the increase in the number of oscillators.

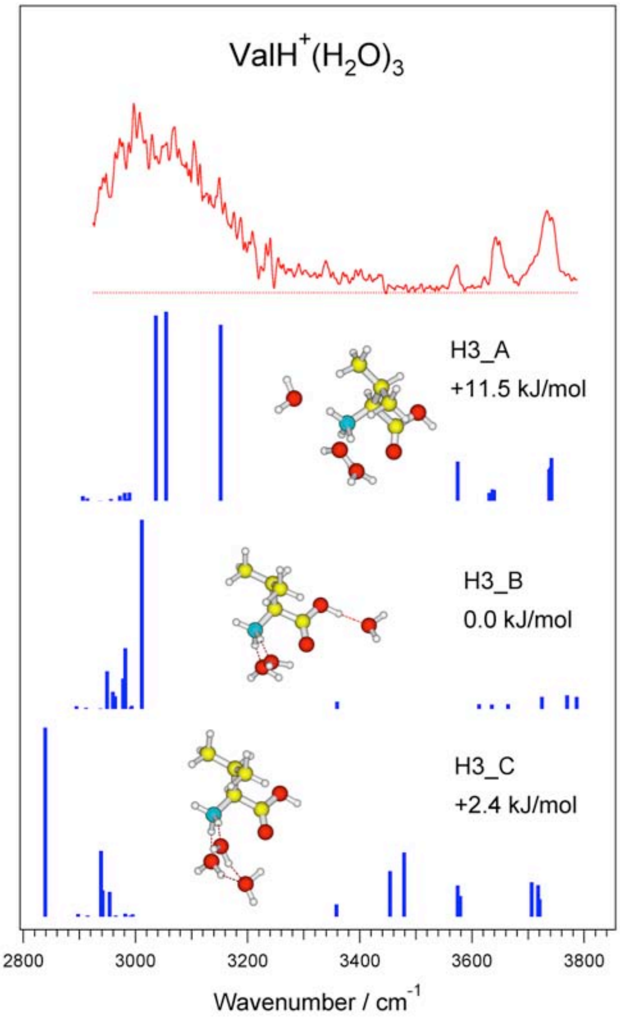

Fig. 3.8: Comparison of measured infrared spectra of Val•H$^+$(H2O)$_3$ with calculated spectra corresponding to the structures shown.

3.3.5 ValH$^+$•(H$_2$O)$_4$

While the infrared spectrum of ValH$^+$•(H$_2$O)$_4$ (*Fig. 3.9*) continues the general trend established by the smaller clusters (i.e., decreasing intensity of the carboxylic acid stretch, increasing intensity of the higher-frequency water stretch, and persistence of the broad, hydrogen-bonded ammonium band), some new bands begin to appear. A completely new feature appears at 3456 cm^{-1}, and a series of smaller peaks seem to grow in on its high-frequency side.

There are two things that seem clear from the measured IR spectrum: (1) the characteristic broad feature between 3000-3200 cm^{-1} implies that at least some of the water molecules remain attached to the ammonium group; and (2) the strong enhancement of the higher frequency free OH stretch band suggests that most of the water molecules have at least one donor hydrogen bond and one free OH stretch, the former being strongly shifted to lower wave number while the latter appears near the asymmetric stretch frequency of free water. It is difficult to draw any further conclusions from the observed spectrum without the help of calculations.

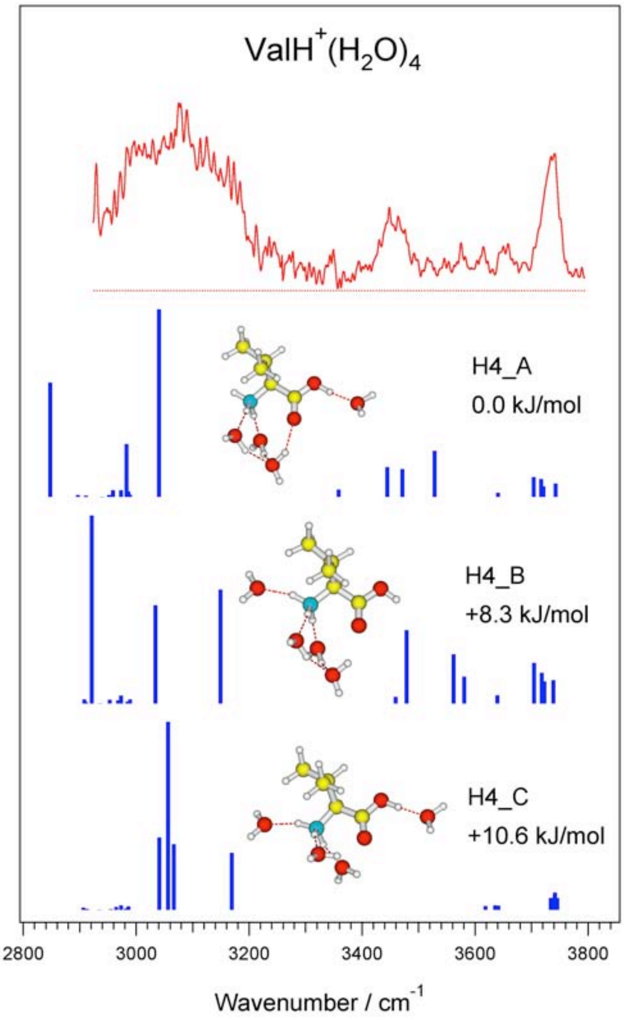

Fig. 3.9: Comparison of measured infrared spectra of Val•H$^+$(H2O)$_4$ with calculated spectra corresponding to the structures shown.

In lieu of performing an exhaustive conformational sampling of ValH$^+$•(H$_2$O)$_4$, we use our chemical intuition and calculate vibrational spectra of three candidate conformers based on the extensive search accomplished for ValH$^+$•(H$_2$O)$_3$. Starting from the dominant conformer H3_A of the tri-hydrated molecule, we add one water molecule near the carboxylic group to obtain a structure with all the available amino acid sites fully hydrated, shown as H4_C in the bottom panel of *Fig. 3.9*. Another logical starting point for stable structures of ValH$^+$•(H$_2$O)$_4$ is the conformer H3_C of the trihydrate, since this already contains water molecules that donate a hydrogen bond. We explore two conformers with H3_C parentage – one in which the additional water binds to the remaining free ammonium NH (H4_B), and the other to the carboxylic acid OH (H4_A). The relative energies of the three calculated structures are shown in *Fig. 3.9*.

The calculated spectrum of the conformer H4_C is clearly not consistent with its being the dominant conformer contributing to the measured spectrum, since no spectral features are predicted between 3200 and 3600 cm^{-1}. On the other hand, conformers H4_A and H4_B, which both contain cyclic water clusters, clearly show peaks in this region arising from water molecules that simultaneously donate and accept hydrogen bonds (AD). In addition, these structures show a strong high-frequency OH band arising from the dangling water OH bonds. While the calculated spectrum of H4_B shows better general agreement with the experimental data than H4_A, we cannot clearly distinguish between them. Moreover, because we have not performed an exhaustive search of the conformational space, we cannot rule out the existence of other structures that would be consistent with the measured spectrum. In particular, we cannot eliminate the possible existence of structural isomers where the cyclic water cluster is broken and the outer-shell water molecule interacts as an AD with one another in the inner-shell rather than as an AA.

3.4 INFRARED SPECTRA OF LITHIATED VALINE-WATER CLUSTERS

The properties of lithiated valine water clusters should be intrinsically different from those of the corresponding protonated species. In lithiated valine, the amino acid appears in its neutral form and the hydrated cluster of the amino acid derives its charge through coordination to the lithium ion. The neutral form of valine offers different possible sites for non-covalent interactions: the NH_2 group and the carboxylic OH may act both as a hydrogen-bond donor and acceptor, and the carbonyl oxygen as an acceptor. In addition, the lithium ion will play a major role in determining the arrangement of solvent, both by occupying potential hydrogen bonding sites on the valine backbone and by directly binding water molecules. Thus the lithium ion and the amino acid compete as potential solvation sites. The coordination number of lithium in gas phase water clusters is generally four [17-20], with the water molecules forming a tetrahedral structure around the metal ion in the first solvent shell. The attraction between the electronegative oxygen atoms of water and the lithium cation is about one order of magnitude stronger than hydrogen-bonding between water molecules [18], which would suggest that the first few water molecules added to lithiated valine will likely hydrate the alkali ion rather than a site on the amino acid or build up a second solvent shell.

3.4.1 ValLi$^+$•(H$_2$O)$_1$

The high frequency region of the ValLi$^+$•(H$_2$O) spectrum (*Fig. 3.10 (a)*) shows a strong resemblance to that of the corresponding protonated species (*Fig. 3.10 (b)*): it exhibits a strong absorption band at 3560 cm^{-1}, characteristic of a free carboxylic acid OH stretch, and two less intense peaks at 3649 cm^{-1} and 3731 cm^{-1}, characteristic of symmetric and antisymmetric OH stretches in the free water molecule. The only absorption that appears below 3500 cm^{-1} is a small band at 2979 cm^{-1}.

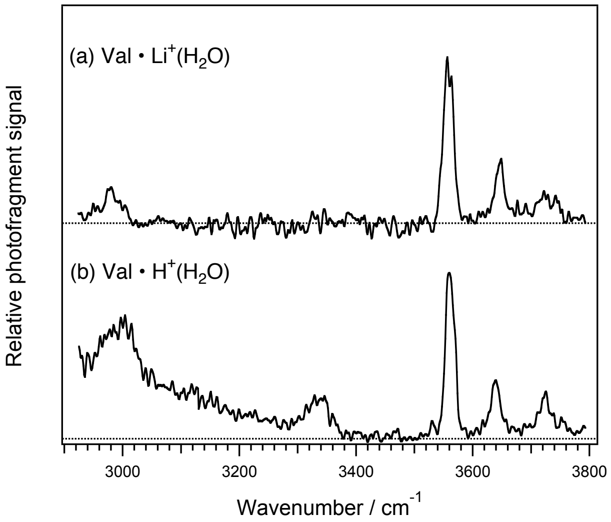

Fig. 3.10: Infrared photophragment spectra of (a) Val•Li$^+$(H$_2$O) and (b) Val•H$^+$(H$_2$O)

As in Val•H$^+$(H$_2$O) water clusters, the symmetric and antisymmetric water bands of Val•Li$^+$(H$_2$O) appear lower in frequency than in a free water molecule, with the lower frequency symmetric stretch band being the more intense. Similar spectroscopic signatures have been observed by Lisy and coworkers in the vibrational spectra of alkali ion water clusters [9] and were attributed to the electrostatic interaction between the lithium cation and water. This would suggest that the water is preferentially solvating the charge.

There seems to be no evidence in our spectra for the presence of either free N-H stretch bands, which would be expected to occur in the region 3200-3400 cm^{-1} based on the spectrum of neutral valine, [8] or hydrogen-bonded ammonium bands, which we observed in the protonated clusters in the region 3000-3200 cm^{-1}. The former is not surprising, since the symmetric and antisymmetric stretch vibrations of the neutral amino group are known to be extremely weak. [21] The latter, combined with the carboxylic OH stretch band at 3560 cm^{-1} suggests that valine does not exist in the zwitterionic form. The remaining band at 2979 cm^{-1} is likely to arise from CH stretch absorptions, which are hidden beneath the hydrogen-bonded ammonium bands in the protonated species.

We show representative calculated structures of $ValLi^+\bullet(H_2O)$ in *Fig. 3.11*.

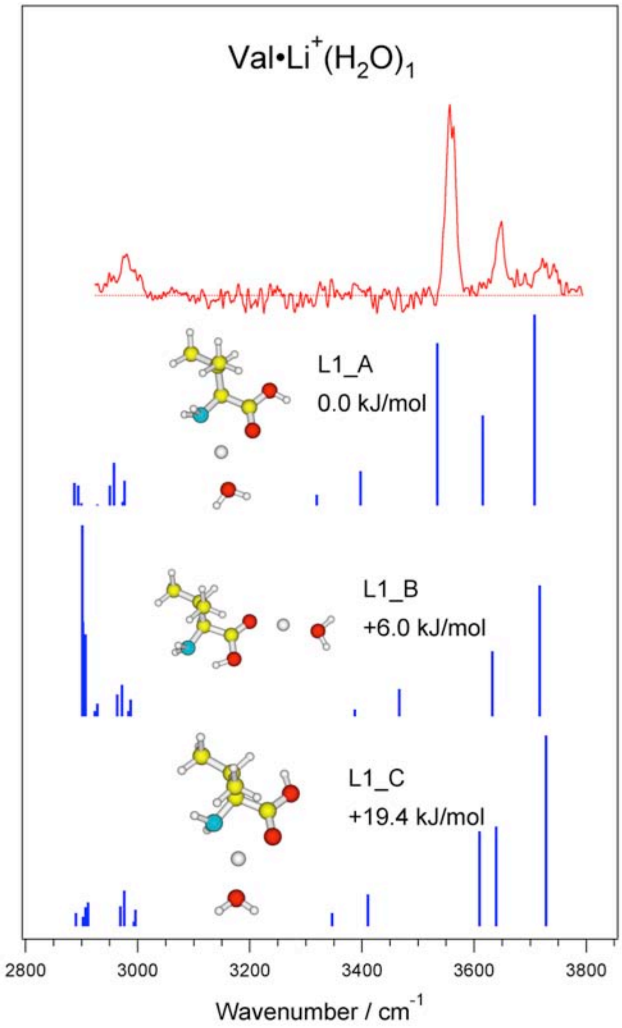

Fig. 3.11: Comparison of measured infrared spectra of $Val\bullet Li^+(H_2O)_1$ *with calculated spectra corresponding to the structures shown.*

The calculated frequencies of the lowest energy conformer, L1_A, show good agreement with the measured spectrum. In this cluster, the lithium is coordinated between the carbonyl oxygen and the amino nitrogen (NO coordinated), which is likely to stabilize the *syn* conformation of valine, and the water molecule solvates the lithium ion. This shows the predominance of electrostatic forces between the water dipole and the cation in the first step of hydration. L1_C is a higher energy conformer also with an NO-coordinated lithium, but differs from L1_A by the carboxylic OH bond in the *trans* position with respect to the carbonyl. This structural difference gives rise to a blue shift of the corresponding absorption band above 3600 cm^{-1}, which is not visible in our spectra, eliminating this conformer from our consideration.

L1_B is a representative conformation of OO-coordinated structures, with the lithium cation bound to the carboxylic group and the valine adopting an *anti* conformation stabilized through intramolecular hydrogen-bonding between the carboxylic OH and the amino group. The latter shifts the COO-H stretch to the red edge of the spectrum, below 2900 cm^{-1}, making it inconsistent with the measured spectrum, which shows clear evidence for a COO-H stretch absorption at 3560 cm^{-1}. It follows that valine is not present in its zwitterionic form in ValLi^{+}•(H_2O), since this would imply the disappearance of the COO-H vibration.

3.4.2 ValLi^{+}•(H_2O)$_2$

The spectrum of Val•Li^{+}(H_2O)$_2$ is similar to that of Val•Li^{+}(H_2O) – it exhibits bands at 3656 and 3738 cm^{-1}, slightly blue shifted from the previously assigned free water O-H bands in Val•Li^{+}(H_2O). In place of the typically strong COO-H vibration, there appears a weaker and blue-shifted band at 3569 cm^{-1}. While this may be interpreted as the carboxylic acid OH stretch, as discussed below, it is also possible that this arises from a weakly hydrogen-bonded OH water stretch. It is difficult to assign this band without the help of calculated spectra, which we show in *Fig. 3.12*.

Calculations predict that the lowest energy structure (L2_C) of Val•Li^{+}(H_2O)$_2$ has valine in the zwitterionic form. In this structure, the carboxylic acid proton resides on the amino group, and the lithium cation is solvated by the carboxylate group, forming a salt bridge with the zwitterion. In this OO-coordinated structure, one of the water molecules exclusively solvates the metal ion, whereas the second water establishes a hydrogen-bond with one oxygen of the carboxylate, resulting in a substantial red-shift of the water O-H vibration to about 3300 cm^{-1}. The vibrational band appearing at 3569 cm^{-1} in the observed spectrum, indicative of a free COO-H stretch, together with the lack of spectral features observed in the region 3300-3400 cm^{-1}, seems to rule out the existence of an OO-coordinated zwitterionic structure.

The energetically competitive non-zwitterionic (NZ) OO-coordinated structure (L2_B) differs from the zwitterionic form (L2_C) only by the position of the proton on the carboxylic group characteristic of the neutral form. This minor difference substantially affects the appearance of the spectrum. The donating water hydrogen bond orients the proton of the carboxylic acid towards the amino group, which favors an intramolecular hydrogen bonded bridge HOH→O-H(COO-H)→ NH_2. Such a geometry gives rise to a H-bonded O-H vibration of the donor water around 3600 cm^{-1} and to a red-shift of the COO-H to 2864 cm^{-1}. The experimental spectrum of ValLi^{+}•(H$_2$O)$_2$ cannot rule out the presence of such a structure: the band at 3570 cm^{-1} previously assigned to a free COO-H stretch could be assigned here to the hydrogen-bonded OH of water. The lack of data below 2900 cm^{-1} does not allow us to observe an intramolecular hydrogen-bonded COO-H band, although the broadening of the band around 3000 cm^{-1} might suggest a beginning of such a band.

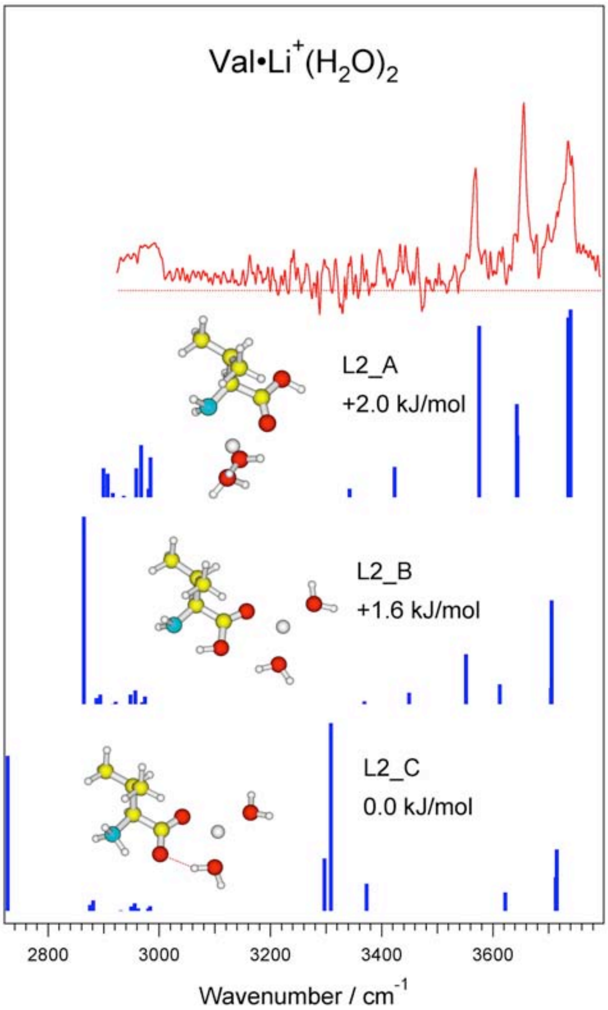

Fig. 3.12: Comparison of measured infrared spectra of Val•Li^{+}(H$_2$O)$_2$ with calculated spectra corresponding to the structures shown.

The NO-coordinated cluster (L2_A) has a similar structure to the most stable conformer of the monohydrated cluster, with a second water molecule bound to the lithium cation providing a four-coordinated shell around the ion. The calculated spectrum corresponding to this structure is in good agreement with the experimental data of ValLi^{+}•(H$_2$O)$_2$. The observed blue shift in frequency of the free COO-H stretch at 3569 cm^{-1} with respect to the monohydrated cluster is in qualitative accord with the shift predicted by calculations. The water bands at 3656 and 3736 cm^{-1} are blue-shifted in comparison with the monohydrated complex, which is well reproduced by calculations and indicates that the presence of second water molecule slightly weakens the electrostatic interaction with the lithium ion.

We thus conclude that the spectrum of ValH^{+}•$(H_2O)_2$ is consistent with two possible charge solvated structures, where the lithium cation is either NO-coordinated (L2_A) or OO-coordinated (L2_B) to neutral valine. There is no experimental evidence to support a salt-bridge OO-coordinated conformation (L2_C).

3.4.3 ValLi^{+}•$(H_2O)_3$

The observed infrared spectrum of ValLi^{+}•$(H_2O)_3$ (*Fig. 3.13*) is substantially different from that of ValLi^{+}•$(H_2O)_{1\text{-}2}$. The free COO-H stretch absorption disappears and the relative intensities of the two free water O-H stretches at 3659 cm^{-1} and 3738 cm^{-1} are reversed, with the anti-symmetric stretch band more intense than the symmetric stretch. These bands are slightly blue-shifted from their position in the spectrum of ValLi^{+}•$(H_2O)_2$, suggesting a weakened ion-dipole interaction probably originating from the presence of an additional water molecule around the metal ion. New bands arise at 3444 and 3619 cm^{-1}, and the CH stretch absorption band at 2980 cm^{-1} gains in relative intensity.

The calculated minimum energy conformation (L3_D) exhibits NO coordination of the lithium cation surrounded by two inner shell water molecules bonded to an outer shell water (AA), forming a cyclic structure. The disappearance of the free COO-H absorption from the spectrum clearly contradicts the possible occurrence of such a conformer. Moreover the hydrogen-bonded O-H stretch bands of the two inner-shell water molecules, which are predicted by calculations to occur around 3500-3600 cm^{-1}, do not appear in the measured spectrum.

The lowest energy zwitterionic structure (L3_E) differs only by 0.1 kJ/mol from the minimum energy structure (L3_D). In such a conformation, the lithium is OO-coordinated and surrounded by two water molecules, one of which donates a hydrogen to the carboxylate group, and the third water hydrates the ammonium group. The spectrum corresponding to L3_E is consistent with the observed disappearance of the COO-H stretch, but it cannot account for the appearance of bands at 3619 cm^{-1} and 3444 cm^{-1}. Moreover, the observed spectrum shows no sign of the hydrogen-bonded ammonium bands in the 3000 cm^{-1} region that were so prominent in the spectra of the ValH^{+}•$(H_2O)_n$ clusters. An alternative zwitterionic structure (L3_F) in which the third water fills the first solvent shell of Li^{+} rather than hydrating the ammonium group of valine is energetically competitive, but there seems to be no feature in the observed spectrum that corresponds to the strong hydrogen bonded

OH water stretch predicted to appear at 3310 cm^{-1}. Thus, the experimental data are not consistent with the calculated spectra for the two salt-bridge structures, even though they are predicted to be among the most stable. We therefore need to examine higher energy conformers.

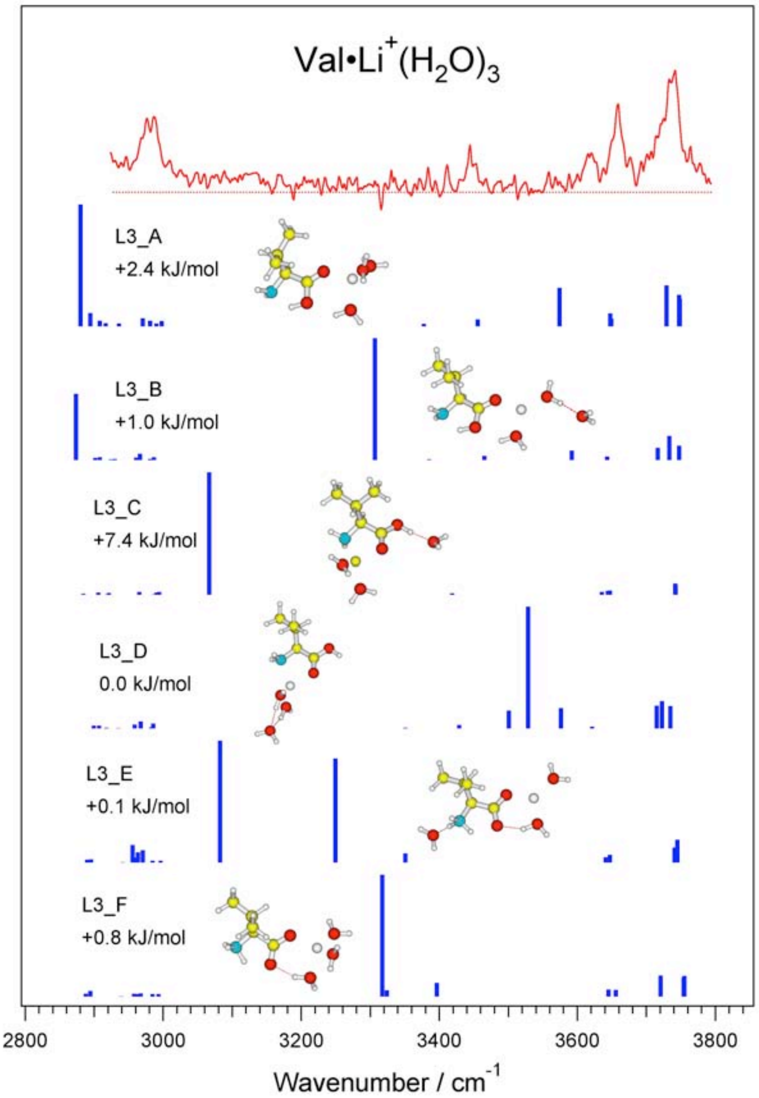

Fig. 3.13: Comparison of measured infrared spectra of Val•Li$^+$(H$_2$O)$_3$ with calculated spectra corresponding to the structures shown.

Only one low-energy structure (L3_C) exhibits NO-coordination of the lithium ion. This conformer derives from L2_A, one of the two dominant conformers contributing to the spectrum of ValLi$^+$•(H$_2$O)$_2$, with the third water molecule hydrogen bonded to the carboxylic acid OH. While this interaction will shift the COO-H stretch away from the 3600 cm^{-1} region, consistent with the observed spectrum, we do not observe the intense, shifted band in the region of 3100 cm^{-1} where it is predicted to occur. All other stable conformers derive from the OO-coordinated conformer L2_B identified in the doubly hydrated cluster. The most stable among these conformers (L3_B) possesses an outer-shell water molecule that would give rise to an intense band around 3300 cm^{-1}, contrary to the observed spectrum. Finally, the OO-coordinated conformer (L3_A), possessing a complete first solvent shell around Li$^+$ with three water molecules, seems to agree best with the experimental spectrum. The hydrogen-bonded water bridging the carboxylic acid is consistent with the absorption band at 3619 cm^{-1} and the NH stretches calculated around 3400 cm^{-1} can account for the observed band at 3444 cm^{-1}. Furthermore, the presence of two free water molecules correlates with the high frequency absorption bands in the measured spectrum.

3.4.4 ValLi$^+$•(H$_2$O)$_4$

The spectrum of ValLi$^+$•(H$_2$O)$_4$ (see *Fig. 3.3 (d)*) shows evidence for two main absorption bands, one above 3700 cm^{-1} characteristic of a free O-H band, and the other centered at 3450 cm^{-1}, which may be due to hydrogen-bonded stretches of AD water molecules. The breadth of these bands suggests the presence of many transitions falling within the same band. The disappearance or very weak contribution of the symmetric O-H stretch implies the loss of free water O-H stretches which would result from the formation of a second solvent shell. The spectral features from 3400 to 3800 cm^{-1} are remarkably similar to those of ValH$^+$•(H$_2$O)$_4$ (*Fig. 3.15*). By analogy with protonated valine clusters (*Fig. 3.9*), we might assume that a cyclic structure forms with two AD waters bound to a terminating AA water, giving rise to the absorption bands between 3400 and 3560 cm^{-1}. The strong and narrower absorption band of the free OH stretches at 3738 cm^{-1} corroborates the formation of such a symmetric H-bonded structure.

3.5 DISCUSSION

Having looked in some detail at our measured infrared spectra and compared them with calculations of spectra for different structures, we present here an overview of the solvation process for both the protonated and lithiated valine-water clusters. It is clear that at the level of B3LYP/6-31++G**, the predicted lowest energy structures do not always have a spectrum that best corresponds to what we measure – it is often the case that the spectra of slightly higher energy structures agree much better. While this should not be surprising given the general uncertainties in the calculated energies, there can be systematic biases to the calculated results. In particular, the stabilization arising from hydrogen bonding to the carboxylic OH seems to be systematically overestimated with respect to putting a second water molecule on a protonated ammonium. Nevertheless, the calculations provide invaluable guidance in predicting the spectrum that would correspond to a particular structure. While the intensities of the bands do not seem to be particularly well predicted, where we have clear assignments of the observed bands, the calculated band positions correspond well to what we observe. The calculations also seem to predict the disappearance of high frequency stretch bands that are red-shifted outside the frequency range of our spectra upon hydrogen bonding with water as well as more subtle blue-shifts of free water OH bands upon addition of water to the same charge site. In our discussion below, we use the structures that agree best with the observed spectra to interpret the stepwise solvation of protonated and lithiated valine-water clusters.

The data shown in *Figs. 5-13*, together with the calculated structures and spectra, suggest that the solvation process is driven by the charged group in preference to hydrogen bonding sites on the amino acid. We show this schematically in *Fig. 3.14*.

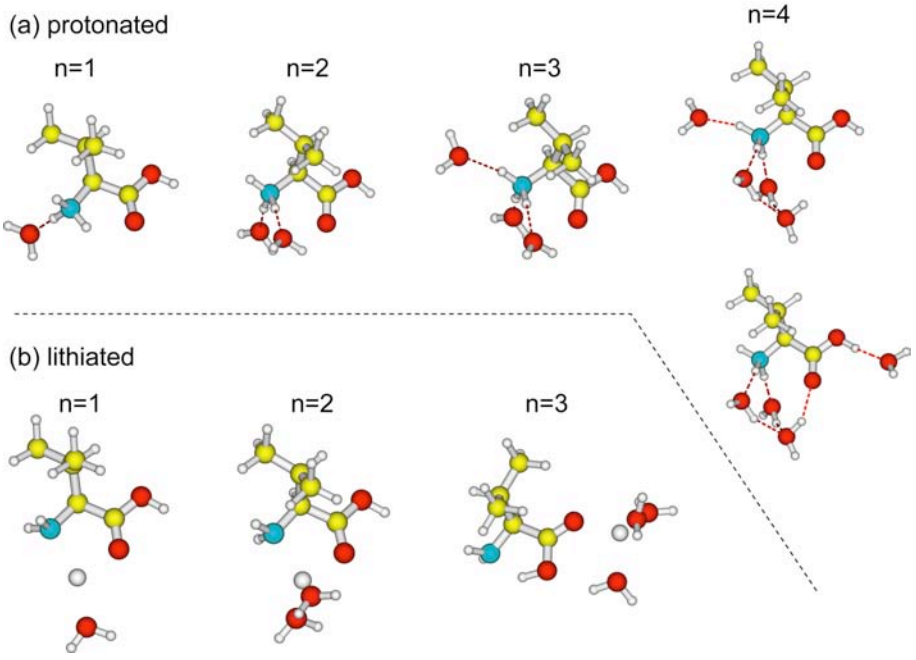

Fig. 3.14: Overview of the solvation process in both the protonated and lithiated valine.

For the protonated species, the first 3 water molecules seem to preferentially bind to the protonated ammonium. In the case of the 4th water molecule, we cannot clearly distinguish between two structures. In both cases, there seems to be a second solvation shell being formed in which one water molecule binds to two others that are bound to the ammonium. In the lowest energy structure, the remaining water molecule is bound to carboxylic acid OH, while in a higher energy structure, that water is bound to the ammonium. Our experience tells us that the calculations overestimate the stabilization due to hydrogen bonding on the carboxylic site, and our intuition tells us that solvation of the ammonium should be preferred. This being the case, the overall picture is that solvation takes place at the charge site until the first solvation shell is filled, and then water begins to form a second shell, binding to other waters rather than to sites on the amino acid backbone.

In the case of the lithiated species, the situation is similar – solvation occurs preferentially at the lithium ion for the addition of the first 3 water molecules. While we do not have calculated spectra for the Val•Li$^+$(H_2O)$_4$, the strong resemblance with the spectrum of the corresponding protonated species suggests that a similar extended water structure is formed. This can be seen most clearly in *Fig. 3.15*, where the correspondence between almost every feature in the range 3450 – 3750 cm^{-1}, where we expect hydrogen bonded water bands to occur, is striking.

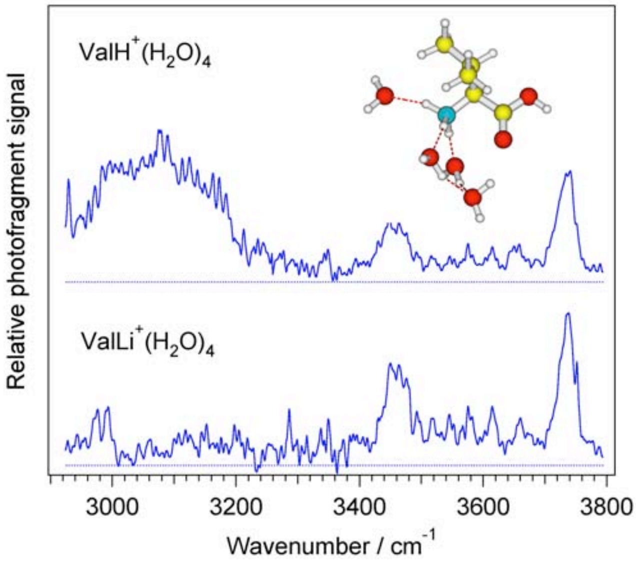

Fig. 3.15: Comparison of the quadruply hydrated protonated and lithiated species.

Given the similarity of the solvation process for protonated and lithiated valine, we might expect to see similar trends in other amino acids with uncharged side chains, as polar groups do not seem to compete with solvation of the charge or with water itself. Indeed, in spectra that we have measured for protonated tryptophan, the indole N-H stretch shows no sign of hydrogen bonding.

An interesting feature of the solvation process in the lithiated species is the apparent change in amino acid backbone conformation upon addition of the third water molecule – from the *syn* to the *anti* configuration. For Val•Li$^+$(H_2O)$_2$, calculations predict that the two conformers have roughly equal energy, although the spectrum agrees slightly better with the *syn* configuration. For Val•Li$^+$(H_2O)$_3$, the spectrum clearly points to the *anti* configuration for the amino acid backbone, which is stabilized by the interaction of the carboxylic OH with the lone pair on the amine nitrogen.

This difference in amino acid backbone conformation between Val•$Li^+(H_2O)_2$ and Val•$Li^+(H_2O)_3$ and the associated change in lithium ion location from NO coordination to OO coordination is consistent with conclusions from the BIRD studies of Williams and coworkers [5, 7]. In these studies, the change in the mode of metal ion binding from NO to OO coordination was deduced from both the dissociation kinetics as well as water binding energies to these two species in comparison to model compounds known to exist in zwitterionic or non-zwitterionic forms. These results were more consistent with a zwitterion form of valine with three water molecules. A similar change in the mode of metal ion binding occurs for both sodiated glycine and valine upon the addition of a second water molecule, although the forms of the amino acids in these clusters could not be identified based on the water binding energies [2, 7]. In contrast, the results presented here, which probe more directly the structure of the solvated species, show no sign of zwitterion formation in lithiated valine with the addition of up to four water molecules.

The discrepancy between conclusions drawn from the BIRD vs. IR spectroscopy experiments for the Val•$Li^+(H_2O)_3$ structure could be due to a number of reasons. It is the increasing difficulty to draw structural conclusions from water binding energies with increasing hydration extent due to the smaller differences in water binding energies between different structures. With BIRD, structural information is inferred from these small differences and from measurements of model compounds with known structure. An excellent reference structure is available for the NO coordinated form of Val•$Li^+(H_2O)_3$ and the change in metal ion binding between the clusters with two vs. three water molecules is clearly indicated from the results of both experiments. There are no suitable reference structures for the zwitterionic form of Val•$Li^+(H_2O)_3$ and a zwitterionic structure was inferred as the most likely reason for the higher water binding energy for Val•$Li^+(H_2O)_3$ vs. the nonzwitterionic and zwitterionic model compounds that had different modes of water binding. The IR spectroscopy experiments probe the structures of these hydrates more directly and should provide more reliable information in cases where suitable reference structures are not available. It is also possible that the structure of this ion differs in the two experiments. The ion structure may depend on how these ions are formed (condensation of water on bare ions vs. solvent evaporation of more extensively hydrated droplets) [22], the internal energy of the clusters, or the time scale of the experiments. The latter two factors are clearly very different in these two experiments and the primary way in which these ions are formed could be as well.

The major difference between the hydration of protonated valine and hydration of lithiated valine comes from the conformation change of valine in lithiated valine into an *anti* conformation. Both bare protonated and lithiated valine show a conformational preference for *syn* structures. Hydration of protonated valine does not seem to affect the *syn* conformation of the amino acid apart from sterical effects of water on the side chain residue. The presence of the lithium ion, on the contrary dictates a conformational change of the amino acid in the presence of water, and clearly shows the fundamental difference between lithiated valine and protonated valine water clusters and how the presence of either the neutral form of valine in the clusters or its protonated form may affect the conformational preferences of the amino acid induced by hydration.

References

1. Rodgers, M. T. and Armentrout, P. B., Acc. Chem. Res. (2004), 37, 989-998.
2. Ye, S. J., Moision, R. M., and Armentrout, P. B., Int. J. Mass Spectrom. (2005), 240, 233-248.
3. Jockusch, R. A., Lemoff, A. S., and Williams, E. R., J. Am. Chem. Soc. (2001), 123, 12255-12265.
4. Lemoff, A. S., Bush, M. F., and Williams, E. R., J. Am. Chem. Soc. (2003), 125, 13576-13584.
5. Lemoff, A. S. and Williams, E. R., J. Am. Soc. Mass Spectrom. (2004), 15, 1014-1024.
6. Ai, H., Bu, Y., and Han, K., J. Chem. Phys. (2003), 118, 10973-10985.
7. Jockusch, R. A., Lemoff, A. S., and Williams, E. R., J. Phys. Chem. A (2001), 105, 10929-10942.
8. Stepanian, S. G., Reva, I. D., Radchenko, E. D., and Adamowicz, L., J. Phys. Chem. A (1999), 103, 4404-4412.
9. Vaden, T. D., Weinheimer, C. J., and Lisy, J. M., J. Chem. Phys. (2004), 121, 3102-3107.
10. Weinheimer, C. J. and Lisy, J. M., J. Chem. Phys. (1996), 105, 2938-2941.
11. Kim, K. Y., Chang, H. C., Lee, Y. T., Cho, U. I., and Boo, D. W., J. Phys. Chem. A (2003), 107, 5007-5013.
12. Wang, Y. S., Chang, H. C., Jiang, J. C., Lin, S. H., Lee, Y. T., and Chang, H. C., J. Am. Chem. Soc. (1998), 120, 8777-8788.
13. Snoek, L. C., Kroemer, R. T., Hockridge, M. R., and Simons, J. P., Phys. Chem. Chem. Phys. (2001), 3, 1819-1826.
14. Herzberg, G., Molecular Spectra and Molecular Structure II. Infrared Raman Spectra of Polyatomic Molecules, ed. V.N. Reinhold. 1945, New York.
15. Macleod, N. A. and Simons, J. P., Phys. Chem. Chem. Phys. (2004), 6, 2821-2826.
16. Zwier, T. S., J. Phys. Chem. A (2001), 105, 8827-8839.
17. Loeffler, H. H. and Rode, B. M., J. Chem. Phys. (2002), 117, 110-117.
18. Lyubartsev, A. P., Laasonen, K., and Laaksonen, A., J. Chem. Phys. (2001), 114, 3120-3126.
19. Dzidic, I. and Kebarle, P., J. Phys. Chem. (1970), 74, 1466-1474.
20. Rodgers, M. T. and Armentrout, P. B., J. Phys. Chem. A (1997), 101, 2614-2625.
21. Carney, J. R. and Zwier, T. S., J. Phys. Chem. A (2000), 104, 8677-8688.
22. Rodriguez-Cruz, S. E., Klassen, J. S., and Williams, E. R., J. Am. Soc. Mass Spectrom. (1999), 10, 958-968.

Chapter 4

INFRARED PHOTOFRAGMENT SPECTROSCOPY OF PROTONATED TRYPTOPHAN WATER CLUSTERS

More than a decade after the first identification of six distinct conformers of bare tryptophan in a free jet expansion by Rizzo *et al*. [1, 2], the conformational preferences of the neutral amino acid in the gas phase have been elucidated by Snoek *et al*. [3] using a conformational selective 'hole-burning' spectroscopy and ab initio calculations and by Compagnon *et al*. [4] based on deflection measurements. These results, together with the pioneering work of Peteanu and Levy [5], motivated subsequent structural investigations of tryptophan water clusters in the gas phase [6] to address the question of zwitterion formation and how it can be triggered by the solvent environment.

Despite the great interest devoted to neutral amino acids, valuable information can also be inferred from investigations of the corresponding protonated species in the gas phase. In fact, the predominant form of many molecules of biological importance in aqueous solution is that of a closed shell molecular ion. The first studies on protonated tryptophan isolated in the gas phase have only been reported over the last couple of years [7-10]. Besides the theoretical work of Weinkauf and coworkers [9], which discusses the conformational preferences of protonated tryptophan, no structural investigations of the corresponding hydrated species have been reported. By probing water clusters of protonated tryptophan in the gas phase, we also investigate the influence of solvent on the amino acid structure. The information obtained on the protonated hydrates should represent a step forward in understanding how gas- and solution-phase structures relate.

Weinkauf and coworkers [9] have shown that the lowest energy conformer of bare protonated tryptophan exhibits a charged ammonium group in lieu of the neutral amine. The addition of the proton results in a conformational rearrangement of the most stable structure of neutral tryptophan proposed by Snoek *et al.* [6], where the stabilization provided by intramolecular hydrogen-bonding between the carboxylic acid and the amine (COO-H···NH_2) is substituted in the protonated species by a weak hydrogen-bonding interaction of the proton with the π electron cloud of the indole ring.

In the previous discussion about the conformational preferences of protonated valine in the Val•$H^+(H_2O)_{1\text{-}4}$ hydrates (cf. *§ 3.3*), we have set the scene for structural investigations of slightly more complex water clusters of amino acids such as those of protonated tryptophan. Valine is one of the simplest amino acids. Its isopropyl residue does not play a predominant role in the hydration process of the amino acid as seen in (cf. *Chapter 3*), leaving the protonated amino group and the carboxylic acid, as the only possible sites of interaction with a water molecule. We have shown in this simple case that hydration primarily affects the ammonium group. In addition to the carboxylic acid and the amino functional groups, tryptophan offers an additional hydration site in the residue with the indole N-H (in the pyrrole ring). The electron density of the aromatic ring can also provide stabilization of the charged ammonium group. Such a variety in the type of interactions with water and in the number of binding sites makes one foresee the difficulty of disentangling the competing interactions in the hydration process.

Since tryptophan and valine only differ by the nature of the residue comparison of the spectra of Trp•$H^+(H_2O)_n$ and Val•$H^+(H_2O)_n$ should elucidate the role played by the residue in the organization of the solvent shell around the amino acid ion core. On the other hand, the vibrational signatures of water clusters of protonated tryptamine shed light on the interaction of water with an ammonium group in the presence of an indole ring. Useful information can be deduced on the possible competition of the indole NH with other binding sites of water but also on the role of the carboxylic group upon hydration of protonated tryptophan.

In light of this, the following interpretation of the spectra of protonated tryptophan water clusters relies essentially on the comparison with the data obtained for valine and tryptamine, while calculations (cf. *§ 2.4.3*) have been performed to support some of the structural assignments. In this section we will refer to the different structures calculated for Trp•$H^+(H_2O)_n$ using the amino acid abbreviation (Trp) followed by a number indicating the number of water molecules in the hydrate and by a letter distinguishing between different conformers. For example, Trp3_A indicates conformer A of the trihydrate of protonated tryptophan.

4.1 PROTONATED TRYPTOPHAN WATER CLUSTERS Trp•$H^+(H_2O)_n$

The vibrational spectra of protonated tryptophan water clusters (Trp•$H^+(H_2O)_{1-4}$) obtained in our photofragment spectrometer are shown in *Fig. 4.1*. The spectra are characterized by sharp features in the high-energy range (3400 - 3800 cm^{-1}) and broad, intense absorption bands at lower energies (below 3400 cm^{-1}), similar to the spectra of protonated valine water clusters (cf. *§ 3.3*). Clear spectral changes arise upon addition of water molecules, which we discuss below, for each degree of hydration.

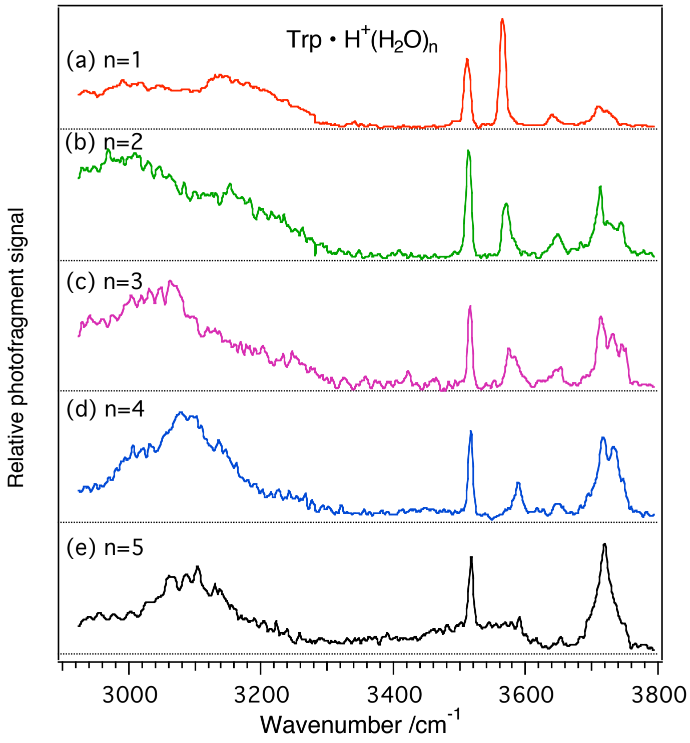

Fig. 4.1: Infrared photofragment spectra of Trp•$H^+(H_2O)_{1-5}$

Before going into detail in the interpretation of the experimental spectra of protonated tryptophan water clusters, we first comment on the calculated vibrational spectra of the bare ion. The latter reveals important features that facilitate the comprehension of vibrational signatures observed in the spectra of the hydrated species.

4.2 Trp•H^+

As already known from the conformational preferences of neutral tryptophan [3, 6] the alkyl chain of the amino acid is flexible enough to fold back over the indole ring and become stabilized by weak H-bonding interactions with the indole ring. This conformational characteristic is also retained in the protonated amino acid, which is not surprising since the interaction with the π-electron cloud offers a stabilization of the charged amino group. The spectra of the lowest-energy structures calculated for bare Trp•H$^+$ (*Fig. 4.2*) all exhibit one band in the free N-H stretch region above 3300 cm^{-1} and two red-shifted bands between 3000 cm^{-1} and 3200 cm^{-1}, indicating a weak interaction with the carbonyl oxygen (N-H···O=C) for the higher-energy one and with the π electron cloud (NH···π) for the most red-shifted one.

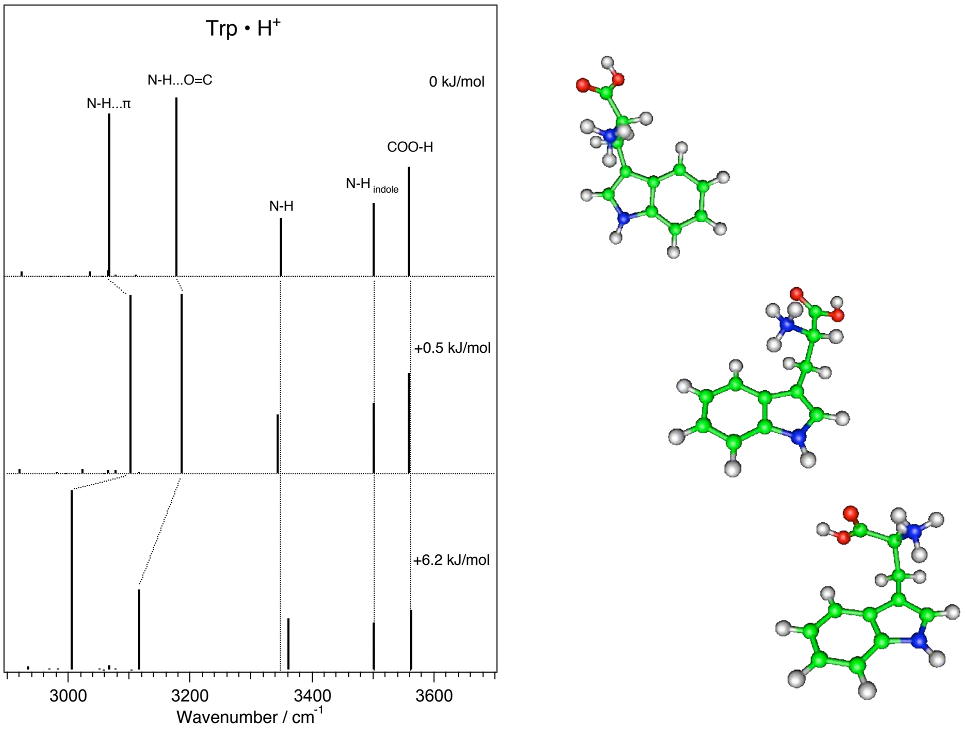

Fig. 4.2: Calculated spectra for different conformers of Trp•H$^+$

A similar flexibility of the alkyl chain has been observed for neutral tryptamine [11, 12]. Our calculations of TRA•H$^+$ vibrational frequencies (*Fig. 4.3*) predict a weak interaction of one of the ammonium stretches with the π electron cloud (at ~ 3100 cm^{-1}) like in protonated tryptophan. Note that in both of the bare ions, C-H stretch absorptions of the alkyl side chain are predicted between 2900 – 3000 cm^{-1}, those of the indole ring between 3000 – 3150 cm^{-1} and the indole N-H vibration at 3500 – 3510 cm^{-1}. For protonated tryptophan, the additional COO-H stretch absorption appears at 3560 cm^{-1}.

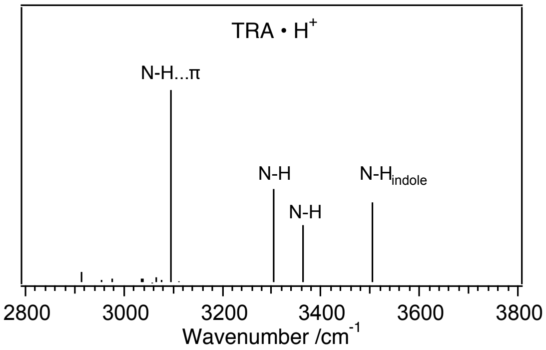

Fig. 4.3: Calculated spectrum of TRA•H$^+$

4.3 TRP•H$^+$(H_2O)

The spectrum of Trp•H$^+$(H_2O) (*Fig. 4.4*) is characterized at high frequency by two strong absorptions at 3511 and 3565 cm^{-1} and by two weaker bands centered at 3640 and 3712 cm^{-1}. In the low frequency range we distinguish a weak absorption at ~ 3340 cm^{-1} and an intense and broad feature below 3300 cm^{-1}, revealing a sub-structure likely suggesting an overlap of multiple vibrations.

We assign the bands at 3511 and 3565 cm^{-1} to a free indole N-H and a free carboxylic COO-H respectively, based on the comparison with the spectrum of TRA•H$^+$(H_2O) but also with those of Val•H$^+$(H_2O) and Val•Li$^+$(H_2O) as discussed earlier in *§3.3.2*. Recall that the spectrum of each amino acid monohydrate contains a characteristic band around 3560 cm^{-1}, which disappears in the spectrum of the tryptamine monohydrate, since the latter does not possess a carboxylic acid. On the other hand, tryptophan and tryptamine both have in common an absorption band at ~3510 cm^{-1} originating from the indole N-H vibration. Calculations of the corresponding vibrational spectra corroborate these assignments. The weaker bands centered at 3712 and 3640 cm^{-1} are characteristic of free anti-symmetric and symmetric OH stretches of an acceptor water, as already observed in the spectra of Val•Li$^+$(H_2O) and Val•H$^+$(H_2O).

Thus, the presence of a free indole N-H and a free COO-H in the experimental spectrum, eliminate the possibility of water binding to either of these sites and leave the ammonium group as the only prospective hydration site in the molecule. An interaction of water with the carbonyl oxygen is not likely, since water exhibits two free O-H stretches, implying that the molecule acts as a hydrogen-bond acceptor with its oxygen lone pair.

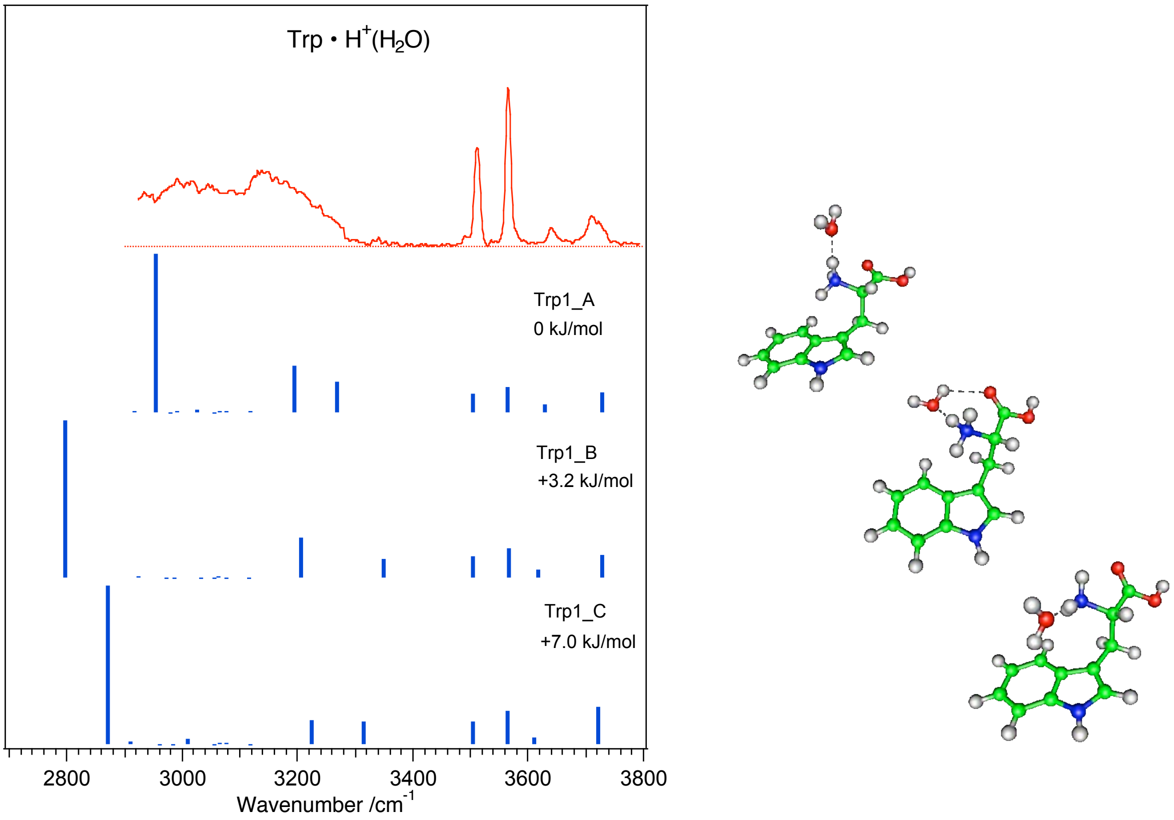

Fig. 4.4: Comparison of measured infrared spectra of Trp•H$^+$(H$_2$O) with calculated spectra corresponding to the structures shown.

The features in the low-energy range bear some similarity with those observed in the monohydrate of protonated valine and seem to support evidence for an interaction of water with the ammonium group. We observe experimentally only a weak band at 3342 cm^{-1} indicating free N-H stretch absorption. The broad and intense bands centered around 3030 and 3150 cm^{-1} presumably arise from hydrogen-bonding of N-H vibrations overlapping with the alkyl and aromatic C-H stretches absorbing in this region.

In light of the observations made for bare protonated tryptophan, where intramolecular interactions have been evidenced, we calculate three conformers of the corresponding monohydrate, exploring three different binding modes of water as depicted in *Fig. 4.4*. In conformer Trp1_A, two N-H stretches are involved in intramolecular interactions either with the indole ring or with the carbonyl and the remaining one is hydrogen-bonded to water. In conformer Trp1_B, the water molecule binds to the N-H pointing towards the carbonyl, while in conformer Trp1_C the weak NH···π interaction is substituted with an NH···OH$_2$···π interaction, where the water hydrogen-bonded to the ammonium ion further interacts with the indole ring.

The calculated spectrum of conformer Trp1_A seems to agree best with the experimental spectrum. We assign the broad feature centered at ~ 3030 cm^{-1} in the latter to the ammonium N-H hydrogen-bonded to water and the one at ~ 3150 cm^{-1} is attributed to the NH interacting with the indole ring as observed for the bare molecular ion. The remaining N-H gives rise to the weak band observed at ~ 3340 cm^{-1}, which may also be involved in a much weaker interaction with the carbonyl.

In conformer Trp1_B, binding of water to the ammonium stretch pointing to the carbonyl results in an N-H vibration shifted to ~ 2800 cm^{-1} upon hydrogen bonding, i.e., out of the experimental frequency range. Moreover the free water symmetric stretch is predicted at lower frequency in this conformer than that predicted in Trp1_A, likely suggesting a small interaction of water with the carbonyl in Trp1_B. Such a red-shift increases the discrepancy between the experimental band observed at ~ 3640 cm^{-1} and the band predicted by calculations. The predicted bands in the low energy end of the spectrum cannot account for the absorption features experimentally observed around 3000 cm^{-1}. This conformer is clearly not the dominant structure observed in the experimental spectrum.

In conformer Trp1_C, the vibrational frequency of the N-H stretch hydrogen-bonded to water is also predicted out of the experimental spectral range, while the two remaining N-H vibrations are predicted above 3200 cm^{-1}. The lack of strong absorption bands in the 2900-3000 cm^{-1} (beyond the expected weaker C-H stretches) is inconsistent with the absorption bands observed experimentally. Moreover, the interaction of water with the indole ring favored in Trp1_C is characterized by a noticeable red-shift of the O-H frequency predicted at 3610 cm^{-1}, contrasting with the experimental band at ~ 3640 cm^{-1}. Thus, there is no strong experimental evidence for an important contribution of Trp1_C in the spectrum.

Further evidence for the existence of intramolecular interactions between the ammonium vibrations and the indole ring or the carbonyl oxygen relies on the comparison of the spectrum of Trp•H$^+$(H_2O) with that of Val•H$^+$ (H_2O) and TRA•H$^+$ (H_2O) as explained below.

Recall that the spectrum of Val•H$^+$(H_2O) is characterized, in the ammonium stretch absorption region, by a broad absorption band corresponding to a hydrogen-bonded N-H vibration to water and a weak interaction with the carbonyl oxygen, while a band of moderate intensity shows evidence for free N-H stretches. The obvious difference with the spectrum of Trp•H$^+$(H_2O) is the contribution of a band which we attribute to an N-H···π interaction of the ammonium with the indole ring. Although water binds to the ammonium group in both protonated tryptophan and protonated valine, intramolecular interactions with the residue seem to play an important role in the conformational preferences of the amino acid.

The experimental spectrum of TRA•$H^+(H_2O)$ (*Fig. 4.5 (b)*) exhibits a free indole N-H at 3509 cm^{-1} and free water stretches at 3643 and 3705 cm^{-1}, indicating that water binds to the ammonium rather than to the indole N-H.

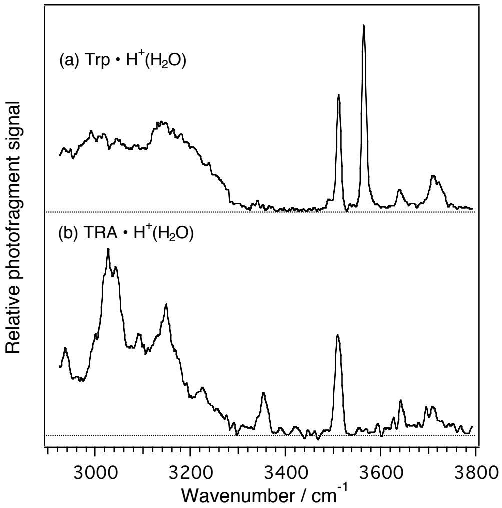

Fig. 4.5: Comparison of infrared spectra of (a) Trp•$H^+(H_2O)$ and (b) TRA•$H^+(H_2O)$

The low frequency range of TRA•$H^+(H_2O)$ spectrum is dominated by a broad absorption between 2900 and 3300 cm^{-1} exhibiting distinctive sub-bands, attributed to hydrogen bonding of N-H with water and a weak interaction of another N-H with the indole as observed in the bare ion. These bands, however, contrast with the smooth absorption profile observed in Trp•H^+ (H_2O). Moreover a stronger band characteristic of free N-H vibrations (~ 3355 cm^{-1}) is slightly blue-shifted compared to that observed for Trp•$H^+(H_2O)$. Despite the resemblance of the spectra arising from the main common characteristics of both compounds, the discrepancy between the IR spectral features of TRA•$H^+(H_2O)$ and Trp•$H^+(H_2O)$ in the NH stretching region demonstrate structural disparities between the amino acid and its model compound arising from the absence of a carboxylic acid group in the latter. Thus, comparison of protonated tryptophan with protonated tryptamine reveals the presence of weak interactions between the carboxylic group and the ammonium vibrations.

Thus, addition of the first water molecule to protonated tryptophan preferentially solvates the ammonium charge without affecting the intramolecular interactions already existing in the bare molecular ion.

4.4 $Trp•H^+(H_2O)_2$

Addition of a second water molecule induces clear changes in the spectrum of the dihydrate of protonated tryptophan (*Fig. 4.6 (a)*). The broad band below 3300 cm^{-1} depicts a higher intensity around 3000 cm^{-1} over that at ~ 3150 cm^{-1}, as opposed to the intensity ratio observed in the monohydrated cluster. Absorption in the free N-H stretch region disappears, and we notice a blue-shift and reduction in the intensity of the free COO-H band at 3572 cm^{-1} with the appearance of a small blue tail. The free water bands shift to higher frequency, and the anti-symmetric water stretch increases in intensity and broadens up, suggesting an overlap of two distinct O-H vibrations at 3713 cm^{-1} and 3743 cm^{-1}.

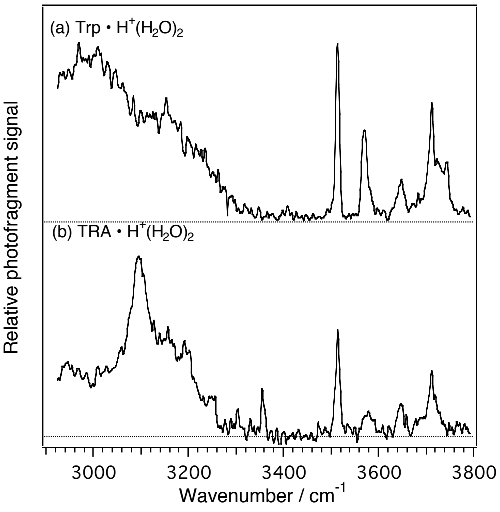

Fig. 4.6: Comparison of infrared spectra of (a) $Trp•H^+(H_2O)_2$ and (b) $TRA•H^+(H_2O)_2$

Examination of the experimental spectrum of $TRAH^+•(H_2O)_2$ (*Fig. 4.6 (b)*) provides some insight for the interpretation of the spectral features of $Trp•H^+(H_2O)_2$. The former exhibits a broad band in the low-frequency region peaking at ~ 3100 cm^{-1} and blue-shifted from the corresponding band in the monohydrate. This indicates binding of the second water molecule to the ammonium group, which is also consistent with the decrease in intensity of the free N-H absorption observed at 3355 cm^{-1} and the unperturbed free indole N-H (3515 cm^{-1}). The appearance of a new band at 3580 cm^{-1} is characteristic of a water bridging to the π-electron cloud (as mentioned earlier for Trp1_C), suggesting that one of the water molecules bridges to the indole ring.

The IR spectra of $Trp•H^+(H_2O)_2$ and $TRA•H^+(H_2O)_2$ are substantially different, therefore denoting the role of the carboxylic acid interaction with the ammonium group. The broad band of $Trp•H^+(H_2O)_2$ does not show any blue shift in comparison with the monohydrated complex. We observe a similar trend in the hydration process of protonated valine (as reported in *§3.3.3*), where the addition of the second water molecule does not induce substantial spectral modifications. This is mainly due to the breadth of the bands observed in our spectra, which limits our ability to detect small frequency shifts arising from hydrogen-bonding rearrangements. Addition of a second water molecule to protonated valine breaks the intramolecular interaction existing in the monohydrate cluster between one ammonium N-H and the carbonyl oxygen. This hydrogen-bonding rearrangement is reflected in the spectrum only by a small change in the width of the corresponding broad absorption band below 3200 cm^{-1}.

We deduce from the above considerations that the second water molecule added to protonated tryptophan also solvates the ammonium group. This could be consistent with breaking the weak interaction between the NH and the carbonyl oxygen observed at 3340 cm^{-1} in the spectrum of $Trp•H^+(H_2O)$ and disappearing in $Trp•H^+(H_2O)_2$. Moreover, the persistent absorption at ~ 3150 cm^{-1} could then be attributed to the preservation of an NH···π. Note that a substantial decrease in the intensity of the free COO-H has also been observed in the spectrum of $Val•H^+(H_2O)_2$, without any evidence of water binding to the carboxylic acid.

In order to suppport or rule out the above hypothesis and to explore plausible alternative binding motifs, we calculated the vibrational frequencies of a few candidate conformers arising from a rapid conformational search (*Fig. 4.7*). The lowest-energy conformer Trp2_A possesses an N-H stretch pointing to the indole ring, and two other N-H bound to water. In Trp2_B one of the water molecules bound to the ammonium points to the carbonyl oxygen, whereas the other one is bridging to the aromatic ring. In Trp2_C the ammonium group is rotated such as one water molecules points away from the indole ring and the other towards the ring. The free N-H points up in the opposite direction from the aromatic structure. Finally in Trp2_D one water is pointing out of the ring and the other points to the carbonyl oxygen, allowing for stabilization of one NH by the π-electrons.

All of the calculated spectra show that the N-H stretches hydrogen-bonded to water give rise to absorption bands in the 2900 – 3100 cm^{-1} region. Thus, calculations agree with the experimental spectrum of $Trp•H^+(H_2O)_2$, which shows an increase in intensity in this region. However, the spectral features in the experimental spectrum are too broad to permit any distinction between possible contributions of different conformers. Sharper bands appear above 3500 cm^{-1} in comparison to those observed in the low-energy end of the experimental spectrum. Although some of these are broadened due to an overlap of several stretches, they still possess some structure, which helps us draw a few conclusions.

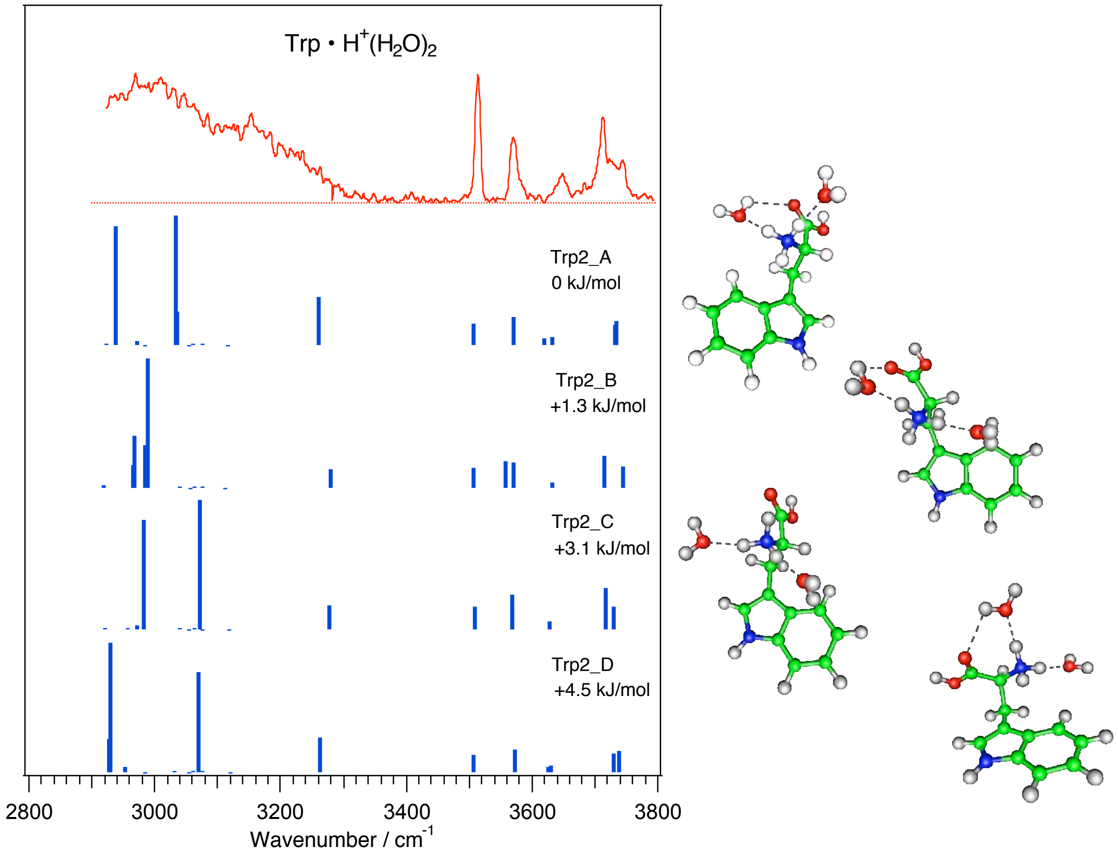

Fig. 4.7: Comparison of measured infrared spectra of Trp•H$^+$(H$_2$O)$_2$ with calculated spectra corresponding to the structures shown.

In conformers Trp2_A and Trp2_D, calculations predict water symmetric and antisymmetric stretches in the region of 3620 - 3630 cm^{-1} and 3732 - 3737 cm^{-1} respectively. This is consistent with the experimental band at 3640 cm^{-1} and with the sub-structure at ~ 3740 cm^{-1} of the observed antisymmetric stretch broad absorption. Note that the frequency of the COO-H calculated for these structures is shifted to higher frequency relative to that predicted in Trp1_A and is therefore consistent with the blue-shift experimentally observed for this band. However, the predicted frequencies of the almost overlapping water stretches cannot account for the experimental sub-band at ~ 3713 cm^{-1}. Note also, that the vibration of an ammonium pointing towards the indole ring is predicted in Trp2_A and Trp2_D, slightly higher in frequency than the experimental band observed at ~ 3200 cm^{-1}. These conformers likely contribute to the experimental spectrum, although the spectral features imply a contribution from other structures.

The calculated spectrum of Trp2_B and Trp2_C show that bridging of a water molecule to the indole ring is accompanied by a substantial red-shift of the water O-H stretch, predicted at 10 cm^{-1} to the blue of the carboxylic stretch in Trp2_B and almost overlapping with the COO-H in Trp2_C (where it is only shifted by 1 cm^{-1}). In this conformer the two water molecules are not equivalent. This could explain the appearance of the blue tail in the experimental band of the carboxylic acid together with the sub-structure of the anti-symmetric water band showing sub-peaks at 3713 cm^{-1} and 3743 cm^{-1}. The latter are in very good agreement with the predicted water bands of conformer Trp2W_B at 3715 cm^{-1} and 3745 cm^{-1}. Thus, there is some evidence that these conformers are also populated in our experiment.

Despite the spectral shifts distinguishing each of these conformers, especially in the low-energy end, our experimental data do not allow us to distinguish between any of these structures, due to the lack of sharp spectral features in the lower frequency portion of the spectrum.

4.5 Trp•H$^+$(H$_2$O)$_3$

The spectrum of Trp•H$^+$(H$_2$O)$_3$ (*Fig. 4.8*) shows some similarities with that of the dihydrate, although a few differences are obvious: the broad band below 3300 cm^{-1} is slightly blue-shifted, peaking at ~ 3050 cm^{1} and the feature assigned to the carboxylic acid O-H is broader and shifts to higher frequency (3580 cm^{-1}). We notice some weak and broad absorption to the red of the unperturbed indole N-H. Finally the broad band corresponding to free water stretches increases in intensity and shows distinct sub-bands at 3715, 3732 and 3748 cm^{-1}.

The evolution of the low-frequency broad band upon addition of the third water is similar to that observed in the spectrum of the protonated valine trihydrate, which might suggest the completion of a first solvation shell around the ammonium group.

We calculate for this cluster the vibrational frequencies of three conformers shown in *Fig.* 4.8. Conformer Trp3_A possesses a fully hydrated ammonium. In the structure of Trp3_B, two water molecules are forming a bridge between an ammonium NH and the carbonyl, while conformer Trp3_C contains two water molecules establishing a bridge from the ammonium to the indole ring.

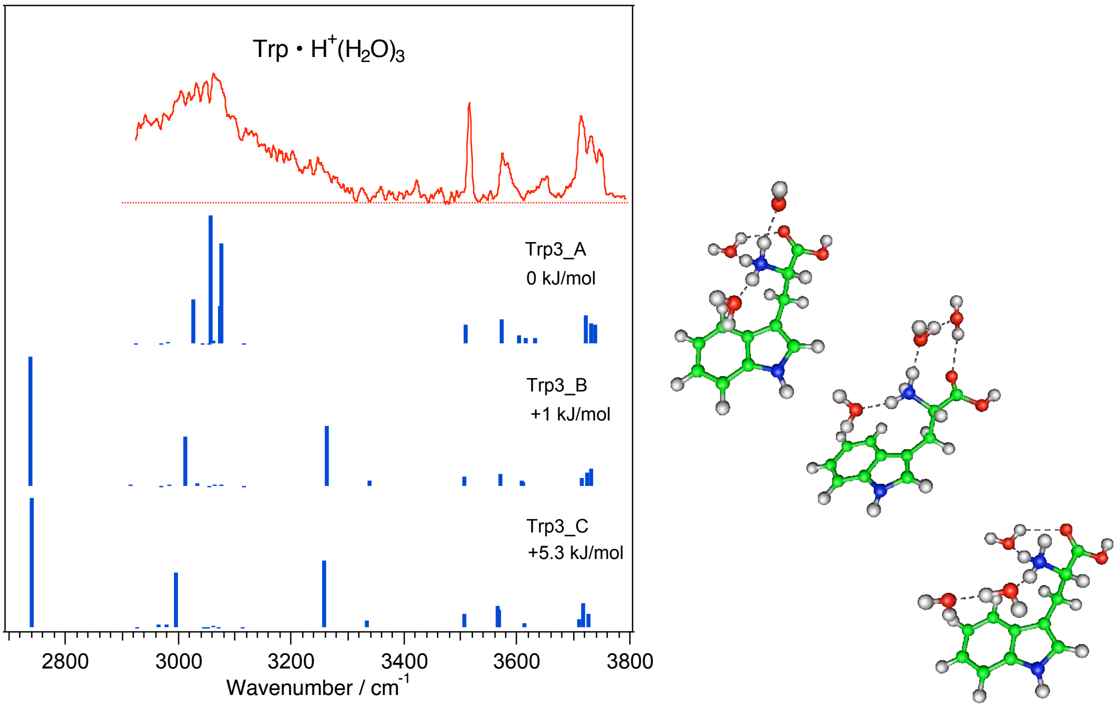

Fig. 4.8: Comparison of measured infrared spectra of Trp•$H^+(H_2O)_3$ with calculated spectra corresponding to the structures shown.

The calculated spectra for the structures with the water bridge (Trp3_B and Trp3_C) show a red-shift of the hydrogen-bonded N-H stretches relative to the predicted bands in the dihydrate, which is in contradiction with the overall blue-shift observed experimentally. An additional strong absorption is predicted at ~ 3260 cm^{-1} due to the hydrogen-bonded O-H of the AD (acceptor-donor) water bridging to the second water. There is evidence for absorption in this region in the experimental spectrum, indicating that Trp3_B and Trp3_C may contribute to the experimental spectrum, although they are not the dominant conformers.

The calculated spectrum of Trp3_A seems to give the best agreement with the experimental data. Completion of the solvation shell of the ammonium group leads to hydrogen-bonded N-H vibrations between 3000 and 3100 cm^{-1}, consistent with the blue-shifted band at the low-energy end of the measured spectrum, centered at ~3050 cm^{-1}. The experimental band at 3580 cm^{-1} is probably a convolution of two bands, one corresponding to a free carboxylic acid O-H and the other to a water O-H interacting with the indole ring, which are predicted by calculations to occur at 3572 and 3604 cm^{-1} respectively. The growth of absorption of the O-H stretch interacting with the π-electron cloud is consistent with the blue tail observed in the dihydrate of protonated tryptophan for the carboxylic acid O-H vibration. The latter was attributed to a small contribution of a conformer in which a water is attached to the ammonium NH pointing towards the aromatic residue. The structure of Trp3_A and its predicted vibrational frequencies illustrate how the water molecules hydrating the ammonium group are involved in different weak interactions with other groups of the amino acid backbone, besides their main hydrogen-bonding interaction with the ammonium N-H stretches. This is also observed experimentally in the structure of the free water band at ~ 3730 cm^{-1}, indicating the presence of three non-equivalent water molecules. One water is weakly interacting with the carbonyl oxygen as also observed in the hydrates of protonated valine, but an additional interaction between a different water and the indole residue of tryptophan is possible due to the flexibility of the alkyl backbone of the amino acid.

Tryptophan presents a higher complexity of interactions in comparison with valine due to the indole residue. Albeit, addition of the first few water molecules leads primary to solvation of the ammonium group, thus showing the importance of the electrostatic interactions over other ones in competition.

4.6 $Trp{\bullet}H^+(H_2O)_4$

The spectrum (*Fig. 4.9*) is marked by a broad band centered at higher frequency (3085 cm^{-1}) than in $Trp{\bullet}H^+(H_2O)_3$. As for smaller clusters, this band appears in the region where hydrogen-bonded N-H vibrations overlap with alkyl and aromatic C-H stretches. A constant and weak absorption is visible above 3300 cm^{-1} up to the indole N-H absorption at 3517 cm^{-1}, which remains unperturbed (thus un-solvated) even upon addition of the fourth water molecule. The feature at 3590 cm^{-1} probably originates from a blue-shift of the band observed at 3580 cm^{-1} in $Trp{\bullet}H^+(H_2O)_3$, which we attributed to a COO-H vibration overlapping with a water O-H interacting with the π-electron cloud. Between this band and that of the symmetric water stretches (3650 cm^{-1}) we discern a weak absorption at 3620 cm^{-1}. Finally the highest-frequency band in the free water stretch region gains in intensity and seems narrower.

The structures calculated for this cluster are shown in *Fig. 4.9* as well as their corresponding spectra. In Trp4_A, the ammonium group is fully solvated with each of its N-H stretches bonded to a water molecule, while the fourth water binds to the carboxylic acid. From our calculations a slightly different conformer (Trp4_B) is predicted to have an energy comparable to that of Trp4_A. Although the ammonium group is also fully solvated in Trp4_B, a cyclic structure is formed between two water molecules hydrogen-bonded to the ammonium and a third water, part of the second solvation shell. In Trp4_C, the ammonium is fully hydrated with the fourth water molecule attached to the water pointing towards the indole ring.

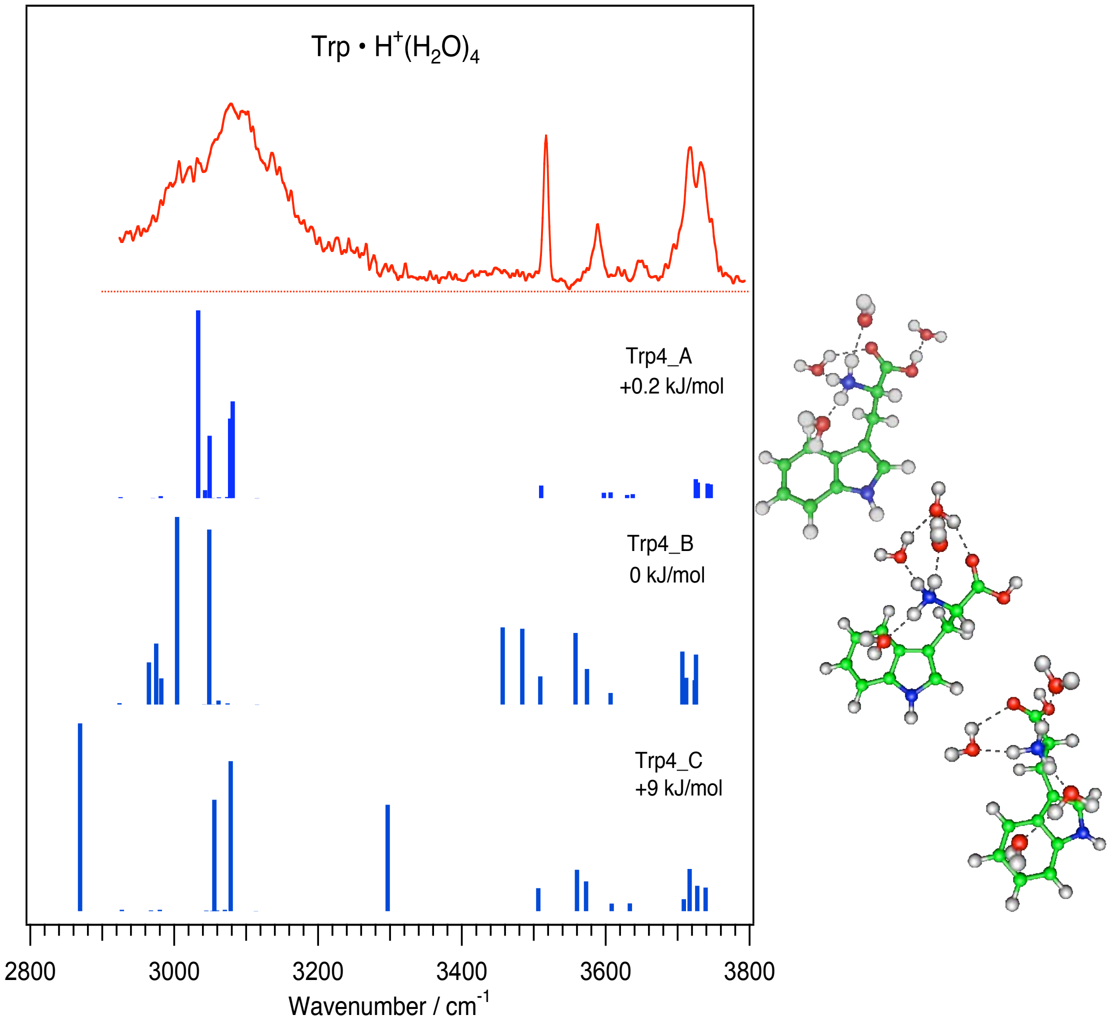

Fig. 4.9: Comparison of measured infrared spectra of Trp•$H^+(H_2O)_4$ with calculated spectra corresponding to the structures shown.

In Trp4_C, the presence of a water molecule in the second shell results in a blue-shift of the N-H vibrations attached to a single water (compared to those predicted for Trp•$(H_2O)_3$) and a red-shift of the N-H stretch, which is hydrogen-bonded to the water bridge. The latter falls out of the experimental range, but the former is in agreement with the blue-shift of the low-frequency absorption band measured experimentally. The O-H stretch vibration of the acceptor-donor (AD) water linked to the second shell water molecule is predicted at ~3300 cm^{-1}, which might be responsible for the blue tail of the broad absorption feature in the low-energy end of the spectrum, although no firm conclusion can be drawn since we cannot rely on the intensities of the bands. The O-H vibration interacting with the indole ring is predicted to appear close in frequency to the COO-H band (only shifted by ~10 cm^{-1}). These absorptions might account for the experimental feature at 3590 cm^{-1}, however calculations are offset by almost 20 cm^{-1}. A similar discrepancy is observed between experimental data and the frequencies predicted for the symmetric stretches of single acceptor water molecules in the first solvation shell. The spread in the frequencies calculated above 3700 cm^{-1} for the anti-symmetric O-H stretches of single acceptor water molecules and dangling O-H vibrations of AD water is not consistent with the narrowing of the experimental band centered at 3727 cm^{-1}. Finally, the calculated spectrum of Trp4_C cannot account for the presence of absorption to the red of the indole N-H band. Thus, the experimental spectrum does not seem to be characterized by a dominant contribution of this structure.

The calculated spectrum for Trp4_A is in good agreement with the prominent features observed experimentally. It accounts for the blue shift of the broad band in the low-frequency region of the experimental spectrum, where hydrogen-bonded N-H stretches are predicted to absorb and also the hydrogen-bonded COO-H of the carboxylic acid, which probably contributes to the red-tail of the band. Despite the red-shift of the carboxylic acid, we still measure absorption at ~ 3590 cm^{-1}, previously assigned to the overlap of a free COO-H and a water O-H interacting with the indole ring (cf. *§ 4.5*). The frequencies calculated for this conformer indicate that this band probably arises from an overlap of the absorption of a water O-H stretch bridging to the indole ring and that of a water hydrogen-bonded to the carbonyl oxygen, which are predicted by calculations respectively at 3606 cm^{-1} and 3597 cm^{-1}. The experimental band at ~ 3650 cm^{-1} can be attributed to symmetric stretches of the remaining two single acceptor water molecules: one of them accepts a hydrogen-bond from the ammonium and the other from the carboxylic acid but none of them are involved in a further interaction with their hydrogen atoms. Calculations also provide predictions for the free water O-H stretches, which reproduce well the structure of the highest-frequency band observed experimentally around 3727 cm^{-1}. The latter is split in two sub-bands, one arising from the antisymmetric stretches of the single acceptor waters and the other from the free O-H stretches of the water molecules involved in further weak, or hydrogen-bonding interactions. Thus, conformer Trp4_A certainly contributes to the experimental spectrum but it is not the only species present since its calculated spectrum cannot account for the broad and constant absorption signal of low intensity appearing to the red of the free indole N-H.

Conformer Trp4_B illustrates a structure where two water molecules (AD) in the first solvent shell and a double acceptor water in the second shell form a cycle. Such a structure has been observed in the water clusters of both protonated and lithiated valine upon addition of the fourth water molecule (cf. *§ 3.3.5* and *§ 3.5*). The calculated spectrum predicts bands to the red of the indole N-H at ~ 3460 and 3480 cm^{-1} characteristic of the coupled stretches of the two AD water molecules. A weak contribution of this conformer to the experimental spectrum may account for the absorption observed to the red of the indole N-H. It seems that this conformer becomes the dominant structure in the water cluster of protonated tryptophan upon addition of the fifth water molecule.

4.7 Trp•$H^+(H_2O)_5$

The experimental spectrum (*Fig. 4.10 (a)*) shows a higher intensity of the absorption band to the red of the indole N-H, which is consistent with the presence of a water cycle like that of Trp4_B, predicted as a stable conformer for Trp•$H^+(H_2O)_4$. It is interesting to note that the spectrum of TRA•$H^+(H_2O)_4$ (*Fig. 4.10 (b)*) presents distinct absorption bands to the red of the indole N-H at 3461 and 3490 cm^{-1}, possibly indicating the formation of a similar water cluster upon addition of the fourth water molecule. The broadened features in the measured spectrum of Trp•$H^+(H_2O)_5$, likely reveal the presence of several conformers overlapping in the spectrum. This is not surprising since our technique is not conformer specific and the temperature of the ions is such that different conformers may be populated. The increase in conformational diversity after completion of the first shell in the ammonium complicates the interpretation of the experimental data, which is mainly limited by the breadth of the observed bands.

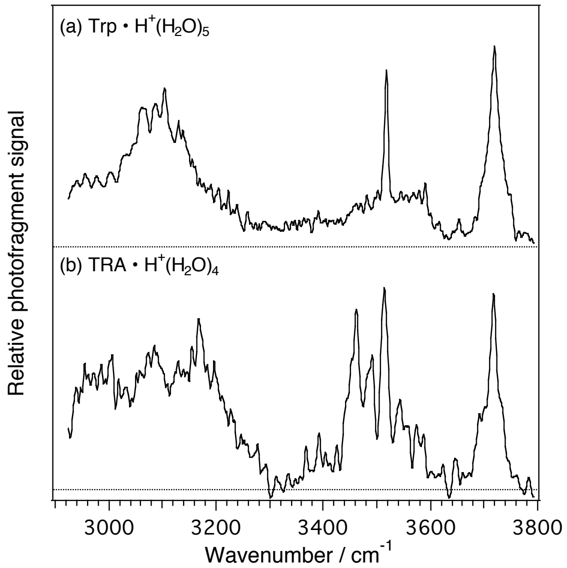

Fig. 4.10: Comparison of infrared spectra of (a) Trp•$H^+(H_2O)_5$ and (b) TRA•$H^+(H_2O)_4$

4.8 DISCUSSION

By comparing the IR photofragmentation spectra of water clusters of protonated tryptophan with those of protonated tryptamine and protonated valine, we have inferred information on the hydration process of the former.

The vibrational features allow us not only to identify where the water molecules bind upon solvation of the amino acid but also reflect finer structural details providing some insight on the competition between stabilizing intramolecular interactions of the ammonium group with the indole ring or the carbonyl group and intermolecular interactions with the water molecules. Although some information can be deduced from gross spectral changes, we lack the ability of providing finer structural details due to the limitation imposed by the breadth of the bands measured experimentally.

However the following conclusions have been drawn. The lowest-energy conformer of protonated tryptophan calculated by Weinkauf and coworkers [9] is not the lowest energy conformer in our DFT calculations. As already discussed in *Chapter 2* (cf. *§ 2.4.4*) and also demonstrated by the study of Williams and coworkers [13], DFT calculations do not allow one to draw conclusions on the relative energies of the different conformers calculated. Higher-level *ab initio* calculations are more suitable for precise estimations. However, in this study the major goal of the calculations was to provide insight on the spectral features characterizing a variety of conformers, since we have performed room temperature experiments and it is unlikely that our spectra can be interpreted solely on the basis of the lowest energy conformation (cf. *§ 2.2.4.2*).

Our structural assignments show that hydration occurs primarily at the ammonium group, with additional stabilizing interactions of the water molecules with other sites (indole ring and carbonyl group), which thus displace the intramolecular interactions existing in the bare molecular ion. Other sites on the amino acid backbone (carboxylic acid group and the indole N-H) are not affected by solvation upon addition of up to three water molecules. Although the indole N-H is not involved in the hydration process, even for the higher order clusters investigated here, there is experimental evidence for binding of water to the carboxylic acid upon completion of the first solvation shell of the ammonium group.

As in the case of protonated valine, it appears that hydration is driven by electrostatic interactions with the ammonium and that formation of a cyclic structure of the water network is typical after completion of the solvation shell around the charged group. It is interesting to note that water bridges play an important role in the hydration of neutral flexible aromatic molecules [14] and particularly in the hydrates of neutral tryptophan [6]. However, it appears that such bridges are not favored in the presence of a charged group in the molecule. This illustrates the fundamental difference between the solvation processes of charged and neutral species.

Although this is not a surprise, hydration of protonated amino acids gives rise to clearly different structural arrangements than those observed in the corresponding neutral clusters as suggested by the comparison of the results presented in this work with those of Snoek *et al* [6]. Based on this different organization of the solvent network in neutral and protonated tryptophan, we could speculate that the transition to the zwitterionic form in the water clusters of the neutral amino acid has not been observed at low hydration levels by Snoek *et al* [6] because a major structural rearrangement of the water network would be necessary for proper solvation of the charges of the zwitterion. Such a reorganization might not be favored entropically. Therefore, the investigation of higher-order water clusters of both neutral and protonated amino acids should provide important insights on the issue of zwitterion formation and a comparison of the solvation shell structures resulting from theses studies should help elucidate the origin of the stabilization of the zwitterion.

References

1. Rizzo, T. R., Park, Y. D., Peteanu, L. A., and H., L. D., J. Chem. Phys (1985), 83, 4819-4820.
2. Rizzo, T. R., Park, Y. D., Peteanu, L. A., and Levy, D. H., J. Chem. Phys. (1986), 84, 2534-2541.
3. Snoek, L. C., Kroemer, R. T., Hockridge, M. R., and Simons, J. P., Phys. Chem. Chem. Phys. (2001), 3, 1819-1826.
4. Compagnon, I., Hagemeister, F. C., Antoine, R., Rayane, D., Broyer, M., Dugourd, P., Hudgins, R. R., and Jarrold, M. F., J. Am. Chem. Soc. (2001), 123, 8440-8441.
5. Peteanu, L. A. and Levy, D. H., J. Phys. Chem. (1988), 92, 6554-6561.
6. Snoek, L. C., Kroemer, R. T., and Simons, J. P., Phys. Chem. Chem. Phys. (2002), 4, 2130-2139.
7. Kang, H., Dedonder-Lardeux, C., Jouvet, C., Gregoire, G., Desfrancois, C., Schermann, J. P., Barat, M., and Fayeton, J. A., J. Phys. Chem. A (2005), 109, 2417-2420.
8. Kang, H., Dedonder-Lardeux, C., Jouvet, C., Martrenchard, S., Gregoire, G., Desfrancois, C., Schermann, J. P., Barat, M., and Fayeton, J. A., Phys. Chem. Chem. Phys. (2004), 6, 2628-2632.
9. Nolting, D., Marian, C., and Weinkauf, R., Phys. Chem. Chem. Phys. (2004), 6, 2633-2640.
10. Talbot, F. O., Tabarin, T., Antoine, R., Broyer, M., and Dugourd, P., J. Chem. Phys. (2005), 122, -.
11. Carney, J. R. and Zwier, T. S., J. Phys. Chem. A (2000), 104, 8677-8688.
12. Carney, J. R., Dian, B. C., Florio, G. M., and Zwier, T. S., J. Am. Chem. Soc. (2001), 123, 5596-5597.
13. Jockusch, R. A., Lemoff, A. S., and Williams, E. R., J. Phys. Chem. A (2001), 105, 10929-10942.
14. Zwier, T. S., J. Phys. Chem. A (2001), 105, 8827-8839.

Conclusions and perspectives

We have presented in this work the implementation of laser photofragment spectroscopy in a home-built electrospray ionization ion trap tandem mass spectrometer for the study of biologically related molecular ions. Although the design and building of the instrument constituted a large part of the work, we also demonstrated the successful implementation of this new technique to follow the microsolvation process of charged amino acids in the gas phase. We obtained IR photofragmentation spectra of the hydrates of protonated and lithiated valine and those of protonated tryptophan in the light atom stretching region.

In the study of $\mathrm{Val{\bullet}Li^+(H_2O)_n}$, we addressed the problem of zwitterion formation in the gas phase due to the stabilization effect of water and an external ion. By probing the region of N-H and O-H stretching vibrations and based on theoretical calculations, we demonstrated that zwitterion formation does not occur in the hydrates of lithiated valine with up to four water molecules. The vibrational signatures of $\mathrm{Val{\bullet}H^+(H_2O)_n}$ provide further evidence for the absence of the zwitterionic form in $\mathrm{Val{\bullet}Li^+(H_2O)_n}$. Thus, our results refute the conclusion that zwitterion formation appears upon addition of the third water molecule in lithiated valine, drawn by Williams and coworkers on the basis of dissociation rates obtained in BIRD experiments [1]. In the hydration process of protonated tryptophan we probe the effect of a higher degree of complexity of the amino acid. Despite the presence of an extra site of hydration (indole N-H) in the indole residue and intramolecular interactions in competition, water primarily solvates the charge similarly to what has been observed for lithiated and protonated valine.

Moreover, we have demonstrated that our technique is sensitive to structural changes in the cluster, which are either related to an amino acid backbone conformational change or to the organization of the water network. For instance, in $\mathrm{Val{\bullet}Li^+(H_2O)_3}$ the presence of the third water molecule results in a conformational change of valine and a modification of the lithium binding from NO to OO coordination. On the other hand, hydration does not seem to affect the conformational preferences of the protonated amino acids studied here. Common structural features have been observed in the build up of the solvation shell for all the clusters studied, in that a first solvation shell is created around the charge of the amino acid (either lithium, or ammonium group) and after its completion (n=3), formation of a second shell occurs rather than hydration of other sites on the amino acid backbone. A striking result revealed by our spectra is the evidence for some preferred structures for the solvent network common to lithiated and protonated valine. It seems that the former is stabilized by forming of cyclic structure upon the addition of the first water molecule in the second shell.

We have been able to answer in these studies some of the fundamental questions related to microsovation of molecules of biological interest in the gas phase posed in the introduction. We gained insights both into the conformational changes of the amino acid induced by solvation and in the organization of the water network. The question of how many molecules are necessary to recover the bulk behavior has not yet been resolved. The answer to this question clearly necessitates investigations of higher-order hydration levels and may reside in the comparison of spectral data obtained on hydrated neutral molecules with those measured by our technique on the corresponding ions. We can imagine that the level of hydration where spectral features of both species become similar indicates a bulk behavior. However, the broadening of absorption bands observed in our spectra as the number of water molecules increases might prevent us from answering this question.

The investigation of such small systems can provide good test cases for theory so as to improve the ability of the latter to predict molecular properties. This is an important issue, since the data interpretation largely relies upon theoretical calculations of vibrational frequencies. Although, not all features in our spectra are fully resolved and unambiguous assignments are not always possible, theory still provides invaluable guidance in the analysis. On the other hand, theory should predict sufficiently accurate frequencies to enable firm spectral assignments. Thus, the appropriate method or force field should be used so that the dominant interactions are correctly modeled in the calculations. Finally, comparing the relative energies, yielded by DFT for different conformers, should be done with care. Higher-level *ab initio* calculations are more suitable for precise energy calculations.

Knowing the limits of theory, we made some spectral assignments by measuring the experimental spectra of analogous compounds, although the latter does not provide answers to all ambiguities. Thus, our spectral assignments are largely based on DFT calculations, which constitute one of the limits of our interpretations, since DFT calculations are well known for their poor treatment of dispersion forces [2]. Moreover, it is important to go beyond the harmonic approximation and treat correctly anharmonic effects, which may play an important role in the clusters investigated here, where non-covalent interactions are predominant. Anharmonic effects have been extensively addressed by Gerber and coworkers, who studied the performance of DFT in predicting anharmonic frequencies [3].

As illustrated by the results of lithiated and protonated valine water clusters, the frequencies calculated for different conformers corresponding to the same hydration level show in many cases ambiguities in the assignment of the absorption bands observed experimentally, which could be reduced if a larger spectral region was sampled in the experiment. Thus, interpretation of the photofragmentation spectra would be facilitated and would not rely so strongly on theoretical calculations. The larger the spectral range investigated experimentally, the richer the information. For instance, it would not be difficult to implement in our laboratory the difference frequency mixing technique used by Gerhards and coworkers [4] to enlarge the range of investigation to the mid-IR region, which would extend the capabilities of our technique in terms of structural characterizations.

The most important limitation in the studies presented in this work is spectral congestion. There is some spectral broadening due to the temperature of the ions, since we do not cool them. At room temperature, many stable conformers may be populated, which can exhibit spectral signatures in the vibrational spectra. If small structural changes characterize different conformers, small spectral shifts would be observed and result in an overlap of the contribution of different conformers. The highest degree of congestion appears in the region of hydrogen-bonded stretches, which also corresponds to the region containing the richest information.

Thus, an important improvement of our technique would be to implement an ion-mobility stage prior to irradiation of the ions, so that conformation/mass-selective photofragmentation spectroscopy is possible. Moreover, with the use of a time-of-flight in lieu of the final quadrupole mass spectrometer, we could perform two-dimensional spectroscopy by measuring simultaneously the photofragmentation mass spectrum and vibrational spectrum of a single conformer. It is not unlikely that the fragmentation mass spectra differ for different conformers and therefore contain additional information useful for structural determinations.

The second improvement of our instrument concerns the ability to obtain well-resolved spectra of cooled ions. Recent infrared photofragmentation studies on protonated water clusters reported by Johnson and coworker [5] have shown the benefit of using argon- tagging and especially neon-tagging in order to detect photofragmentation of the cluster as opposed to boiling off one water molecule. The internal energy of ions is substantially reduced (to that determined by the binding energy of the atom) so that less congestion is visible in the spectra. Despite the promising data obtained with neon-tagging [5], the presence of the tag introduces a perturbation in the cluster, which can be visible in the vibrational spectra.

A more efficient way to cool the ions at lower temperatures and without perturbing the molecule is to use a cold 22-pole ion trap [6]. The trapped ions are cooled radiatively and by collisions with cold helium down to ~ 10 K. The photofragment spectrometer described in the present work has recently been modified in order to incorporate such an ion trap instead of the long section of the octupole ion guide. The first electronic photofragmentation spectra of protonated tryptophan and its hydrates with up to two waters, and tyrosine have been measured in our laboratory and have already demonstrated the importance of cooling for understanding the photophysics of these ions. The sharp spectral features observed for tyrosine (~ 3 cm^{-1}) indicate the tremendous cooling of the ion, which has been estimated to be on the order of 6 K. The obtention of well-resolved spectral features for the dihydrate of protonated tryptophan opens up the doors of conformational selective spectroscopy using an IR/UV double resonance technique. We expect that these conformational selective studies at low temperature will provide new insights on the interpretation of our room temperature spectra.

The 22-pole cooled ion trap dramatically extends the range of applications of our apparatus allowing all kinds of spectroscopic schemes (in the IR to the UV range of the spectrum) to be applied to practically all sizes and types of biological ions and their hydrates.

References

1. Lemoff, A. S. and Williams, E. R., J. Am. Soc. Mass Spectrom. (2004), 15, 1014-1024.
2. Hobza, P., Sponer, J., and Reschel, T., J. Comput. Chem. (1995), 16, 1315-1325.
3. Wright, N. J. and Gerber, R. B., J. Chem. Phys. (2000), 112, 2598-2604.
4. Gerhards, M., Unterberg, C., and Gerlach, A., Phys. Chem. Chem. Phys. (2002), 4, 5563-5565.
5. Hammer, N. I., Diken, E. G., Roscioli, J. R., Johnson, M. A., Myshakin, E. M., Jordan, K. D., McCoy, A. B., Huang, X., Bowman, J. M., and Carter, S., J. Chem. Phys. (2005), 122.
6. Gerlich, D., Physica Scripta (1995), T59, 256-263.

List of Figures

List of Tables

Appendix

Simion programs for ion trajectory simulations in the photofragment spectrometer.

The simulations have been performed using Simion 3D Version 7.0. In order to draw all elements of the photofragment spectrometer at sufficient resolution for a proper modeling of the electric fields, the system was split in seven different sections, which are described below:

- *quadin*: comprises the entrance lens of the first quadrupole (Q_{1in}) and a small section of the quadrupole rods (for continuity reasons).
- *quad1*: contains the quadrupole rods where both the time-varying and DC components of the electric field are applied.
- *bender1*: contains the last section of the first quadrupole (for continuity reasons), the bender electrodes (two pairs of poles, B_1^+ and B_1^-, and two pairs of electrodes, B_{1in} and B_{1out}), the five electrostatic lenses ($L_1 - L_5$), the octopole entrance lens (O_{in}) and a small section of the octopole rods (for continuity reasons).
- *octo*: comprises the major section of the octopole rods, where the rf-only electric field is applied.
- *bender2*: includes the last section of the octopole rods (for continuity reasons), the octopole exit lens (O_{out}), the bender electrodes (two pairs of poles, B_2^+ and B_2^-, and two pairs of electrodes, B_{2in} and B_{2out}), the entrance lens (Q_{2in}) and a small section of the final quadrupole rods.
- *quad2*: contains the rods of the final quadrupole mass analyzer, where the RF and DC components of the electric field are applied.
- *quadout*: comprises the last section of the rods and the exit electrode (Q_{2out}) of the second quadrupole

Quadin, *quad*, *octo* and *quad2* have been drawn directly on the potential array, while geometry files have been used to draw *bender1, bender2 and quadout*. The codes written for each of these geometry files (bender1.gem, bender2.gem and quadout.gem) are given at the end of this appendix.

User-programs have been written for each section in order to define the electrostatic and time-depend electric fields of the electrodes. Each user-program (quadin.prg, quad.prg, bender1.prg, octo.prg, bender2.prg, quad2.prg and quadout2.prg) controls the voltages in a section of the instrument when ions are flying in an ion trajectory simulation. We give below the codes of these programs necessary to run a simulation.

(1) QUADIN.PRG

```
; definition of user adjustable variables ----------------------
              ; ---------- adjustable during flight -----------------
defa _Percent_tune                       99.0                    ; percent of optimum tune
defa _AMU_Mass_per_Charge                205.0                   ; mass tune point in amu/unit charge
defa _Quad_Entrance_Voltage              0.0                     ; voltage of quad entrance
defa _Quad_Axis_Voltage                  1.5                     ; voltage of quad axis
defa _Quad_Exit_Voltage                  -10.0                   ; voltage of quad exit
   ; ---------- adjustable at beginning of flight -----------------
defa PE_Update_each_usec                 0.001                   ; pe surface update time step in usec
defa Percent_Energy_Variation            10.0                    ; (+- 10%) random energy variation
defa Cone_Angle_Off_Vel_Axis             2.0                     ; (+- 2 deg) cone angle - sphere
defa Random_Offset_mm                    0.1                     ; del start position (y,z) in mm
defa Random_TOB                          0                       ; random time of birth over one cysle
defa Phase_Angle_Deg                     80.0                    ; entry phase angle of ion
defa Frequency_Hz                        1.2E6                   ; rf frequency of quad in (Hz)
defa Effective_Radius_in_cm              0.43                    ; effective quad radius r0 in cm

; definition of static variables -----------------------------
defs first                               0.0                     ; first call flag
defs scaled_rf_quad                      0.0                     ; scaled rf base
defs rfvolts_quad                        0.0                     ; rf voltage
defs dcvolts_quad                        0.0                     ; dc voltage
defs omega                               1.2                     ; freq in radians / usec
defs theta_quad                          0.0                     ; phase offset in radians
defs Next_PE_Update_I                    0.0                     ; next time to update pe surface

; program segments below -------------------------------------------
;----------------------------------------------------------------------
seg initialize                                                   ; randomize ion's position, ke , direction
              ;------------------- get ion's initial velocity components -------------
              rcl ion_vz_mm                                      ; get ion's specified velocity components
              rcl ion_vy_mm
              rcl ion_vx_mm
              ;------------------- convert to 3d polar coords -------------
              >p3d                                               ; convert to polar 3d
              ;------------------- save polar coord values ----------------
              sto speed rlup                                     ; store ion's speed
              sto az_angle rlup                                  ; store ion's az angle
              sto el_angle                                       ; store ion's el angle

              ;------------------- make sure Percent_Energy_Variation is legal -------------
                                                                 ; force 0 <= Percent_Energy_Variation <= 100
              rcl Percent_Energy_Variation abs
              100 x>y rlup sto Percent_Energy_Variation

              ;------------------- make sure Cone_Angle_Off_Vel_Axis is legal -------------
                                                                 ; force 0 <= Cone_Angle_Off_Vel_Axis <= 180
              rcl Cone_Angle_Off_Vel_Axis abs
              180 x>y rlup sto Cone_Angle_Off_Vel_Axis

              ; --------------------- calculate ion's defined ke -------------
              rcl ion_mass                                       ; get ion's mass
              rcl speed                                          ; recall its total speed
              >ke                                                ; convert speed to kinetic energy
              sto kinetic_energy                                 ; save ion's defined kinetic energy

              ; --------------------- compute new randomized ke -------------
                                                                 ; convert from percent to fraction
              rcl Percent_Energy_Variation 100 /
              sto del_energy 2 * rand *                          ; fac = 2 * del_energy * rand
              rcl del_energy - 1 +                               ; fac += 1 - del_energy
              rcl kinetic_energy *                               ; new ke = fac * ke
```

```
          ; --------------------- convert new ke to new speed -----------
          rcl ion_mass                              ; recall ion mass
          x><y                                      ; swap x any y
          >spd                                      ; convert to speed
          sto speed                                 ; save new speed

          ;-- compute randomized el angle change 90 +- Cone_Angle_Off_Vel_Axis -------
          ;-------- we assume elevation of 90 degrees for mean ----------
          ;-------- so cone can be generated via rotating az +- 90 -------
                                                    ; (2 * Cone_Angle_Off_Vel_Axis * rand)
          2 rcl Cone_Angle_Off_Vel_Axis * rand *
                                                    ;  - Cone_Angle_Off_Vel_Axis + 90
          rcl Cone_Angle_Off_Vel_Axis - 90 +

          ;-------------- compute randomized az angle change ------------
          ;--------- this gives 360 effective because of +- elevation angels ---
          180 rand * 90 -                           ; +- 90 randomized az

          ;---------------------- recall new ion speed ------------------
          rcl speed                                 ; recall new speed

          ;--------- at this point x = speed, y = az, z = el --------------
          ;------------- convert to rectangular velocity components ---------
          >r3d                                      ; convert polar 3d to rect 3d

          ;------------- el rotate back to from 90 vertical -------------
          -90 >elr

          ;------------- el rotate back to starting elevation -------------
          rcl el_angle >elr

          ;------------- az rotate back to starting azimuth -------------
          rcl az_angle >azr

          ;------------- update ion's velocity components with new values --------
          sto ion_vx_mm                             ; return vx
          rlup
          sto ion_vy_mm                             ; return vy
          rlup
          sto ion_vz_mm                             ; return vz

          ;--------- randomize ion's position components --------
          rcl Random_Offset_mm
          2 / sto half_pos                          ; save half max shift
          rcl ion_py_mm                             ; get nominal y start
          rcl Random_Offset_mm rand * +             ; add random shift
          rcl half_pos -                            ; subtract half shift
          sto ion_py_mm                             ; store random y start
          rcl ion_pz_mm                             ; get nominal z start
          rcl Random_Offset_mm rand * +             ; add random shift
          rcl half_pos -                            ; subtract half shift
          sto ion_pz_mm                             ; store random z start
          ;--------- randomize ion's time of birth --------
          rcl Random_TOB abs rand *                 ; create random time of birth
          sto Ion_Time_of_Birth                     ; use it for ion
          ;--------------------- done ----------------------------------------
;----------------------------------------------------------------------
seg Fast_Adjust                                     ; generates rf with fast adjust
                                                    ; has first pass initialization
  rcl first                                         ; recall first pass flag
  x=0 gsb init                                      ; if this is first reference  --> init

  rcl scaled_rf_quad
  rcl _AMU_Mass_per_Charge *                        ; multiply by mass per unit charge
  sto rfvolts_quad                                  ; save rf voltage
  rcl scaled_rf_quad
  rcl _AMU_Mass_per_Charge *                        ; multiply by mass per unit charge
  rcl _Percent_tune *                               ; substitute dc tune point
  100 /
  0.1678399 *
  sto dcvolts_quad
```

```
   rcl _Quad_Entrance_Voltage
   sto Adj_elect04                             ; update quad entrance voltage

   rcl Ion_Time_of_Flight                      ; current tof in micro seconds
   rcl omega *                                 ; omega * tof
   rcl theta_quad +                            ; add phasing angle
   sin                                         ; sin(theta + (omega * tof))
   rcl rfvolts_quad *                          ; times rf voltage
   rcl dcvolts_quad +                          ;
   sto tempvolts                               ; save rf voltage
   rcl _Quad_Axis_Voltage +                    ; add quad axis voltage
   sto Adj_Elect01                             ; electrode 1 voltage
   rcl _Quad_Axis_Voltage                      ; rcall quad axis voltage
   rcl tempvolts -                             ; subtract rf dc from it
   sto Adj_Elect02                             ; electrode 2 voltage
   exit                                        ; exit program segment

   lbl init                                    ; parameter initialization subroutine
   1 sto first                                 ; turn off first pass flag
   RCL Effective_Radius_in_cm                  ; recall effective radius in cm
   entr *                                      ; (r * r)
   rcl Frequency_Hz entr * *                   ; multiply by frequency squared
   7.22175e-12 *                               ;7.22175e-12*MASS*FREQ*FREQ*R0*R0
   sto scaled_rf_quad
   rcl _AMU_Mass_per_Charge *                  ; multiply by mass per unit charge
   sto rfvolts_quad                            ; save rf voltage
   rcl scaled_rf_quad
   rcl _AMU_Mass_per_Charge *                  ; multiply by mass per unit charge
   rcl _Percent_tune *                         ; substitute dc tune point
   100 /
   0.1678399 *
   sto dcvolts_quad                            ; save dc voltage

   rcl Phase_Angle_Deg
   >rad                                        ; degrees to radians
   sto theta_quad                              ; phase angle
   rcl Frequency_Hz                            ; rf frequency in Hz
   6.28318E-6 *                                ; to radians / microsecond
   sto omega                                   ; save frequency in radians / usec
   rtn                                         ; return from subroutine

;------------------------------------------------------------------------
seg Other_Actions                              ; used to control pe surface updates
   rcl Next_PE_Update_I                        ; recall time for next pe surface update
   rcl ion_time_of_flight                      ; recall ion's time of flight
   x<y exit                                    ; exit if tof less than next pe update
   rcl PE_Update_each_usec                     ; recall pe update increment
   + sto Next_PE_Update_I                      ; add to tof and store as next pe update
   1 sto Update_PE_Surface                     ; request a pe surface update
```

(2) QUAD.PRG

```
; definition of user adjustable variables  -----------------------
; ---------- adjustable during flight -----------------
defa _Percent_tune               99.0          ; percent of optimum tune
defa _AMU_Mass_per_Charge        205.0         ; mass tune point in amu/unit charge
defa _Quad_Entrance_Voltage      0.0           ; voltage of quad entrance
defa _Quad_Axis_Voltage          1.5           ; voltage of quad axis
defa _Quad_Exit_Voltage          -10.0         ; voltage of quad exit

; ---------- adjustable at beginning of flight -----------------
defa PE_Update_each_usec         0.001         ; pe surface update time step in usec
defa Phase_Angle_Deg             80.0          ; entry phase angle of ion
defa Frequency_Hz                1.2E6         ; rf frequency of quad in (Hz)
defa Effective_Radius_in_cm      0.43          ; effective quad radius r0 in cm

; definition of static variables -----------------------------
defs scaled_rf_quad              0.0           ; scaled rf base
defs rfvolts_quad                0.0           ; rf voltage
```

```
defs dcvolts_quad                       0.0                 ; dc voltage
defs omega                              1.2                 ; freq in radians / usec
defs theta_quad                         0.0                 ; phase offset in radians
defs Next_PE_Update_II                  0.0                 ; next time to update pe surface

; program segments below -------------------------------------------
;----------------------------------------------------------------------
seg Fast_Adjust                                             ; generates rf with fast adjust
rcl scaled_rf_quad
rcl _AMU_Mass_per_Charge *                                  ; multiply by mass per unit charge
sto rfvolts_quad                                            ; save rf voltage
rcl scaled_rf_quad
rcl _AMU_Mass_per_Charge *                                  ; multiply by mass per unit charge
rcl _Percent_tune *                                         ; substitute dc tune point
100 /
0.1678399 *
sto dcvolts_quad                                            ; save dc voltage
rcl Ion_Time_of_Flight                                      ; current tof in micro seconds
rcl omega *                                                 ; omega * tof
rcl theta_quad +                                            ; add phasing angle
sin                                                         ; sin(theta + (omega * tof))
rcl rfvolts_quad *                                          ; times rf voltage
rcl dcvolts_quad +                                          ; add dc voltage
sto tempvolts                                               ; save rf dc voltage
rcl _Quad_Axis_Voltage +                                    ; add quad axis voltage
sto Adj_Elect01                                             ; electrode 1 voltage
rcl _Quad_Axis_Voltage                                      ; recall quad axis voltage
rcl tempvolts -                                             ; subtract rf dc from it
sto Adj_Elect02                                             ; electrode 2 voltage
exit                                                        ; exit program segment

;----------------------------------------------------------------------
seg Other_Actions                                           ; used to control pe surface updates
rcl Next_PE_Update_II                                       ; recall time for next pe surface update
rcl ion_time_of_flight                                      ; recall ion's time of flight
x<y exit                                                    ; exit if tof less than next pe update
rcl PE_Update_each_usec                                     ; recall pe update increment
+ sto next_pe_update_II                                     ; add to tof and store as next pe update
1 sto Update_PE_Surface                                     ; request a pe surface update
```

(3) BENDER1.PRG

```
;------- definition of user adjustable variables  -----------------------
         ; ---------- adjustable during flight QUADRUPOLE -----------------
defa _Percent_tune                      99.0                ; percent of optimum tune
defa _AMU_Mass_per_Charge               205.0               ; mass tune point in amu/unit charge
defa _Quad_Entrance_Voltage             0.0                 ; voltage of quad entrance
defa _Quad_Axis_Voltage                 1.5                 ; voltage of quad axis
defa _Quad_Exit_Voltage                 -10.0               ; voltage of quad exit

         ; ---------- adjustable at beginning of flight -----------------
defa PE_Update_each_usec                0.001               ; pe surface update time step in usec
defa Phase_Angle_Deg                    80.0                ; entry phase angle of ion
defa Frequency_Hz                       1.2E6               ; rf frequency of quad in (Hz)
defa Effective_Radius_in_cm             0.43                ; effective quad radius r0 in cm

; ------------definition of static variables -----------------------------
defs premier                            0.0
defs scaled_rf_quad                     0.0                 ; scaled rf base
defs rfvolts_quad                       0.0                 ; rf voltage
defs dcvolts_quad                       0.0                 ; dc voltage
defs omega                              1.2                 ; freq in radians / usec
defs theta_quad                         0.0                 ; phase offset in radians
defs Next_PE_Update_III                 0.0                 ; next time to update pe surface


; ========================OCTOPOLE===================================
defa _rf_Amplitude_octo                 500
defa _octo_entrance_voltage             1
```

```
defa _octo_axis_voltage                  0
defa _octo_exit_voltage                  -10
defa Frequency_Hz_octo                   2.1E6               ; in Hz
defs omega_octo                          2.1                 ; freq of octopole

; program segments below -------------------------------------------
;----------------------------------quadrupole--------------------------
seg Fast_Adjust                                              ; generates rf with fast adjust
   rcl scaled_rf_quad
   rcl _AMU_Mass_per_Charge *                                ; multiply by mass per unit charge
   sto rfvolts_quad                                          ; save rf voltage
   rcl scaled_rf_quad
   rcl _AMU_Mass_per_Charge *                                ; multiply by mass per unit charge
   rcl _Percent_tune *                                       ; substitute dc tune point
   100 /
   0.1678399 *
   sto dcvolts_quad

   rcl _Quad_Exit_Voltage
   sto Adj_elect04                                           ; update quad exit voltage

   rcl Ion_Time_of_Flight                                    ; current tof in micro seconds
   rcl omega *                                               ; omega * tof
   rcl theta_quad +                                          ; add phasing angle
   sin                                                       ; sin(theta + (omega * tof))
   rcl rfvolts_quad *
   rcl dcvolts_quad +                                        ; times rf voltage
   sto tempvolts                                             ; save rf dc voltage
   rcl _Quad_Axis_Voltage +                                  ; add quad axis voltage
   sto Adj_Elect01                                           ; electrode 1 voltage
   rcl _Quad_Axis_Voltage                                    ; recall quad axis voltage
   rcl tempvolts -                                           ; subtract rf dc from it
   sto Adj_Elect02                                           ; electrode 2 voltage

   ;------------------------------octopole---------------------
   rcl premier
   x=0 gsb initial

   rcl _octo_entrance_voltage
   sto Adj_Elect17
   RCL Ion_Time_of_Flight
   rcl omega_octo
   *
   Sin
   RCL _rf_Amplitude_octo *
   sto temp
   rcl _octo_axis_voltage
   +
   STO Adj_Elect15                                           ; rod 2,4,6,8
   rcl _octo_axis_voltage
   rcl temp -
   sTO Adj_Elect14                                           ; rod 1,3,5,7
   exit

lbl initial
   1 sto premier

   rcl Frequency_Hz_octo
   6.28318E-6 *
   sto omega_octo
   rtn

;---------------------------------------------------------
seg tstep_adjust
   rcl ion_time_step 0.0013
   x>y exit
   sto ion_time_step
exit

;----------------------------------------------------------------------
seg Other_Actions                                            ; used to control pe surface updates
   rcl Next_PE_Update_III                                    ; recall time for next pe surface update
```

```
   rcl ion_time_of_flight                          ; recall ion's time of flight
   x<y exit                                        ; exit if tof less than next pe update
   rcl PE_Update_each_usec                         ; recall pe update increment
   + sto Next_PE_Update_III                        ; add to tof and store as next pe update
   1 sto Update_PE_Surface                         ; request a pe surface update
```

(4) OCTO.PRG

```
SEG Define_Data
;--------------Adjustable Variables---------------------------------------------------------------
   ;-------adjustable at beginning of flight--------
   defa      _rf_Amplitude_octo         500
   defa      _octo_entrance_voltage     1
   defa      _octo_axis_voltage         0
   defa      _octo_exit_voltage         -10
   defa      PE_Update_each_usec        0.001             ; pe surface update time step in usec
   defa      Frequency_Hz_octo          2.1E6             ; in Hz

;---------------------adjustable during flight-----------------------------------------------------
   defa      _AMU_Mass_per_Charge       205.0             ; mass tune point in amu/unit charge

;--------------Static Variables--------------------------------------------------------------------
   defs omega_octo                      2.1               ; freq of octopole
   defs Next_PE_Update_IV               0.0               ; next time to update pe surface

;==================================================================
SEG Fast_Adjust
   rcl omega_octo                                         ; save frequency in radians / usec
   RCL Ion_Time_of_Flight
   *
   Sin
   RCL _rf_Amplitude_octo
   *
   sto temp
   rcl _octo_axis_voltage
   +
   STO Adj_Elect02                                        ; rod 2,4,6,8
   rcl _octo_axis_voltage
   rcl temp -
   sto Adj_Elect01                                        ; rod 1,3,5,7
   exit
;------------------------------------------------------------
seg tstep_adjust
   rcl ion_time_step 0.0013
   x>y exit
   sto ion_time_step
exit
;-----------------------------------------------------------
seg Other_Actions
   rcl Next_PE_Update_IV                                  ; recall time for next pe surface update
   rcl Ion_Time_of_Flight                                 ; recall ion's time of flight
   x<y exit                                               ; exit if tof less than next pe update
   rcl PE_Update_each_usec                                ; recall pe update increment
   + sto  Next_PE_Update_IV                               ; add to tof and store as next pe update
   1 sto  Update_PE_Surface                               ; request a pe surface update
```

(5) BENDER2.PRG

```
;------- definition of user adjustable variables  -----------------------
           ; ---------- adjustable during flight QUADRUPOLE -----------------
defa _Percent_tune_2                    70.0              ; percent of optimum tune
defa _AMU_Mass_per_Charge               205.0             ; mass tune point in amu/unit charge
defa _AMU_Mass_per_Charge_2             205.0             ; mass tune point in amu/unit charge
defa _Quad_Entrance_Voltage_2           -5.0              ; voltage of quad entrance
defa _Quad_Axis_Voltage_2               0.0               ; voltage of quad axis
defa _Quad_Exit_Voltage_2               -200.0            ; voltage of quad exit
```

```
            ; ---------- adjustable at beginning of flight -----------------
defa PE_Update_each_usec                0.001           ; pe surface update time step in usec
defa Phase_Angle_Deg                    80.0            ; entry phase angle of ion
defa Frequency_Hz_2                     1.2E6           ; rf frequency of quad in (Hz)
defa Effective_Radius_in_cm_2           0.43            ; effective quad radius r0 in cm
defa theta_quad_2                       0.0             ; phase offset in radians

; ------------definition of static variables -----------------------------
defs premier                            0.0
defs scaled_rf_quad_2                   0.0             ; scaled rf base
defs rfvolts_quad_2                     0.0             ; rf voltage
defs dcvolts_quad_2                     0.0             ; dc voltage
defs omega_2                            1.2             ; freq in radians / usec
defs theta_2                            0.0
defs first                              0.0

defs Next_PE_Update_V                   0.0             ; next time to update pe surface

;===========================OCTOPOLE=======================================
defa _rf_Amplitude_octo                 500
defa _octo_entrance_voltage             1
defa _octo_axis_voltage                 0
defa _octo_exit_voltage                 -10
defa Frequency_Hz_octo                  2.1E6           ; in Hz
defs omega_octo                         2.1             ; freq of octopole

; program segments below --------------------------------------------
;-----------------------------------quad2-----------------------------
seg Fast_Adjust                                         ; generates rf with fast adjust
rcl first
x=0 gsb init

  rcl scaled_rf_quad_2
  rcl _AMU_Mass_per_Charge_2 *                          ; multiply by mass per unit charge
  sto rfvolts_quad_2                                    ; save rf voltage
  rcl scaled_rf_quad_2
  rcl _AMU_Mass_per_Charge_2 *                          ; multiply by mass per unit charge
  rcl _Percent_tune_2 *                                 ; substitute dc tune point
  100 /
  0.1678399 *
  sto dcvolts_quad_2
  rcl _Quad_entrance_Voltage_2
  sto Adj_elect12                                       ; update quad exit voltage
  rcl Ion_Time_of_Flight                                ; current tof in micro seconds
  rcl omega_2 *                                         ; omega * tof
  rcl theta_2 +                                         ; add phasing angle
  sin                                                   ; sin(theta + (omega * tof))
  rcl rfvolts_quad_2 *
  rcl dcvolts_quad_2 +                                  ; times rf voltage
  sto tempvolts_2                                       ; save rf dc voltage
  rcl _Quad_Axis_Voltage_2 +                            ; add quad axis voltage
  sto Adj_Elect09                                       ; electrode 1 voltage
  rcl _Quad_Axis_Voltage_2                              ; recall quad axis voltage
  rcl tempvolts_2 -                                     ; subtract rf dc from it
  sto Adj_Elect10                                       ; electrode 2 voltage

  ;------------------------------octo-----------------------------
  rcl _octo_exit_voltage
  sto Adj_Elect04
  RCL Ion_Time_of_Flight
  rcl omega_octo
  *
  Sin
  RCL _rf_Amplitude_octo *
  sto temp
  rcl _octo_axis_voltage
  +
  STO Adj_Elect02                                       ; rod 2,4,6,8
  rcl _octo_axis_voltage
  rcl temp -
  STO Adj_Elect01                                       ; rod 1,3,5,7
```

```
lbl init                                        ; parameter initialization subroutine
   1 sto first                                  ; turn off first pass flag
   RCL Effective_Radius_in_cm_2                 ; recall effective radius in cm
   entr *                                       ; (r * r)
   rcl Frequency_Hz_2 entr * *                  ; multiply by frequency squared
   7.22175e-12 *                                ; 7.22175e-12 * MASS * FREQ * FREQ * R0 * R0
   sto scaled_rf_quad_2
   rcl _AMU_Mass_per_Charge_2 *                 ; multiply by mass per unit charge
   sto rfvolts_quad_2                           ; save rf voltage
   rcl scaled_rf_quad_2
   rcl _AMU_Mass_per_Charge_2 *                 ; multiply by mass per unit charge
   rcl _Percent_tune_2 *                        ; substitute dc tune point
   100 /
   0.1678399 *
   sto dcvolts_quad_2                           ; save dc voltage
   rcl theta_quad_2
   >rad                                         ; degrees to radians
   sto theta_2                                  ; phase angle
   rcl Frequency_Hz_2                           ; rf frequency in hz
   6.28318E-6 *                                 ; to radians / microsecond
   sto omega_2                                  ; save frequency in radians / usec
   rtn                                          ; return from subroutine
;---------------------------------------------------------
seg tstep_adjust
   rcl ion_time_step 0.0013
   x>y exit
   sto ion_time_step
exit

;-----------------------------------------------------------------------
seg Other_Actions                               ; used to control pe surface updates
   rcl Next_PE_Update_V                         ; recall time for next pe surface update
   rcl ion_time_of_flight                       ; recall ion's time of flight
   x<y exit                                     ; exit if tof less than next pe update
   rcl PE_Update_each_usec                      ; recall pe update increment
   + sto Next_PE_Update_V                       ; add to tof and store as next pe update
   1 sto Update_PE_Surface                      ; request a pe surface update
```

(6) QUAD2.PRG

```
; definition of user adjustable variables  -----------------------
; ---------- adjustable during flight -----------------
defa _Percent_tune_2                 70.0          ; percent of optimum tune
defa _AMU_Mass_per_Charge_2          205.0         ; mass tune point in amu/unit charge
defa _Quad_Entrance_Voltage_2        0.0           ; voltage of quad entrance
defa _Quad_Axis_Voltage_2            0.0           ; voltage of quad axis
defa _Quad_Exit_Voltage_2            -200.0        ; voltage of quad exit

; ---------- adjustable at beginning of flight -----------------
defa PE_Update_each_usec             0.001         ; pe surface update time step in usec
defa Phase_Angle_Deg                 80.0          ; entry phase angle of ion
defa Frequency_Hz_2                  1.2E6         ; rf frequency of quad in (hz)
defa Effective_Radius_in_cm_2        0.43          ; effective quad radius r0 in cm
defa theta_quad_2                    0.0           ; phase offset in radians

; definition of static variables -----------------------------
defs scaled_rf_quad_2                0.0           ; scaled rf base
defs rfvolts_quad_2                  0.0           ; rf voltage
defs dcvolts_quad_2                  0.0           ; dc voltage
defs omega_2                         1.2           ; freq in radians / usec
defs theta_2 0.0
defs Next_PE_Update_VI               0.0           ; next time to update pe surface


; program segments below -------------------------------------------
;-----------------------------------------------------------------------
seg Fast_Adjust                                    ; generates rf with fast adjust
```

```
rcl scaled_rf_quad_2
rcl _AMU_Mass_per_Charge_2 *                        ; multiply by mass per unit charge
sto rfvolts_quad_2                                  ; save rf voltage
rcl scaled_rf_quad_2
rcl _AMU_Mass_per_Charge_2 *                        ; multiply by mass per unit charge
rcl _Percent_tune_2 *                               ; substitute dc tune point
100 /
0.1678399 *
sto dcvolts_quad_2                                  ; save dc voltage
rcl Ion_Time_of_Flight                              ; current tof in micro seconds
rcl omega_2 *                                       ; omega * tof
rcl theta_2 +                                       ; add phasing angle
sin                                                 ; sin(theta + (omega * tof))
rcl rfvolts_quad_2 *                                ; times rf voltage
rcl dcvolts_quad_2 +                                ; add dc voltage
sto tempvolts_2                                     ; save rf dc voltage
rcl _Quad_Axis_Voltage_2 +                          ; add quad axis voltage
sto Adj_Elect01                                     ; electrode 1 voltage
rcl _Quad_Axis_Voltage_2                            ; recall quad axis voltage
rcl tempvolts_2 -                                   ; subtract rf dc from it
sto Adj_Elect02                                     ; electrode 2 voltage
                                                    ; exit program segment

;-----------------------------------------------------------------------
seg Other_Actions                                   ; used to control pe surface updates
rcl Next_PE_Update_VI                               ; recall time for next pe surface update
rcl ion_time_of_flight                              ; recall ion's time of flight
x<y exit                                            ; exit if tof less than next pe update
rcl PE_Update_each_usec                             ; recall pe update increment
+ sto next_pe_update_VI                             ; add to tof and store as next pe update
1 sto Update_PE_Surface                             ; request a pe surface update
```

(7) QUADOUT.PRG

```
; definition of user adjustable variables  ----------------------
                ; ---------- adjustable during flight -----------------
defa _Percent_tune_2                    70.0        ; percent of optimum tune
defa _AMU_Mass_per_Charge_2             205.0       ; mass tune point in amu/unit charge
defa _Quad_Entrance_Voltage_2           0.0         ; voltage of quad entrance
defa _Quad_Axis_Voltage_2               0.0         ; voltage of quad axis
defa _Quad_Exit_Voltage_2               -200.0      ; voltage of quad exit

                ; ---------- adjustable at beginning of flight -----------------
defa PE_Update_each_usec                0.001       ; pe surface update time step in usec
defa Phase_Angle_Deg                    80.0        ; entry phase angle of ion
defa Frequency_Hz_2                     1.2E6       ; rf frequency of quad in (hz)
defa Effective_Radius_in_cm_2           0.43        ; effective quad radius r0 in cm
defa theta_quad_2                       0.0         ; phase offset in radians

; definition of static variables ----------------------------
defs scaled_rf_quad_2                   0.0         ; scaled rf base
defs rfvolts_quad_2                     0.0         ; rf voltage
defs dcvolts_quad_2                     0.0         ; dc voltage
defs omega_2                            1.2         ; freq in radians / usec
defs theta_2  0.0
defs Next_PE_Update_VII                 0.0         ; next time to update pe surface

; program segments below -------------------------------------------
;-----------------------------------------------------------------------
seg Fast_Adjust                                     ; generates rf with fast adjust
   rcl scaled_rf_quad_2
   rcl _AMU_Mass_per_Charge_2 *                     ; multiply by mass per unit charge
   sto rfvolts_quad_2                               ; save rf voltage
   rcl scaled_rf_quad_2
   rcl _AMU_Mass_per_Charge_2 *                     ; multiply by mass per unit charge
   rcl _Percent_tune_2 *                            ; substitute dc tune point
   100 /
   0.1678399 *
   sto dcvolts_quad_2                               ; save dc voltage
```

```
   rcl _Quad_Exit_Voltage_2
   sto Adj_elect04                                  ; update quad exit voltage
   rcl Ion_Time_of_Flight                           ; current tof in micro seconds
   rcl omega_2 *                                    ; omega * tof
   rcl theta_2 +                                    ; add phasing angle
   sin                                              ; sin(theta + (omgga * tof))
   rcl rfvolts_quad_2 *                             ; times rf voltage
   rcl dcvolts_quad_2 +                             ; add dc voltage
   sto tempvolts_2                                  ; save rf dc voltage
   rcl _Quad_Axis_Voltage_2 +                       ; add quad axis voltage
   sto Adj_Elect01                                  ; electrode 1 voltage
   rcl _Quad_Axis_Voltage_2                         ; rcall quad axis voltage
   rcl tempvolts_2 -                                ; subtract rf dc from it
   sto Adj_Elect02                                  ; electrode 2 voltage
   exit                                             ; exit program segment

;------------------------------------------------------------------------
seg Other_Actions                                   ; used to control pe surface updates
   rcl Next_PE_Update_VII                           ; recall time for next pe surface update
   rcl ion_time_of_flight                           ; recall ion's time of flight
   x<y exit                                         ; exit if tof less than next pe update
   rcl PE_Update_each_usec                          ; recall pe update increment
   + sto Next_PE_Update_VII                         ; add to tof and store as next pe update
   1 sto Update_PE_Surface                          ; request a pe surface update
```

BENDER1.GEM

```
pa_define(155,61,231,p,y)
;====================QUADRUPOLE===============================
locate(95,0,60,40)
{
electrode(1)                                                           ; quad positive poles
          { fill{locate(-1.878,0,0,1,90)
                         {within{cylinder(0.3525,0,0,0.1875,,0.5)}
                          within{cylinder(-0.3525,0,0,0.1875,,0.5)}}}}
electrode(2)                                                           ; quad negative poles
          {locate(-1.878,0,0,1,90)
                 {fill {within{cylinder(0,0.3525,0,0.1875,,0.5)}}} }
electrode(3)
          { locate(-1.5,0,0,1,90)
                 {fill{     within{cylinder(0,0,0,0.918,,0.094)}
                            within{cylinder(0,0,0,0.815,,0.25)}
                            notin{cylinder(0,0,0,0.533,,0.25)}
                            notin{cylinder(0,0.625,0,0.035,,0.25)}     ; holes
                            notin{cylinder(0.625,0,0,0.035,,0.25)}     ; idem
                            notin{cylinder(-0.625,0,0,0.035,,0.25)}    ; idem
                            notin{cylinder(0.44,0.44,0,0.035,,0.25)}   ; idem
                            notin{cylinder(-0.44,0.44,0,0.035,,0.25)}}}} ; idem
   electrode(4)
          {locate(-1.5,0,0,1,90)                                       ; exit lens
                 { fill {   within_inside{cylinder(0,0,0,0.4975,,0.185)}
                            notin_inside{cylinder(0,0,0,0.15,,0.185)}}}}}

;===================BENDER=========================================
locate(95,0,60,40,-90,,-90)
{ electrode(5)                                                         ; 1st pair of poles
          { fill{ within{    locate(0,0,0,1,,-45)
                            {hyperbola(0,0,0.723,0.789)}
                            centered_box3D(0,0,0,2.4,2.4,2.4) }}}

electrode(6)                                                           ; 2nd pair of poles
          {fill {within{ locate(0,0,0,1,,45)
                  {hyperbola(0,0,0.723,0.789)}
                 centered_box3d(0,0,0,2.4,2.4,2.4)  }} }}

locate(95,0,60,40)
{ electrode(7)
           {fill { locate(0,0,0,1,-90)                                 ; right focusing lens
                 { within{cylinder(0,0,-1.25,0.5,,0.2)}
                  notin{cylinder(0,0,-1.25,0.25,,0.2)}}}
```

```
            fill { locate(0,0,0,1,90)                                   ; left focusing lens
                      {within{cylinder(0,0,-1.25,0.5,,0.2)}
                       notin{cylinder(0,0,-1.25,0.25,,0.2)}}}}
     electrode(8)
             {fill { locate(0,0,0,1,180)                                ; front focusing lens
                      { within{cylinder(0,0,-1.25,0.5,,0.2)}
                      notin{cylinder(0,0,-1.25,0.25,,0.2)}}}
              fill  {    within{cylinder(0,0,-1.25,0.5,,0.2)}           ; back focusing lens
                      notin{cylinder(0,0,-1.25,0.25,,0.2)}}}}

;=========================lenses============================================
locate(95,0,60,40)
   {electrode(9)
             {locate(0,0,1.602,1,180)
                      { fill {     within{cylinder(0,0,-0.093,0.3,,0.219)}
                                   within{cylinder(0,0,-0.062,0.35,,0.031)}
                                   within{cylinder(0,0,0,0.75,,0.06)}
                                   notin{cylinder(0,0,0,0.25,,0.312)}
                                   notin{cylinder(0.5795,0,0,0.09,,0.312)}       ; holes
                                   notin{cylinder(0,0.5795,0,0.09,,0.312)}       ; idem
                                   notin{cylinder(-0.5795,0,0,0.09,,0.312)} }}}  ; idem
   electrode(10)
             {locate(0,0,1.945,1,180)
                      {fill{       within{cylinder(0,0,0,0.3,,0.219)}
                                   within{cylinder(0,0,-0.219,0.35,,0.031)}
                                   within{cylinder(0,0,-0.25,0.75,,0.062)}
                                   notin{cylinder(0,0,0,0.25,,0.312)}
                                   notin{cylinder(0.5795,0,0,0.09,,0.312)}       ; holes
                                   notin{cylinder(0,0.5795,0,0.09,,0.312)}       ; holes
                                   notin{cylinder(-0.5795,0,0,0.09,,0.312)}}}}   ; holes
   electrode(11)
             {locate(0,0,2.288,1,180)
                      {fill{       within{cylinder(0,0,-0.093,0.3,,0.219)}
                                   within{cylinder(0,0,-0.062,0.35,,0.031)}
                                   within{cylinder(0,0,0,0.75,,0.062)}
                                   notin{cylinder(0,0,0,0.25,,0.312)}
                                   notin{cylinder(0.5795,0,0,0.09,,0.312)}       ; holes
                                   notin{cylinder(0,0.5795,0,0.09,,0.312)}       ; holes
                                   notin{cylinder(-0.5795,0,0,0.09,,0.312)}}}}   ; holes
   electrode(12)
             {locate(0,0,2.631,1,180)
                      {fill{       within{cylinder(0,0,0,0.3,,0.219)}
                                   within{cylinder(0,0,-0.219,0.35,,0.031)}
                                   within{cylinder(0,0,-0.25,0.75,,0.062)}
                                   notin{cylinder(0,0,0,0.25,,0.312)}
                                   notin{cylinder(0.5795,0,0,0.09,,0.312)}       ; holes
                                   notin{cylinder(0,0.5795,0,0.09,,0.312)}       ; holes
                                   notin{cylinder(-0.5795,0,0,0.09,,0.312) }}}}  ; holes

   electrode(13)
             {locate(0,0,3,1,180)
                      {fill{       within{cylinder(0,0,-0.093,0.3,,0.219)}
                                   within{cylinder(0,0,-0.062,0.35,,0.031)}
                                   within{cylinder(0,0,0,0.75,,0.062)}
                                   notin{cylinder(0,0,0,0.25,,0.312)}
                                   notin{cylinder(0.5795,0,0,0.09,,0.312)}       ; holes
                                   notin{cylinder(0,0.5795,0,0.09,,0.312)}       ; holes
                                   notin{cylinder(-0.5795,0,0,0.09,,0.312)} }}}} ; holes

;=====================octopole==============================
locate(95,0,60,40)
    {electrode(14)                                                       ; poles
             {locate(0,0,3.742,1,180)
                      {fill{        within_inside{cylinder(0,0.25,0,0.0625,,0.5)}
                                    within_inside{cylinder(0.25,0,0,0.0625,,0.5)}
                                    within_inside{cylinder(-0.25,0,0,0.0625,,0.5)}}} }
   electrode(15)
              {locate(0,0,3.742,1,180)                                   ; poles

                      {fill {       within_inside{cylinder(0.177,0.177,0,0.0625,,0.5)}
                                    within_inside{cylinder(-0.177,0.177,0,0.0625,,0.5)}}}}
             electrode(16)
```

```
                  {locate(0,0,3.372,1,180)
                   {fill{ within{cylinder(0,0,0,0.918,,0.094)}        ; grounded plate of entrance lens
                          within{cylinder(0,0,0,0.815,,0.25)}
                           notin{cylinder(0,0,0,0.533,,0.25)}
                           notin{cylinder(0.44,0.44,0,0.032,,0.25)}   ; holes
                           notin{cylinder(-0.44,0.44,0,0.032,,0.25)}
                           notin{cylinder(0.44,0.44,-0.125,0.13,,0.125)}
                           notin{cylinder(-0.44,0.44,-0.125,0.13,,0.125)} }}}
          electrode(17)
                           { locate(0,0,3.372,1,180)                  ; entrance lens
                                   {fill{  within_inside{cylinder(0,0,0,0.4975,,0.185)}
                                           notin_inside{cylinder(0,0,0,0.15,,0.185)} } }}}
```

BENDER2.GEM

```
 pa_define(155,61,171,p,y)

;======================octopole==============================
locate(60,0,0,40)
   { locate(0,0,0.5,1) {
          electrode(1)                                                ; poles
                  {fill  {within_inside{cylinder(0,0.25,0,0.0625,,0.6)}
                          within_inside{cylinder(0.25,0,0,0.0625,,0.6)}
                          within_inside{cylinder(-0.25,0,0,0.0625,,0.6)}}}
          electrode(2)                                                ; poles
                  { fill {within_inside{cylinder(0.177,0.177,0,0.0625,,0.6)}
                           within_inside{cylinder(-0.177,0.177,0,0.0625,,0.6)}}}}
          locate(0,0,0.878,1)
          {electrode(3)                                               ; plate of exit lens
                  {fill{  within{cylinder(0,0,0,0.918,,0.094)}
                          within{cylinder(0,0,0,0.815,,0.25)}
                          notin{cylinder(0,0,0,0.533,,0.25)}
                          notin{cylinder(0,0.625,0,0.035,,0.25)}      ; holes
                                  notin{cylinder(0.625,0,0,0.035,,0.25)}
                          notin{cylinder(-0.625,0,0,0.035,,0.25)}
                          notin{cylinder(0.44,0.44,0,0.035,,0.25)}
                          notin{cylinder(-0.44,0.44,0,0.035,,0.25)}}}
          electrode(4)
                  {fill{ within_inside{cylinder(0,0,0,0.4975,,0.185)}  ; exit lens
                  notin_inside{cylinder(0,0,0,0.15,,0.185)}}}}}

;====================BENDER===========================================
locate(60,0,95,40,-90,,-90)
{
electrode(5)                                                          ; 1st pair of poles
          {fill{  within{ locate(0,0,0,1,,-45)
                  {hyperbola(0,0,0.723,0.789)}
                  centered_box3D(0,0,0,2.4,2.4,2.4)}}}
electrode(6)                                                          ; 2nd pair of poles

          { fill {within{locate(0,0,0,1,,45)
                  {hyperbola(0,0,0.723,0.789)}
                  centered_box3d(0,0,0,2.4,2.4,2.4)}}}}
locate(60,0,95,40)
{ electrode(7)
          {fill{locate(0,0,0,1,-90)                                   ; right focusing lens
                  { within{cylinder(0,0,-1.25,0.5,,0.2)}
                   notin{cylinder(0,0,-1.25,0.25,,0.2)}}}
          fill {locate(0,0,0,1,90)                                    ; left focusing lens
                   { within{cylinder(0,0,-1.25,0.5,,0.2)}
                    notin{cylinder(0,0,-1.25,0.25,,0.2)}}}}
 electrode(8)
          {fill {locate(0,0,0,1,180)                                  ; front focusing lens
                  {within{cylinder(0,0,-1.25,0.5,,0.2)}
                  notin{cylinder(0,0,-1.25,0.25,,0.2)}}}
           fill{                                                      ; back focusing lens
                   within{cylinder(0,0,-1.25,0.5,,0.2)}
                   notin{cylinder(0,0,-1.25,0.25,,0.2)}}}}

;====================QUADRUPOLE================================
locate(60,0,95,40)
{electrode(9)                                                         ; quad positive poles
```

```
            {fill{locate(+1.878,0,0,1,-90)
                        {within{cylinder(0.3525,0,0,0.1875,,0.5)}
                        within{cylinder(-0.3525,0,0,0.1875,,0.5)}}}}
electrode(10)                                                                    ; quad negative poles
   {locate(+1.878,0,0,1,-90)
            {fill{       within{cylinder(0,0.3525,0,0.1875,,0.5)}}}}
electrode(11)
   {locate(+1.5,0,0,1,-90)
            {fill{       within{cylinder(0,0,0,0.918,,0.094)}
                         within{cylinder(0,0,0,0.815,,0.25)}
                         notin{cylinder(0,0,0,0.533,,0.25)}
                         notin{cylinder(0.44,0.44,0,0.032,,0.25)}                ; holes
                         notin{cylinder(-0.44,0.44,0,0.032,,0.25)}               ; idem
                         notin{cylinder(0.44,0.44,-0.125,0.13,,0.125)}           ; idem
                         notin{cylinder(-0.44,0.44,-0.125,0.13,,0.125)} }} }     ; idem

electrode(12)
   {locate(+1.5,0,0,1,-90)                                                       ; entrance lens
            {fill {      within_inside{cylinder(0,0,0,0.4975,,0.185)}
                         notin_inside{cylinder(0,0,0,0.15,,0.185)}}}}}
```

QUADOUT.GEM

```
pa_define(71,61,151,p,y)

;====================QUADRUPOLE===============================
locate(35,0,60,40)
{electrode(1)                                                                    ; quad positive poles
            { fill{locate(0.378,0,0,1,-90)
                        {within{cylinder(0.3525,0,0,0.1875,,0.5)}
                        within{cylinder(-0.3525,0,0,0.1875,,0.5)}}}}
electrode(2)                                                                     ; quad negative poles
             {locate(0.378,0,0,1,-90)
                          { fill{within{cylinder(0,0.3525,0,0.1875,,0.5)}}}}
electrode(3)
   {locate(0,0,0,1,-90)
            {fill        {within{cylinder(0,0,0,0.918,,0.094)}
                          within{cylinder(0,0,0,0.815,,0.25)}
                          notin{cylinder(0,0,0,0.533,,0.25)}
                          notin{cylinder(0,0.625,0,0.035,,0.25)}                 ; holes
                          notin{cylinder(0.625,0,0,0.035,,0.25)}                 ; idem
                          notin{cylinder(-0.625,0,0,0.035,,0.25)}                ; idem
                          notin{cylinder(0.44,0.44,0,0.035,,0.25)}               ; idem
                          notin{cylinder(-0.44,0.44,0,0.035,,0.25) }}}}          ; idem
electrode(4)
   {locate(0,0,0,1,-90)                                                          ; quad entrance lens
            {fill {        within_inside{cylinder(0,0,0,0.4975,,0.185)}          ; electrode (int)
                           notin_inside{cylinder(0,0,0,0.15,,0.185)}}}}}
```

Acknowledgments

I would like to thank Prof. Rizzo, who accepted me in his group and showed to me that science can be driven by dreams no matter how old they are and how 'crazy' they are.

Also, I would like to express my sincere gratitude to all the people who contributed to this work, either for their scientific input or for their friendship and in particular to:

Dr. Oleg Boyarkin, for sharing his knowledge in laser spectroscopy and for his rigorous, reliable and efficient work,

Dr. Rainer Beck for his advice and experience in building scientific instruments,

Prof. Evan Williams and Dr. Matt Bush for their fruitful collaboration in the theoretical part of this work,

Prof. Tino Gaümann for sharing so generously his findings in the literature, keeping me always up to date with the latest advances in mass spectrometry,

The members of the mechanical and electrical workshops for their great work and promptness,

Prof. Weinkauf, Prof. Leutwyler, Prof. Dyson and Prof. Girault for agreeing to evaluate this thesis work,

Sébastien Mercier for his high-quality work, his patience in the difficult moments shared in building the machine and setting up the experiment, and especially for his particular sense of humor: merci pour "les petits yaourts RAB" en période de crise !

Amanz Ruf for his imaginative solutions to all kinds of technical problems, but also for his interesting ideas, fruitful discussions and his encouragement,

Dr. Plinio Maroni for bringing life and sunshine in the moments of 'isolation' during experiments, Dr. Richard Bossart for his kindness and aid, especially with RRKM calculations, and both for their willingness to help but also for the fun outside the lab.

Monia Guidi, Dr. Jaime Stearns and Caroline Seaiby, the most recent members of the 'bio sub-group' for the lively and pleasant atmosphere brought in the office and their support in the very last stressful moments. Antoine Milon, Cédric Bovet, Rachele Chianese, past colleagues with whom I had the pleasure to work.

Dr. Julia Rebstein, my first officemate for her friendship and for her concern until the end.

All the current and former members of LCPM: Dr. Régis Bisson, Dr. Andreas Braun, Dr. Andrea Callegari, Thanh Tung Dang, Dr. Marcel Drabbels, Dr. Aziz Kasimov, Dr. Monika Kowalczyk, Evgeniy Loginov, Dr. Joachim Makowe, Pavel Maksyutenko, Dr. Dimitrios Papageorgopoulos, Dr. Mikhail Polianski, Dr. David Rueda, Marco Sacchi, Dr. Mathieu Schmid, Dr. Patrice Theulé, for such an enjoyable 'multicultural' environment. A special thanks to those who became real friends along these years.

Marianne Dang, our secretary, for being such a wonderful person,

All my friends in Lausanne, for the special moments shared outside the lab and those abroad for keeping in touch and being 'close' despite distance. It will be too long to list all of them and unfair to name only a few, but I sincerely thank them for their love and support.

My family for being the invisible and unbreakable 'net' always present for me.

CURRICULUM VITAE

Personal

Date and place of birth: 25.01.1978, Geneva
Nationality: Greek
Marital status: Single

Education

2000-2005 : École Polytechnique Fédérale de Lausanne
Ph.D in Physical Chemistry,
Infrared photofragment spectroscopy of charged amino acid water clusters in the gas phase, with Pr. T. R. Rizzo

1999-2000 : Université Louis Pasteur de Strasbourg,
D.E.A (Master of Science) in Physical Chemistry (Mention Très Bien)

1995-1999 : Université Louis Pasteur de Strasbourg,
Studies leading to the diploma in Physical Chemistry

Secondary education in Lycée français d'Athènes, Greece.

Fellow of the French Government ("Bourse d'Excellence du Gouvernement Français") for pursuing studies in a French University (1995-1997).

Fellowship for the D.E.A. (Master of Science) academic year.

Fellowship (June-August 1999) for research experience of undergraduates (REU program) in the University of Florida.

Work/Research experience

September 1999- June 2000 : CNRS Strasbourg, Laboratoire de Spectrométrie de Masse Bio-Organique, France, *Protein desalting using ion exchange resins for purification prior to electrospray mass spectrometry analysis*, with Pr. A. Van Dorsselaer.

June - August 1999 : Department of Chemistry and Center for Chemical Physics, University of Florida, Gainesville, U.S.A *Electronic excited states of* CoO^+, with Dr. P.J. Brucat

June- September 1998 : National Center for Scientific Research 'Demokritos', Institute of Physical Chemistry, Athens, Greece, *Trace elements analysis in airborne particulated matter by Instrumental Neutron Activation Analysis,* with Dr. G.D. Kanias

Publications

Infrared spectroscopy of hydrated amino acids in the gas phase: protonated and lithiated valine, A. Kamariotis, O. V. Boyarkin, S. R. Mercier, M. F. Bush, E. R. Williams, R. D. Beck and T. R. Rizzo, J. Amer. Chem. Soc., in press.

Electronic spectroscopy of cold, protonated tryptophan and tyrosine, O. V. Boyarkin, S. R. Mercier, A. Kamariotis, and T. R. Rizzo, J. Amer. Chem. Soc., submitted.

Languages

Bilingual Greek-French, English, German, Italian (elementary).